MILLIMETER-WAVE CHANNEL CHARACTERIZATION FOR 5G CELLULAR SYSTEMS IN THE UAE AT THE 28 GHZ BAND

by

Mohammed K.Y. Aborahama

A Thesis presented to the Faculty of the
American University of Sharjah
College of Engineering
In Partial Fulfillment
of the Requirements
for the Degree of

Master of Science in
Electrical Engineering

Sharjah, United Arab Emirates
May 2019

Approval Signatures

We, the undersigned, approve the Master's Thesis of Mohammed K.Y. Aborahama.

Thesis Title: Millimeter Wave Channel Characterization for 5G Cellular Systems in the UAE at the 28 GHz Band.

Signature **Date of Signature** (dd /mm/yyyy)

_____ _____
Dr. Amer S. Zakaria
Assistant Professor, Department of Electrical Engineering
Thesis Advisor

_____ _____
Dr. Mahmoud H. Ismail Ibrahim
Associate Professor, Department of Electrical Engineering
Thesis Co-Advisor

_____ _____
Dr. Mohamed El-Tarhuni
Professor, Department of Electrical Engineering
Thesis Co-Advisor

_____ _____
Dr. Mohamed Hassan
Professor, Department of Electrical Engineering
Thesis Committee Member

_____ _____
Dr. Taha Landolsi
Professor, Department of Computer Science and Engineering
Thesis Committee Member

_____ _____
Dr. Nasser Qaddoumi
Head, Department of Electrical Engineering

_____ _____
Dr. Lotfi Romdhane
Associate Dean for Graduate Affairs and Research
College of Engineering

_____ _____
Dr. Naif Darwwish
Acting Dean, College of Engineering

_____ _____
Dr. Mohamed El-Tarhuni
Vice Provost for Graduate Studies

Acknowledgement

First, I would like to thank my advisors Dr. Amer S. Zakaria, Dr. Mahmoud H. Ismail Ibrahim and Dr. Mohamed El-Tarhuni for providing their time throughout my master's stage. I am grateful for their assistance.

I would like to thank Mr. Ibrahim Abu Seif for his continued help and support in my research experiments. I would also thank Professor Lim Nguyen for sharing his experiences and providing his supports.

I would also like to acknowledge the financial support from the American University of Sharjah in the form of graduate teaching and research assistantship.

Finally, I would like to thank engineer Yamen Hatahet, Marwan El Bardicy and Walaa Mosah for helping me in conducting the experimental work.

Abstract

The rapid increase in wireless communication services and the need for higher data rate communications have pushed people towards adopting fifth generation (5G) cellular systems. One of the new technologies to be used in 5G is using the millimeter wave (mm-wave) band for the carrier signals. Though mm-waves are expected to cover the needed bandwidth and data rate, they suffer from higher losses and scattering from more objects within the radio channel than the currently used frequencies. For this reason, the effect of the channel should be studied well before implementing 5G technology to be able to design 5G systems and know their capabilities. This is done by conducting large-scale, small-scale, penetration loss and reflectivity channel measurements. Many measurements have been conducted for mm-wave channel characteristics in different parts of the world. However, no measurements have been reported in environments similar to that in the UAE. Thus, in this work, large-scale, small-scale and penetration loss measurements were conducted in the UAE; the study covers many aspects of wireless channel characteristics. The measurements were conducted from April 2018 until April 2019 in the American University of Sharjah's campus. A narrow-band wireless communication setup and a wideband wireless setup have been assembled. Path loss measurements were conducted in labs, corridors, building rotunda, halls and outdoor areas using 28 GHz band. The measurements revealed that the path loss exponent is mostly around that would be observed in a free space model and that is aligned with measurements reported in the literature. In addition to that, penetration and reflection measurements were conducted for building material used in the UAE. Finally, wideband channel impulse response measurements were conducted in the 24 GHz band with a signal bandwidth of 250 MHz. The power delay profile and channel delay spread results show that the maximum RMS delay spread observed was about 247 ns and 433 ns for indoor and outdoor environments, respectively.

Keywords: ***5G, millimeter-wave, channel characterizations, path loss, power delay profile, measurements campaign***

Table of Contents

List of Figures

List of Tables

List of Abbreviations

3GPP	3rd Generation Partnership Project
4G	4th Generation of Cellular Networks
5G	5th Generation of Cellular Networks
5GCM	5th Generation Channel Model
AM	Amplitude Modulation
AOA	Angle of Arrival
AOD	Angle of Departure
AUS	American University of Sharjah
BS	Base Station
CDF	Cumulative Density Function
CIR	Channel Impulse Response
FM	Frequency Modulation
GPS	Global Positioning System
HBS	Human Body Shadowing
LOS	Line of Sight
LNA	Low Noise Amplifier
MIMO	Multiple Input Multiple Output
MS	Mobile station
Mm-Wave	Millimetre Wave
NLOS	Non-Line of Sight
O2I	Outdoor to Indoor
P2P	Peer to Peer
PDF	Probability Density Function
PDP	Power Delay Profile
PLE	Path loss Exponent
PN	Persuade Noise
RF	Radio Frequency
RMS	Root Mean Square
RX	Receiver
SNR	Signal to Noise Ratio

TX	Transmitter
UAE	United Arab Emirates
UHF	Ultra High Frequency
Wi-Fi	Wireless Fidelity
WINNER	Wireless World Initiative New Radio
XDP	Cross-Polar Discrimination

Chapter 1. Introduction

In this chapter, a short introduction about millimeter wave (mm-wave) channel characteristics is provided. Then, the problems investigated in this study, as well as the thesis contribution, are presented. Finally, the organization of the thesis is highlighted.

1.1. Overview

According to [1], one of the most crucial challenges faced in the attempt to utilize the mm-wave spectrum is the lack of suitable channel models. A great deal of research was done by 3GPP in this field [2-5]. It is noticed that more research was done on the characterization of the 60 GHz band [6, 7] in contrast to the other proposed bands of 28, 38, and 73 GHz [8-11]. This is likely due to greater interest in the 60 GHz band in earlier periods of the development of the radio standards. Some of the mm-wave channel models that have been proposed are summarized in [12].

Mm-waves suffer from high path loss due to the high frequency of operation and the presence of additional attenuation through oxygen absorption [13]. The goal is to deliver always signals with reasonable Signal-to-Noise-Ratio (SNR) over long separation distances between the transmitter and the receiver, an issue that can be resolved by using directional antennas. When compared to frequencies used in 3G and 4G systems, mm-waves undergo greater gaseous and rain attenuation, and are subject to larger attenuation when crossing a given distance [14]. They also fall victim to greater shadowing effects [8]. This can be attributed to the shorter wavelengths, which are associated with shorter skin depth effect. Greater penetration losses are present in higher frequency waves since a waveform has more cycle inside an object as it passes through [15]. Based on the above, to design mm-wave communication systems properly, it is necessary to consider both the wideband and narrowband behaviors of the signals at frequencies of interest.

The need for using mm-wave frequencies in cellular radio systems instead of today's ultra-high frequencies (UHF) is a direct consequence of the rapid growth in the smart-phone industry, technology dependency, and the need for higher data rates. To fulfill these demands, data rates and capacities of wireless channels must increase, which entails the utilization of other frequencies bands in the spectrum.

Almost all commercial wireless communications including AM/FM radio, TV broadcasting, satellite communication, GPS, and Wi-Fi are using a narrow portion of the RF spectrum from 300 MHz to 3 GHz. The current spectrum is flooded by other

applications, showing the value of moving to the untouched spectrum. The RF spectrum above 3 GHz has little research for wireless applications. Some limited experiments have been conducted to explore this spectrum for short-range and fixed wireless communications [16].

The range 57 – 64 GHz, which suffers from about 15 dB/km attenuation from oxygen absorption, was promoted for short range usage [13]. Moreover, frequencies of the 164 – 200 GHz band suffer from great water vapor absorption attenuation [8]. The mentioned band has a limited transmission range and is not preferred for cellular communication. On October 16, 2003, the FCC allocated the 71 – 76 GHz, 81 – 86 GHz, and 92 – 95 GHz frequency bands to be used for ultra-high-speed data communication applications, including point-to-point wireless local area networks, mobile backhaul, and broadband Internet access [17].

Researchers have proposed several frequencies to be used for 5G cellular networks, namely 28, 38 and 73 GHz. Within the range of mm-wave frequencies around 20 – 100 GHz, the proposed frequencies suffer from much less atmospheric absorption attenuation than their respective neighboring frequencies [8].

Moreover, using mm-wave frequencies provides users with higher bandwidth, resulting in higher data rates required to fulfill people's increasing demands in the near future. In [18], the authors expect the data rate of video streaming to reach 3.5 gigabits per second (Gbps) for a carrier frequency of 60 GHz. This data rate can be further improved by using carrier aggregation and other techniques.

As 5G systems are developed and implemented, forming comparisons with 4G systems is a good starting point. It is believed that the main differences between the two systems lie in the allocation of much greater spectrum at untapped mm-wave frequency bands. Furthermore, 5G systems will utilize highly directional beam-forming antennas at both the mobile device and base station (BS), allowing for longer battery life for handhelds and lower outage probabilities.

Additionally, 5G systems will allow for much higher bit rates in larger portions of the coverage area, lower infrastructure costs, and higher capacity for many simultaneous users in both licensed and unlicensed spectrum (e.g., the convergence of Wi-Fi and cellular). 5G will move from using copper and fiber to mm-wave wireless channels, assisting rapid deployment and allowing for mesh-like connectivity to develop between base stations [8, 14].

1.2. Thesis Objectives

In order to successfully design and deploy 5G systems, mm-wave channel characterizations are needed. To the best of the researcher's knowledge, no mm-wave wireless channel measurement had been reported in the UAE environment (Gulf environment). Thus, this work will be the first attempt to use mm-wave channel characteristics in the UAE. The UAE environment is different than most of other countries environment because of its unique weather, building construction style, building interiors, used building material, type of plants, people populations, and many other factors. This work focuses on the channel characteristics measurement at 28 GHz for large-scale measurement and 24 GHz for small-scale measurement. The experimental results provided in this study would allow the wireless communication system designer to predict the coverage of an mm-wave base station and to estimate the maximum achievable data rate without the need for channel equalization.

1.3. Research Contribution

The contributions of this research can be summarized as follows:

- Developed and implemented a path loss measurement system for indoor and outdoor scenarios at 28 GHz frequency in the American University of Sharjah (AUS) campus.
- Conduced penetration and reflection loss measurements at 28 GHz frequency for materials commonly used in UAE's buildings.
- Developed and implemented a wideband measurement system at 24 GHz frequency in different indoor and outdoor scenarios.
- Presented path loss exponent, reflection cofecient, power delay profile results.

1.4. Thesis Organization

The rest of the thesis is organized as follows: Chapter 2 provides a summary of the literature available on mm-wave channel characteristics. Chapter 3 discusses the path loss measurement set up, results and analysis. Chapter 4 presents the penetration and reflection measurement set up, results and analysis. Chapter 5 shows the small-scale measurements done in this work. Finally, Chapter 6 concludes the thesis and outlines recommended future work.

Chapter 2. Background and Literature Review

This chapter reviews the available literature on mm-wave channel characteristics. Channel characterization is divided into large-scale and small-scale. Large-scale characterization measures whether the receiver will receive detectable power or not. Large-scale measurement is usually conducted using a single tone frequency; thus, it called a narrow band measurement. In large-scale characterization, people usually conduct path loss measurements, coverage and outage measurements, penetration loss measurements and reflection loss measurements. Small-scale characterization is concerned with the channel impulse response (CIR). In this measurement, a wideband signal is used; thus, it is called wideband measurement. Small-scale characterization provides the channel's power delay profile (PDP), delay spread, and angle of arrival (AOA) and angle of departure (AOD) measurements. Predicting the CIR is important to design proper modulation and equalization techniques to mitigate the effects of multipath propagation.

2.1. Large-scale Channel Characteristics

To implement mm-wave technology, it is important to ensure that the receiver (RX) will pick up a signal with high enough SNR and with as little distortion or interference as possible. This can be done by conducting path loss measurements, which is the first step towards testing the performance of mm-wave systems. Path loss measurement is done by finding the attenuation of the transmitted signal until it reaches the receiver antenna. The path loss exponent (PLE) is an important parameter to estimate from path loss measurement results. The PLE is a quantity used to measure how lossy the environment is for a wireless signal. Path loss measurement campaigns have been reported in the literature for both indoor [10, 11, 19, 20] and outdoor scenarios [8, 21-24] since it is required to form a full picture of the performance of systems utilizing the newly proposed frequencies. In general, the received signal might be composed of a line of sight (LOS) component, reflected components, penetrated components and diffracted components [25]. The LOS case means that there is a direct path between the TX and RX, which is not the case for non-line of sight (NLOS). Implementing path loss measurements is relatively simple since it is only required to generate a single tone signal at the desired carrier frequency, transmit it through an antenna, receive it through an antenna, mix it down and measure the power loss in the signal. This section will talk about large-scale measurements results reported by

previous researchers, probabilistic models, path loss models developed and finally the coverage area of mm-wave.

2.1.1. Review of large-scale measurement results. Early works showed that the PLE for mm-wave in indoor environments under the LOS propagation case is lower than that of free-space (FS) [10, 11]. The reason lies in the reflective conducting materials that make up the inside of buildings, acting as waveguides until signals reach the RX. On the other hand, PLE for the NLOS case in indoor environments is higher than the FS case [26] due to the signal requiring multiple reflections before arriving at the RX antenna.

Generally, for outdoor transmission, LOS propagation has a PLE close in value to that of the FS scenario, while the NLOS case has larger PLE similar to that of urban environments [8]. Additional losses at the frequencies of interest in the LOS case are attributed to atmospheric absorption [13], and presence of dust and humidity [8]. At shorter wavelengths, particles appear to be large and contribute to losses, which are not present at longer wavelengths. Additional losses appear under NLOS transmission due to the higher reflection and penetration losses from objects in the environment [8]. To sum it all up, the PLE, in the case of NLOS indoor propagation, is generally higher than that of the NLOS outdoor scenario [10].

The more the environment can be categorized as “urban”, the higher the PLE [8, 27]. Foliage is present in many cities and is an unanticipated source of much attenuation due to the high penetration losses.[28]. To address this specific issue, a possible solution is to reduce the cell radius by increasing the number of base stations, raising the transmitted power, or introducing several reflectors to guide the signals around the trees. The presence of ground reflection losses further degrades the efficiency of the system [28].

2.1.1.1. *Effect of rain*. The presence of rain and its intensity should be taken into consideration when developing a channel model for mm-wave transmission; rain droplets act as scattering objects, meaning that the PLE is generally higher in a rainy environment when compared to that of a dry environment. Another side effect of the scattering is the larger number of resulting multipath components [29]. This justifies the general observation of larger penetration losses when signals propagate through the surfaces and objects [29].

2.1.1.2. Use of beamforming techniques. All of the previous factors increase the PLE, which results in degrading the performance of wireless systems. We can generally decrease the PLE for NLOS scenarios by using the link that forms at the "best pointing angle", where this angle is obtained by sweeping both TX and RX and setting them at a point to acquire the largest received SNR. Using beamforming for both TX and RX antennas allows mm-wave systems to have a performance like today's UHF systems in terms of received power [11, 30, 31].

2.1.1.3. Comparison between large-scale measurements for mm-wave and other frequencies. Measurements in [11] show that the PLE at 73 GHz is larger than 28 GHz, affirming the idea that higher frequencies will inevitably result in higher losses. On the other hand, a study presenting a comparison between 29 GHz and 2.9 GHz shows that there is no big difference in losses for the provided distance, but the larger difference exists in terms of excess delay when comparing LOS and NLOS propagation [30]. Even though the study from [19] shows that penetration losses at 73 GHz are not much different than those of current Wi-Fi systems, it is still evident that there will be a greater PLE at higher frequencies of operation [10, 27]. Differences in the PLEs of 73 GHz and UHF are negligible under LOS conditions, making the two systems very similar [27].

In [32], a comparison between 2.9, 29 and 61 GHz frequencies was performed under several scenarios. Starting with an indoor office scenario, it was observed that the PLE of the mm-wave frequencies were lower than those of the 2.9 GHz in the LOS scenario. Furthermore, in the urban micro street scenario and indoor shopping malls, differences were negligible (in the order of hundredths). When moving to the outdoor open areas, the PLE showed a bigger increase as frequencies increased; in mm-waves, scattering has great importance to the system and serves as an effective way to reduce the PLE. This is why the PLE of mm-waves in tighter and narrower environments is closer to, and may sometimes be lower than, that of 2.9 GHz. Under NLOS, the differences are clear, and the trend continues where greater PLE is attributed to higher frequencies due to the higher reflection losses present in mm-waves.

2.1.1.4. Effect of cross-polarization. Another property that appears when using mm-wave frequencies is that losses resulting from having the antennas in cross-polarized orientations are considerably high according to measurements conducted in [8]. Cross-polarization occurs when the electric field resulting from the transmitter

antenna is not aligned, or is perpendicular with the electric field of the receiver antenna if it were to transmit an electromagnetic signal. Co-polarization, on the other hand, occurs when the electric fields are aligned, and is the typical desired case for any transmission. Measurements in [28] showed that cross-polar discrimination (XPD), an indication of the amount of power lost due to improper polarization, is very high in environments populated by foliage. This leads to the possibility of employing orthogonal frequency reuse, a technique that utilizes different antenna polarizations for increasing channel capacity without an increase in interference.

2.1.1.5. Effect of human mobility and human body shadowing. Another parameter that can affect path loss for mm-wave frequencies is the mobility of elements in the environment such as cars and people. To elaborate further on the impact of mobility, a study was performed indoors showing the throughput in the presence of people under mm-wave transmission. Measurements showed that the throughput indoors can vary from 500 megabits per second (Mbps) to almost no throughput purely due to the movement of people. The rapid variation in path loss due to the change in the environment from the transmitter to the receiver is dictated by the order of which the environment changes, resulting in a direct change in throughput [32].

Extensive studies have been performed on human body shadowing (HBS) effects, as they constitute another factor affecting mm-wave channels [32-37]. Measurements show that losses due to HBS are high, for human bodies obstruct and reflect signals substantially [33]. Studies show that the closer the human body is to the RX, the more losses it causes [34]. For 28 GHz carrier frequencies, it was found that HBS has a range of (15.62 to -6.29 dB) [35]. In fact, the amplitude of the shadowing depends on the antenna configuration, not on the number of people [33]. Directive antennas were not seen to cause angular diversity; thus shadowing effects mean amplitude found to be greater than 15 dB in 90% of the cases. If the antenna has a wide beam width, the shadowing effect has a shorter duration, lower amplitude and slower rising time. This is caused by the channel diversity which leads to the fact that that the channel is unavailable during about 1–2% of the time when one to five persons move between the antennas or in their vicinity [33]. As we increase the frequency of the signal, shadowing effects also become more dominant [36]. Unexpectedly, however, the presence of moving objects in the environment, people for example, improves signal coverage in NLOS scenarios [37]. It still holds true that obstructions in LOS cases will result in

lower coverage [37]. Some statistical models were developed in [36] as a way of approximating the effects that the presence of people has on the signal, specifically in terms of the induced shadowing. The fading characteristics in some environments, where people are the main source of obstruction, were found to have a statistical distribution similar to that of a Nakagami-Rice distribution [38]. Due to the size and movement speed of the typical human body, mixed with the short wavelengths of high-frequency signals, the duration of the shadowing caused by people is usually in the order of hundreds of milliseconds. Clearly, the duration of the shadowing that the signals undergo will increase with the greater number of people. This period is much larger than the signal duration of mm-wave signals, leading to a significant decrease in throughput. These shadowing effects can be combated by making the receiver dependent on the NLOS components through having a receiver capable of collecting signals from 360° in the azimuth plane [33].

2.1.1.6. Solutions for high path loss and environment effects. To compensate for all the aforementioned losses in mm-wave systems effectively, high gain antennas are necessary in spatial array configurations, jointly with the implementation of some beamforming techniques [32]. Moreover, because of the very short wavelengths in such high frequencies, directive antennas are much smaller in size and cost less to manufacture, compared to antennas used in lower frequencies [39].

2.1.2. Probabilistic path loss models. It is much more convenient and time effective for designers to use mathematical models extracted from measurements for describing the behavior of the wireless signals and channels. Plenty of models were created in an attempt to predict the path loss of a signal under different scenarios. Some of these models indicate the probability of the PLE to reach a specific threshold. Other models were proposed to predict the path loss of a signal under specific conditions. A summary of those models can be found in [12]. To the best of the researcher's knowledge, 5GCM models provide more dependable numerical results, since they cover most measurement scenarios under which 5G systems will operate [12].

2.1.3. Coverage and outage measurements. Coverage area is the area where signal power is high enough to be detected. Otherwise, outage is occurring. Determining the coverage area is a vital step in designing wireless systems, as it is used to plan the number of base stations, their placements, and their power specifications. Researchers want to decrease cell coverage areas as much as possible so that the number of cells can

be increased, and thus increasing the network capacity [40]**.** Moreover, the inter-cellular interference is minimized for mm-wave due to the higher path loss affecting it [39]. Furthermore, with the presence of many base stations nearby, different types of cooperative multiple-input and multiple-output (MIMO) architectures can be implemented to further improve performance gains. A side effect of increasing the number of required base stations for a given 5G network is reflected onto the economical side of things; the greater the number of manufactured base stations is, the less their independent costs will be. This makes it easier to expand the network at a lower cost in the long run [41]. Coverage is a factor greatly reliant on base station and mobile station (MS) parameters. Antenna gains, transmitted power, radio-frequency (RF) bandwidth, carrier frequency, and modulation and coding techniques are examples of such parameters [39]. Many research outcomes concluded that mm-wave 5G cellular networks coverage areas should have radii of about 200 meters [8, 27, 39]. While cells with 200 meter radii are good for most cases, coverage in semi-urban environments is better than that in urban environments [27].

One of the early coverage area tests conducted for carrier frequencies of 28 and 38 GHz were performed in [8]. Outage studies were also conducted in Austin at 38 GHz, concluding that lower base station heights provide better close-in coverage. No outages occurred within a 200 m cell radius for LOS, but some places suffer from a good percentage of outage behind some buildings, due to the intensive high obstructions [8].

2.1.3.1. Comparison between 5G coverage and earlier generations. The study in [39] presented a comparison between 2nd, 3rd, 4th, and 5th generation cellular networks in terms of their coverage. Cell radii were 538 m, 372 m, 334 m, and 200 m for 2G, 3G, 4G, and 5G networks, respectively. Measurements showed that terminals located at cell edges faced problems in 2G, 3G, 4G, but were nonexistent in 5G [30]. This was a result of two things: the rounded shape of the cell area (using three directive antennas at the TX), and the fact that inter-cellular interference is less evident due to the high path loss of mm-waves. This observation entails that 5G systems are highly likely to be noise limited and not interference limited [30].

2.1.3.2. Coverage and outage in rural environments. For rural environments, it is better to use very high TX antenna heights to provide larger coverage areas. In [42], it was found that measurable 73 GHz signals were detected at separation distances, ranging from 33 m to 10.8 km for LOS cases in rural areas, and from 3.4 km to 10.6

km for NLOS. Similarly, for urban scenarios, a higher TX antenna provides more coverage area, but it deprives the system from utilizing reflections from the environment in delivering the signal. This means that there will be a higher probability of outage in a given cell radius [26, 43, 44]. This is the reason why environments with low numbers of "high buildings" have higher LOS coverage but suffer from outage in NLOS cases. The aforementioned observations imply that there is a need for adaptive antennas to be used, and that the height of the BS antennas should depend on the surrounding buildings [44].

2.1.3.3. Mm-wave coverage advantages and limitations. The above argument indicates that mm-wave systems work best with urban environments for a cellular radius of 200 m [8, 30]. For indoor scenarios, measurements in [10] showed that no signal can be detected for different TX and RX floors, thus repeaters will be required. We can increase cell radii up to about 318 m if the single best beam was used (by finding the best pointing angle and utilizing the concept of beamforming). As a result, the number of base stations in the region will decrease. Since mm-wave base stations cover a smaller physical footprint, it is expected that it will be less costly to provide services to a specific region using mm-wave systems, compared to that of current UHF systems [39]. Another advantage of using mm-waves on coverage stems from their property of having very short wavelengths; while objects that can block links for lower frequency signals will also block mm-wave signals, similar sized equipment will give mm-wave systems an advantage. The use of subarrays in mm-wave systems, for example, makes it possible for signals to propagate through small openings, which are otherwise seen as blockages in lower frequency systems (sub 6-GHz) [32].

2.2. Penetration, Reflection and Scattering Measurements

For both NLOS and urban environments, electromagnetic waves will face obstacles as they propagate. Some of the waves' will penetrate through the obstacles, whereas part of the signal will be reflected because of the difference of conductivity and permittivity between the different media. The direction of wave transmission and reflection depend on the incident angle of the wave at the interface, as well as the differences in electrical properties between the two media. Penetration loss is the attenuation of the signal caused after it penetrates through an object, while reflection loss is the loss of the signal after it is reflected from an object. The amount of reflected power is also affected by the size and the shape of the object obstructing the signal, as

well as the polarization of the signals as they pass through [32]. In case the reflector object is rough, the reflected signals scatter in many different directions. Measurements in [45-47] show that more scattering is connected to rougher surfaces and higher frequencies, leading to higher scattering. They also show that larger angles of incident lead to larger reflections, and thus a greater magnitude of reflection coefficients. Moreover, wet surfaces have higher penetration loss and more scattering than dry surfaces.

Performing penetration and reflection measurements can assist in creating models to predict the effects of obstacles, and that is necessary in the design and implementation of any mm-wave wireless communication system [8, 19, 48]. The phenomena of wave penetration and reflection could be explained using electromagnetic plane wave theory. In general, penetration losses increase when material's conductivity increases, and/or when the material itself is a composition of many different electro-type materials. In addition, the number of obstructions for indoor wave propagation determines the extent of penetration losses [49].

2.2.1. Penetration and reflection measurements for building materials. Studies have shown that metals and bricks have high penetration losses, whereas wood and glass have low penetration losses [49, 50]. In addition, the direction of incidence affects the penetration loss [52]. Measurements show that there is great variation in penetration and reflection losses among mm-wave frequencies, much higher than in UHF frequencies. Given this knowledge, a new requirement is imposed in order to find the best direction of wave propagation within an indoor environment for maximum intended coverage.

The measurements conducted in [51, 52] show that signal penetration through concrete is extremely small, but it is higher in wood. In general, the material used to separate between indoor and outdoor environments has a larger reflection coefficient compared to indoor material, since outdoor material generally contains thick and dense metal layers. For example, non-tinted glass has a much higher reflection coefficient than tinted glass [49]. Higher reflection coefficient entails higher penetration losses since more power will be reflected, leaving what is left to penetrate through the medium [49]. In [52], the authors found that Styrofoam and wooden doors have negligible penetration losses. The provided information about such material gives an insight about environments in which repeaters are not required.

2.2.2. The relation between frequency and penetration loss. Many conducted research results support the hypothesis that an increase in the frequency of the signal results in an increase in the penetration losses. This is related to the fact that the wavelength of the electromagnetic signals becomes smaller as the frequency increases, causing signals to suffer from a larger number of interior reflections and scattering while passing through the material [52]. Furthermore, increasing the thickness of the material will increase the penetration losses, following what has been mentioned in [53]. At mm-wave frequencies, such as 73 GHz range, communication could be suitable in indoor environments where there is only non-tinted glass, wooden doors, and a small number of obstructions [8].

2.2.3. Cross-polarization effect on penetration loss. Some papers performed penetration losses measurements involving co- and cross-polarized antennas to find out their effects on the penetration losses. It was found that using cross-polarized antennas results in lower penetration losses for closet doors, steel doors and whiteboard walls when compared to co-polarization. Other research showed that penetration losses for walls were not affected by antenna polarization, whereas penetration losses for glass were increased when using cross-polarized antennas [8].

2.2.4. Advantages and solutions for high penetration loss of mm-wave.

The reflective material makes outdoor-to-indoor (O2I) communication a great challenge for mm-wave systems. The use of relays, ultra-wideband repeaters and access points is required to solve this problem [8, 49]. Some repeaters' behavior for 28 GHz is studied and presented in [25].

In addition, the high penetration losses between indoor-to-outdoor (I2O) environments have the advantage of allowing handhelds to use the same carrier frequency without leakage or interference with the different environments. This means that the same carrier frequency can be used at the same time for a nearby indoor and outdoor environment without resulting in interference, further increasing the capacity of the channel.

2.2.5. Penetration loss models. To be able to predict penetration losses for designing purposes, some penetration loss models have been developed. 3GPP came up with several models, and their parameters can be found empirically. Penetration loss models for different materials for O2I cases are summarized in [12].

2.3. Small-Scale Channel Characteristics

As mentioned before in this report, to understand small-scale channel effects of wireless systems, the channel's impulse response (CIR) is one of the most important characteristics to measure. This is not only describing the response of the channel, but also helps in predicting the channel's time-varying and frequency-varying effects on the transmitted signal. The two most commonly used parameters in small-scale measurements are the power delay profile (PDP) and root-mean squared (RMS) delay spreads. PDP shows the multipath components and their delays and scales. The RMS delay spread measures channel dispersion over time. Both quantities will be explained more later. This section is divided into three parts. The first part talks about channel sounding techniques used for small-scale measurements. Then, small-scale measurements results reported in the literature are discussed. Lastly, small-scale channel models are described.

2.3.1. Channel sounding. Many papers discussed the channel sounding techniques used for mm-wave measurements [54-56]. The easiest way to sound the channel is to send a wideband signal known by the receiver through the channel and then cross correlate the received signal with a copied replica of the transmitted signal. Another way for sounding wireless channels is through the use of sliding correlators, which can be built by using simple components [54]. The transmitter segment consists of a pseudo-noise (PN) generator connected to a mixer for up-conversion. A PN sequence is a periodic wideband deterministic, but looks, random signal that is only highly correlated with itself which means that the output of the cross correlation of the PN signal with any other signal except itself is almost zero. For the receiver segment, the same PN signal generated at the transmitter's side must be re-generated, but with a slightly lower clock rate. The bandwidth (BW) of the signal depends on the clock rate of the signal. This signal will be mixed with the received signal. The received signal will go through a filter with a cutoff frequency of f_c/γ. The filtered signal will thus be proportional to the CIR but dilated by a factor of γ [56], which is defined as shown in equation (2.1):

$$\gamma = \frac{f_c}{f_c - f_c'} \tag{2.1}$$

where γ is known as the sliding factor, f_c is the PN clock rate at the TX, f_c' is the PN clock rate at the RX, [54]. The specifications of the sliding correlator are controlled by three factors which are f_c, γ, and L, where L is the length of the PN sequence used. Recently, advancements in design have allowed for simpler and more effective sliding correlators. The specifications of a sliding correlator that can be used for mm-wave measurements can be found in [35]. After getting the CIR, finding the delay for each component could be done by measuring the ratio between the delay of the component and a full PN sequence period delay and multiplying it by the period time length, that is the number of chips per period multiplied by the chip duration.

2.3.2. Review of small-scale measurement results. Many research groups have conducted small-scale measurements for mm-wave channels. In this section, we present a summary of the major efforts done in this field. In general, signals are clustered based upon their angle-of-arrival (AOA), angle-of-departure (AOD), and excess delays. Signals sharing the same clusters also usually share the same TX-RX path [9]. The first set of measurements at mm-wave frequencies were carried out at 60 GHz, such as the ones found in [6, 57]. The studies then moved to other frequencies, namely 28 GHz [8, 58], 38 GHz [8] and other mm-wave frequencies [6, 59]. Some measurements show that the first multipath component generally suffers from 20 dB loss more than the LOS component [46], giving great importance to the LOS component. In case there is none, the total power received is around 20 dB less than the case when there is a LOS component. One of the first papers that discussed this topic was published in 2006, and talked about 60 GHz indoor measurements conducted in a long corridor [57]. The results showed that the RMS delay spread of NLOS is 1.5 times that of the LOS case. More recent experiments at 28 GHz and 38 GHz showed similar results [6, 26, 60]. This means that the NLOS RMS delay spread can be predicted in urban environments by calculating the LOS RMS delay spread. In general, radio channels do not vary significantly over short distances; changes become evident when separation distances are more than 20 times that of the wavelength [57]. In [6], measurements for two outdoor scenarios using 60 GHz signal were conducted: peer-to-peer (P2P) measurements in an urban campus courtyard and into vehicles. In both cases, the RMS delay spread for LOS scenarios did not exceed one nanosecond.

2.3.2.1. Relation between antenna directivity and RMS delay spread. In [59], measurements were conducted using signals whose frequencies ranged from 81 to 86

GHz. Two scenarios were investigated: a street canyon where TX-RX separation is 685 m, and a roof-to-street scenario, where TX-RX separation distance is around 175 m. Readings were taken under both co- and cross-polarized antenna orientations. While directive antennas were utilized, the measurements picked up many multipath components, which was also observed in other measurement campaigns [58, 61, 62]. This indicated that several multipath components are still received even in the cross-polarization case. The mean RMS delay spreads for the signal's strongest pointing angles under co-polarized antennas were reduced for both LOS and NLOS cases, with a greater impact seen on LOS. A similar impact was seen at higher frequencies, but to a lesser extent. Measurements reported in [26] and [60] also support the previous observations. The fact that the mean RMS delay is greatly reduced by the strongest beam shows that it is an attractive choice to use steerable antennas, as this greatly reduces multipath time dispersion and increases SNR. In [26, 58, 62], wider antenna beam widths and lower gains were associated with higher RMS delay spreads. RMS delay spread decreases when the TX-RX separation increases.

2.3.2.2. Relation between signal power and RMS delay spread. At the edges of the cells, RMS delays are very small, which negates the need to use equalization at the signal processing part [26], saving valuable computing resources. This result also is supported by [62], as they concluded that increasing transmitted power should increase RMS delay spread at low TX-RX separation distances [60]. These results also supported the fact that cross-polarized antennas showed less reduction in the delay spread.

The results show that co-polarized antennas produce stronger multipath components, and in turn, result in greater delay spreads [10]. Moreover, the azimuth angle of arrival is more spread for short TX-RX separations for the above reason [63]. Further studies show that the RMS delay spread is lower for measurement setups where the antennas are cross-polarized. Similar to the previous reasoning, the extra losses resulting from cross-polarization weaken all the received signals, dropping the already weak multipath components to a threshold beneath the minimum detectable power of the receiver.

In [58], 28 GHz band outdoor measurements in an urban environment (New York City) were conducted. Two different TX heights were used, 7 m and 17 m. They found

that for LOS, there is an average of 7.2 unique resolvable multipath components and 6.8 for the NLOS case.

Through performing research on P2P networks and cellular channels, it was observed that carrier frequencies at 60 GHz have lower RMS delay spread than sub-GHz frequencies due to the fact that 60 GHz signals have higher attention [60].

2.3.2.3. Effects of high buildings on RMS delay spread. For cellular channel measurements, high buildings can lead to higher delay spreads. In addition, smaller TX azimuth pointing angles result in lower delay spreads. It is preferable to have lower RMS delay spreads so that the need for complex equalizers at the receivers can be avoided.

2.3.2.4. RMS delay spread for wide streets and areas. Wide streets are associated with more multipath components with detectable power levels, resulting in an increase in the RMS delay spread. This is caused by the many reflectors faced by the signals, such as cars, traffic signs, buildings, and so on present in the environment [61].

2.3.2.5. Effects of reflectors on AOA. High reflections occur in mm-waves caused by reflective materials resulting in enhancing outdoor coverage and increasing the range of AOA between TX-RX links. This is possible because the reflective material does not allow signals to pass through, and hence reducing penetration greatly; the signals will bounce off several buildings to reach the destination rather than having to pass through them and lose a larger portion of the signal's energy, resulting in enhanced outdoor coverage. The reflected signals will also arrive at the destination from a larger array of directions, leading to an increase in the AOA, when compared to an environment with little or no reflectors. Higher AOA leads to higher received power since power will be received from more directions [49].

2.3.2.6. Mm-wave small-scale aspects: Conclusion from measurements results. The mean and variance of RMS delay spread under different scenarios are summarized in Appendix B for LOS and NLOS measurements, including those that consider only the best pointing angles. Based on the majority of the results in the tables, choosing the pointing angle in the best LOS scenario yields a much lower RMS delay spread, and hence an improvement in the system performance. For NLOS cases, choosing the best pointing angle reduces the RMS delay spread but not as much reduction as observed in a LOS environment. The reason behind this is the fact that received signal in NLOS

case mostly comes from reflections, not from the LOS component. Thus choosing the best pointing angle will not reduce the number of reflections significantly, while having a better pointing angle in LOS will strengthen the main component that reaches the receiver, and reduces the reflected signal power. Furthermore, increasing the carrier frequency also results in the same observation as shown by the measurements; as frequency increases the RMS delay spread decreases. Again, the greater losses resulting from the higher frequency carriers drop the reflections' power significantly. It should be noted that other phenomena might become more evident at higher frequencies due to the change in the wavelength, ultimately affecting the RMS delay spread.

2.3.3. Small-scale channel models. There have been many attempts to improve the accuracy of characterizing the behavior of wireless channels using mathematical models [62-65]. The CIR of any communication medium can be written as the sum of several impulses, each experiencing a certain time shift and amplitude scale [66]:

$$h(m, L) = \sum_{l=0}^{k-1} \alpha_l(L)\delta(m - m_l(L)). \tag{2.2}$$

Here k, α_l, m_l and L represent the total number of multipath components, l^{th} path amplitude, l^{th} path spatial shift and time or spatial location, respectively.

The channel characteristics are not the only small-scale effects that the signals undergo; the antenna radiation patterns of both TX and RX antennas also affect the PDP at the receiver. In fact, the PDP at the receiver is the result of the convolution of the CIR of the channel with the antenna radiation pattern at both TX and RX [63]. Studies in [64] stated a method to eliminate the effects resulting from imperfections in the antenna radiation patterns.

To characterize the wireless channel, TX and RX pointing angles should be taken into consideration, since antennas do not usually have ideal isotropic radiation patterns. Studies have appeared where people attempt to find the PDP as a function of azimuth and elevation angles. While the study in [63] did not consider the elevation angle, the PDP was obtained utilizing the azimuth angle. The PDP as a function of elevation rotation is given as [63] ,

$$\text{PDP}(\tau) = \left|\sum_{i=1}^{N} h_i(\tau)\right|^2. \tag{2.3}$$

Here h_i is CIR found at the index i. The detailed model of power azimuth delay is shown in [62] and [63]. It can be used to find the PDP for power angular window, where a window is selected to capture most of the power of the signal in the spectrum. Additionally, the angular spread of arrival can also be extracted from the PDP [62]. In [67], COST 2100 channel model and its parameters extracted. Parameters of the models were not found for mm-wave before [66] had published them using 28 GHz carrier frequency.

One way to know whether the channel has a large number of multipath components or not is by measuring the RMS delay spread and using the PDP [10, 65, 66]. Finding the RMS delay spread is important to have a good measure of the coherence BW nature of multipath channel and severity of inter symbol interference. Delay spread and RMS delay spread equation derivation provided in [68]

Measuring the RMS delay is also important to be able to design the equalizer at the receiver [10]. Several models that are used to calculate RMS delay can be found in [66]. The RMS delay spread has been modeled by cumulative distribution functions based on different distributions: Log-normal, Weibull, Rayleigh, Rician and non-parametric distributions. The non-parametric model is the best representation of the RMS delay spread, as it indicates the rapid variation of the channel [66].

In [69], two spatial statistical channel modeling concepts were used, namely “time cluster” and “spatial lobe”. Using only one modeling concept as a representative is not enough to encompass the channel characteristics. There is the possibility that multiple signals from different paths or directions may arrive to the antenna belonging to the same cluster.

Both 3GPP and WINNER 2 models assign only one-time cluster to each AOA. As the number of the clusters decreases, the number of sub-paths per cluster increases and vice versa. The number of clusters is mainly dependent on the measurement’s scenario, such as street canyons or malls.

Based on a study done in [70], the average number of clusters in urban environments is around 3.6. Using this information, it can be seen that a good way to characterize or categorize the channels can be by looking at the number of clusters they possess. Moreover, some models have been extracted from ray tracing techniques; such models utilize geometry and some prior assumptions such as the one used in [71]. Small-scale

parameters usually follow statistical models. A summary of the parameters and their statistical Models is given in Table 2.1 [70].

Table 2.1: Small-scale parameters and their statistical models.

Small-scale Parameters	**Statistical Models**
The cumulative distribution function (CDF) of the number N of clusters	Log-norm distribution
Probability Density Function (PDF) of excess delays for Urban NLOS environment	Exponential distribution
PDF of sub path delays for Urban NLOS environment	Exponential distribution
Cluster powers	Single Slope Exponential Decay
RMS delay and sub path delay spreads σ DS	WINNER II
PDF of the cluster's AOD	Laplacian distribution

Chapter 3. Large-Scale mm-Wave Channel Characterization Measurement Campaign for Indoor and Outdoor Environments

The first step necessary to comprehend wireless channels is by implementing large-scale measurements. Both Indoor and outdoor measurements were conducted using a carrier frequency of 28 GHz at the American University of Sharjah (AUS). In this chapter, the set up used for conducting large-scale measurements, the measurement scenarios, and the results are presented and discussed.

3.1. Measurement Setup

The large-scale measurements' setup consisted of a transmitter (TX) and a receiver (RX) equipment. Both the TX and RX are mounted on a trolley for mobility purposes. The transmitter is composed of a 14 GHz single tone generator connected to a frequency doubler with a 14-dB conversion loss. The frequency doubler's output is a 28 GHz single tone signal. The doubler is followed by a WR-28 15 dBi horn antenna. The horn antenna is mounted on a tripod. Similarly, the receiver has a WR-28 horn antenna that is fixed on a tripod but is connected to a 16 dB low-noise amplifier (LNA). The LNA output is down-converted by a mixer with 12 dB conversion loss. The mixer combines the received signal with a 22.5 GHz oscillator's signal; then the mixer's output is captured by the spectrum analyzer to measure the output power at 5.5 GHz. A block diagram of the measurement setup is shown in Figure 3.1. More details about the used equipment are shown in Table 3.1.

Furthermore, throughout the measurements, both transmitter and receiver antennae heights were fixed at 1.45 m. The path loss measurements were conducted from April to June 2018 and from December 2018 to January 2019.

Table 3.1: The details of the components used for large-scale measurement's TX and RX.

Component	Manufacturer and Model Number	Details
Amplifier	HD Communications Corp-HD30172	24 dB gain with 13dBm saturated power
Mixer	Marki Microwave-M2-0240	12 dB convergent loss
Oscillator	Cernexwave-42S35FOO	22.5 GHz with 10 dBm output power
Antenna	Cernexwave –Waveguide Standard Gain Horn Antenna	30° beam width with 15 dB gain at Ka Band

3.2. Indoor Measurement Scenarios and Results

Indoor for path loss measurements were conducted on the AUS campus to characterize the mm-wave channel in different indoor scenarios. The AUS campus was chosen due to the wide variety of different indoor environments. This consists of diverse labs containing different sets of equipment as well as environments encountered during everyday life, such as classrooms, corridors, and halls. As a result, the collected measurements could be used to describe a large array of indoor scenarios. Indoor scenarios in AUS could be classified into four types as follows: laboratories, narrow corridors, lecture halls and wide building rotundas. Each indoor location has both its construction properties and channel characteristics aspect that will be discussed in the following sections. For consistency, the measurements were gathered in environments during times at which people were not present to disrupt or affect the measurement taking process.

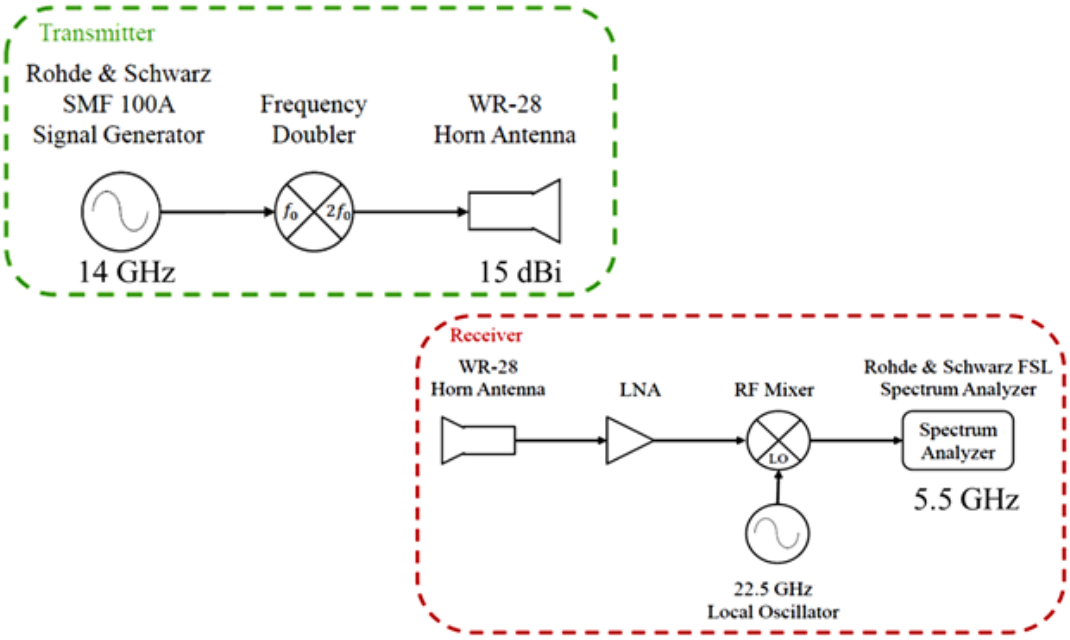

Figure 3.1: Block diagram of the measurements system.

3.2.1. Laboratories. Laboratories at the AUS are located on the basement of the building. Most of them contain computers and devices placed on wooden tables. The labs have at least two wooden doors with small offices located inside them. Circuits and Microwave labs had been chosen for large-scale measurements. The main

difference between these labs is their area, the equipment, and the organization of the instruments. Figure 3.2 shows the interior of the three labs.

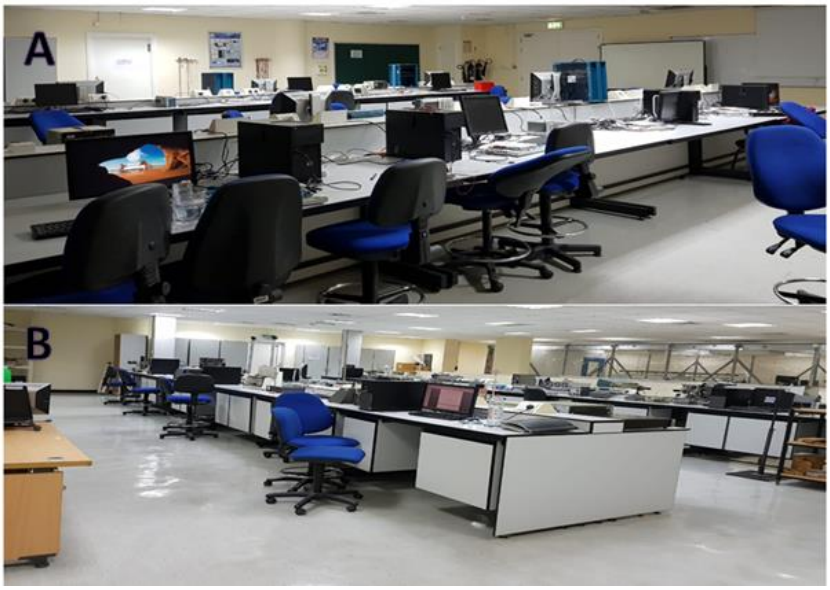

Figure 3.2: A) The interior of Circuits Lab. B) The interior of Microwaves Lab.

Line-of-sight measurements were conducted under different TX-RX separation distances in Circuits and Microwaves labs. The transmitted power for both measurements was 5 dBm. The top view measurement setup diagrams for Microwaves and Circuit labs are shown in Figure 3.3 and Figure 3.4, respectively. The side view of a single measurement diagram is shown in Figure 3.5. Figure 3.6 shows the relationship between received power and the TX-RX separation distance for LOS measurement. It is noticeable from Figure 3.6 that as the distance increases, path loss also increases and the deviation between powers received at the same distance for each lab increases. The best-fit lines for both measurements are found in the graph for the LOS case. From Figure 3.6, several observations can be drawn about channel characteristics for laboratories under the LOS case. The increase of the TX-RX separation distance resulted in more variations in the received power and greater differences between best-fit lines of two lab measurements. From this observation, it is evident that if TX-RX separation distance increased, the effects of the lab environments on the signal levels are amplified. The other observation is that both labs have very similar path loss behavior. For instance, the difference between the best-fit lines at 9 meters TX-RX

separation (the largest TX-RX separation in Circuits lab) is less than 1dB, which is a minor difference. Thus, we expect underground lab environments with similar areas to have similar path loss characteristics.

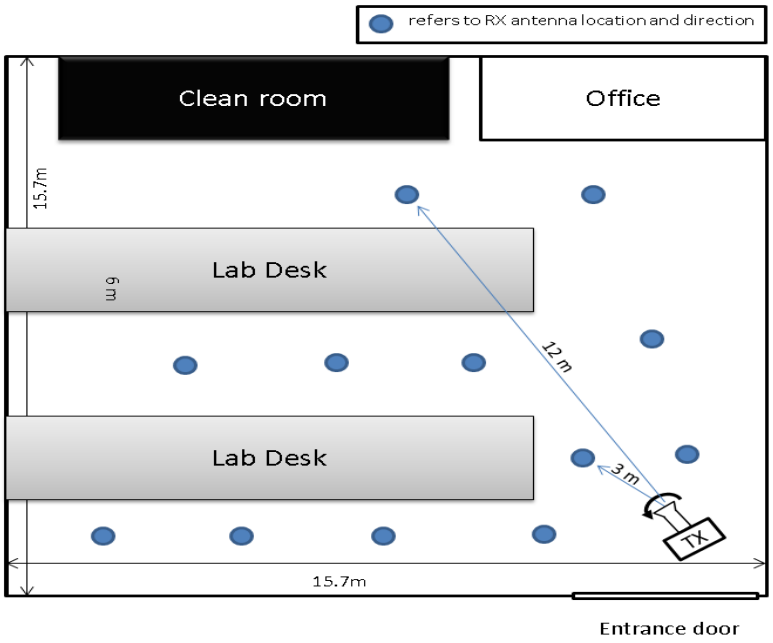

Figure 3.3: Microwave Lab top view measurement setup diagram.

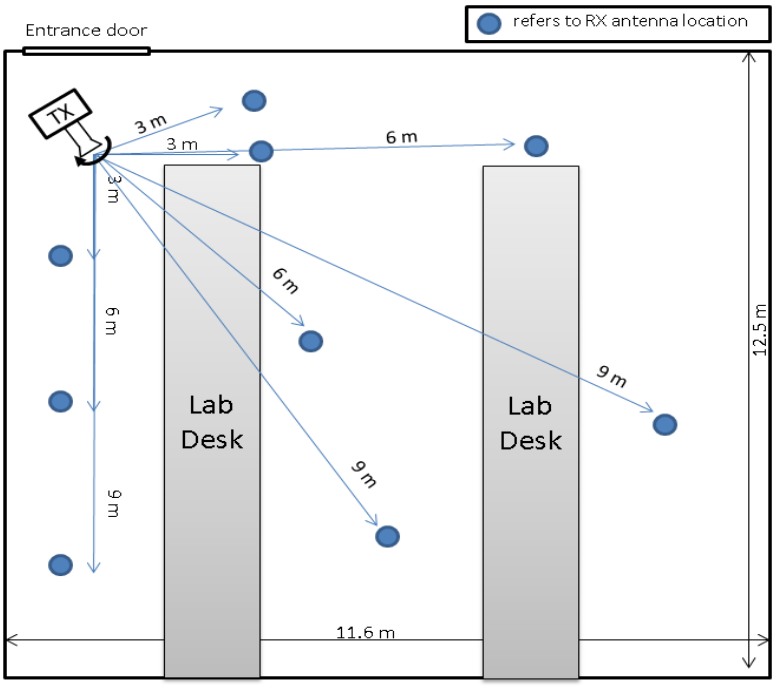

Figure 3.4: Circuit lab top view measurement setup diagram.

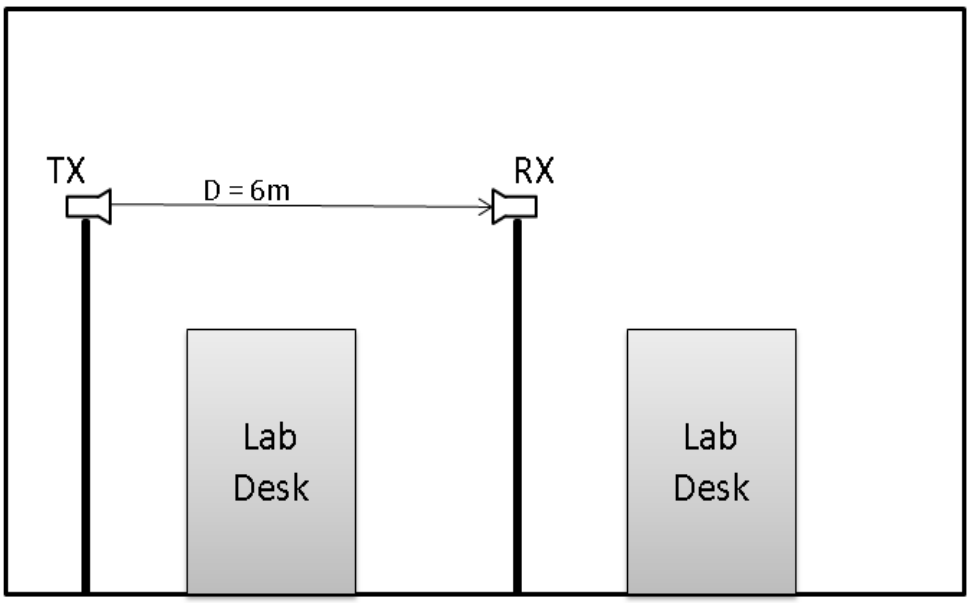

Figure 3.5: Single point labs side view measurement setup diagram

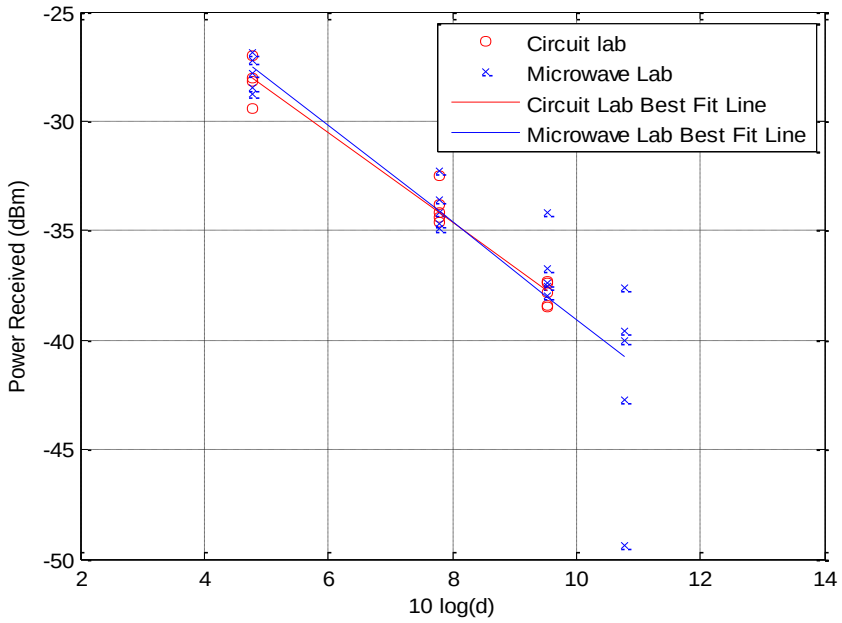

Figure 3.6: Received power loss measurements in Circuit and Microwave labs.

The calculated path loss exponent (PLE) from the best fit line in LOS measurements was 2.2 for the Microwaves lab, and 2 for the Circuits lab which are close to the PLE exhibited by free-space (FS) scenarios, which is 2. Equation 3.1 used to find the PLE is given below as,

$$PL_{\mathrm{dB}} = PL_{\mathrm{dB}}(1\ m) + 10\ n\ log_{10}\left(\frac{d}{1\ m}\right) \tag{3.1}$$

where $PL_{\mathrm{dB}}(1)$ is the path loss at one meter TX-RX separation distance and n is the PLE. This result is important since it made it possible to model or to expect the behavior of signal power in laboratories or similar scenarios. It was expected to have PLE close to 2 since the experiment utilized directive antennas and the labs' environments are not very reflective. Thus, some of the multipath components were added to the LOS component. The result of this summation has higher power level than LOS component power level. Microwave lab has higher PLE since it is more populated with metallic equipment and components that can cause several reflections or could block some of the multipath components. It was expected that the PLE would decrease with the increase of TX-RX distance in these labs, since more multipath components will be present along with the LOS components. The standard deviations of labs received power measurement were calculated to be 0.786 dB and 2.52 dB for Circuits and Microwave labs' measurements, respectively.

3.2.2. Corridors. Corridors are usually best described as long narrow paths connecting two or more rooms, building, halls or any type of indoor construction. Two corridor measurements have been conducted at the AUS. The first measurement was conducted in Engineering Building 2 (EB2) basement, which resides next to Communication Lab. The other was conducted in the underground tunnel between the Main Building and the Student Center.

The EB2 corridor is around 45 meters long, 3 meters high and has a width of 2.5 meters. There are offices and labs around this corridor, where some wooden doors have different dimensions. This corridor does not have a constant width and intersects with another corridor. In addition, aluminum and glass doors divide the corridor into two smaller sections; these were always kept open for the sake of consistency. Regarding the underground tunnel, it is around 60 meters long, 3 meters in height, and has a width of 2.5 meters. There were several metallic fans along the ceiling of the tunnel connected to the sides of the wall, one of which is indicated by the orange circle in Figure 3.7. In the middle, the tunnel's height varied by about 25 cm. The corridor and the tunnel pictures are shown in Figure 3.7 and Figure 3.8, respectively. LOS measurement was conducted in four stages. First TX was fixed at one side of the corridor/tunnel while the RX was being moved from the opposite side towards the TX.

Then the RX was fixed at the opposite side while the TX was being moved this time towards the RX. After that, the TX and the RX were swap and the procedure explained earlier was carried on again. The top view of the four measurement setups used for both corridor and tunnel is shown in Figure 3.9. The received power results are demonstrated in Figure 3.10.

Figure 3.7: The Underground Tunnel.

Figure 3.8: The Engineering Building Corridor.

Figure 3.10 shows that the path loss for both the EB2 corridor and underground tunnel are very close even though they have different dimensions and surrounding material and objects.

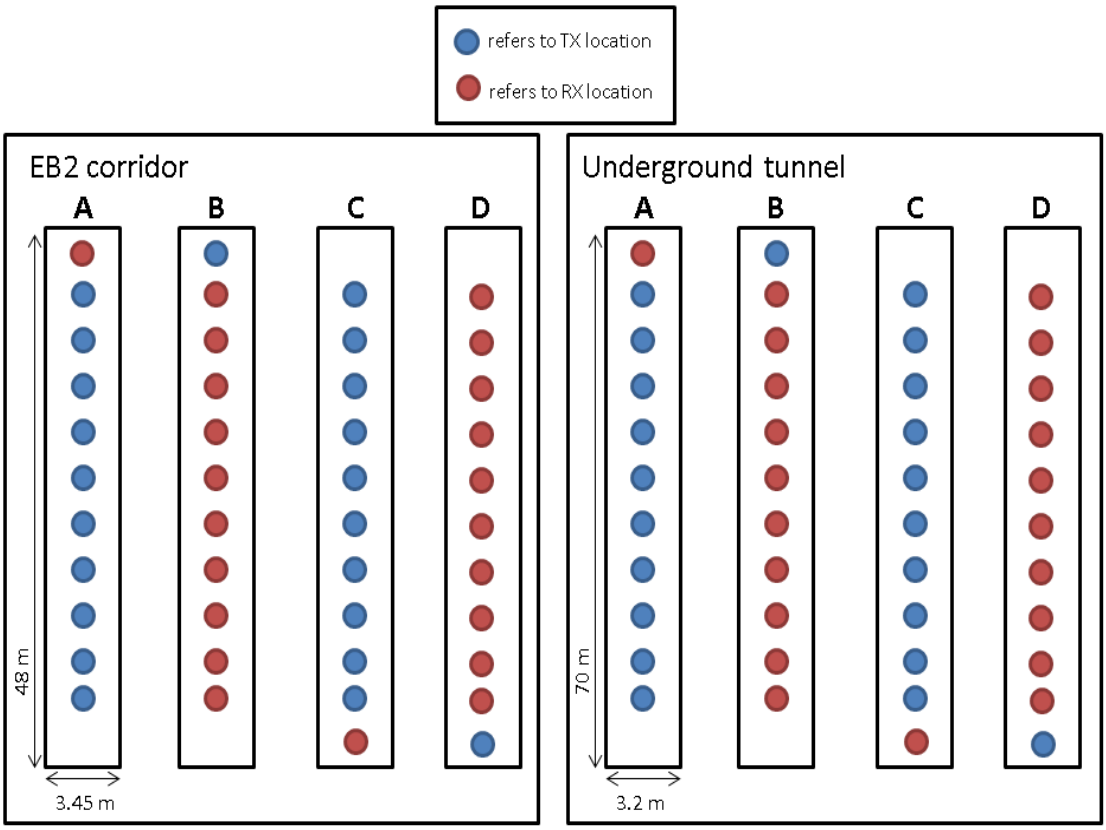

Figure 3.9: EB2 Corridor and the Underground Tunnel top view measurement setup diagram.

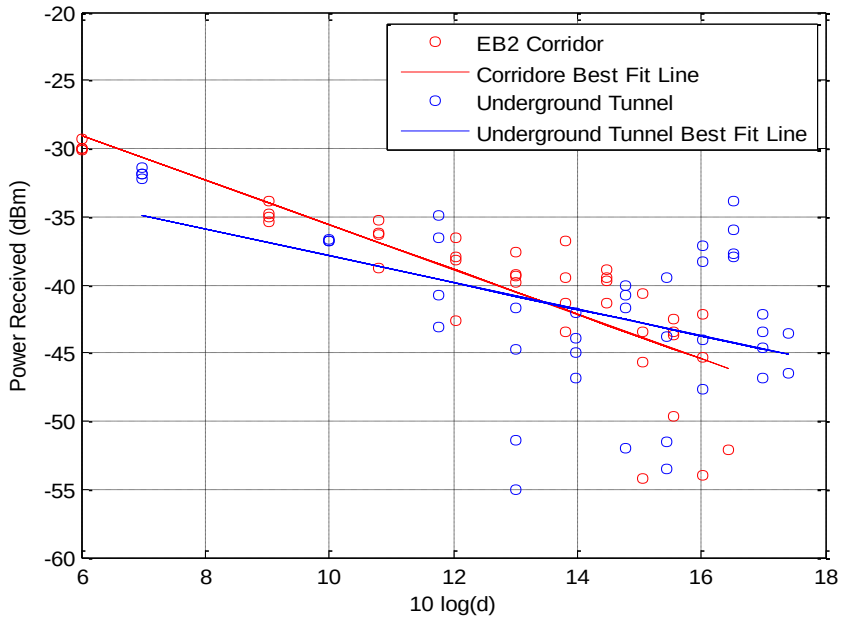

Figure 3.10: Received power LOS measurements in EB2 Corridor and the Underground Tunnel.

Furthermore, the path loss exponents in corridor and tunnel scenarios were lower than the free space scenario. The path loss exponents found for the EB2 and tunnel are 1.64 and 0.98, respectively. It was expected that the tunnel would have the lowest PLE among all indoor scenarios since it had highly reflective environment, allowing it to act as a waveguide to permit the signal to pass through with minimum losses. Also, since both scenarios have similar path losses, generalizing their case for all corridors and narrow indoor scenarios is possible. Thus, predicting the path loss in any corridor scenario without previous measurement will be simple task. In addition, by observing Figure 3.10 it can be concluded that at low TX-RX separation distances, the received power is lower than the best fit line, while it was higher when TX-RX separation distance increased. This proves that the narrow corridor acts as a waveguide, and the energy inside it was somehow conserved, that is the difference between the highest and lowest received power was small. The standard deviation for the corridor measurement and tunnel measurements are found to be 3.2 dB and 5.3 dB, respectively. The high standard deviation for tunnel scenario caused by the metallic fans that affects the received power at the points surround it.

3.2.3. Lecture halls. Lecture Halls are known as indoor scenarios where lectures or presentations are held. They are similar to classrooms but have a bigger space and a higher student capacity. Three halls were used for path loss measurements EB1-030, Lecture Hall A and Main Auditorium. The capacitance of EB1-030, Lecture Hall A and Main Auditorium is 158, 113 and 1000 seat respectively. EB1-030 is a small hall with a large whiteboard in the front side. The TX was placed at the top right of the hall and LOS path loss measurements were conducted. Regarding Lecture hall A, it was very similar to EB1-030, but it was narrower and longer. The TX was placed at the entrance of the lecture hall for LOS path loss measurement. The Main Auditorium was much bigger than the previous two halls. Its ceiling descends slowly as we get closer to the stage. The TX was placed exactly in front of the main entrance. Figure 3.11 shows that the three halls demonstrate a difficulty of moving TX and RX setups in such environments. Thus, lower number of measurement points have been taken. The top view measurement scenario diagram for Main Auditorium, Hall A and EB1-030 are shown in Figure 3.12, Figure 3.13 and Figure 3.14 respectively. The received power vs TX-RX separation distance is shown in Figure 3.8.

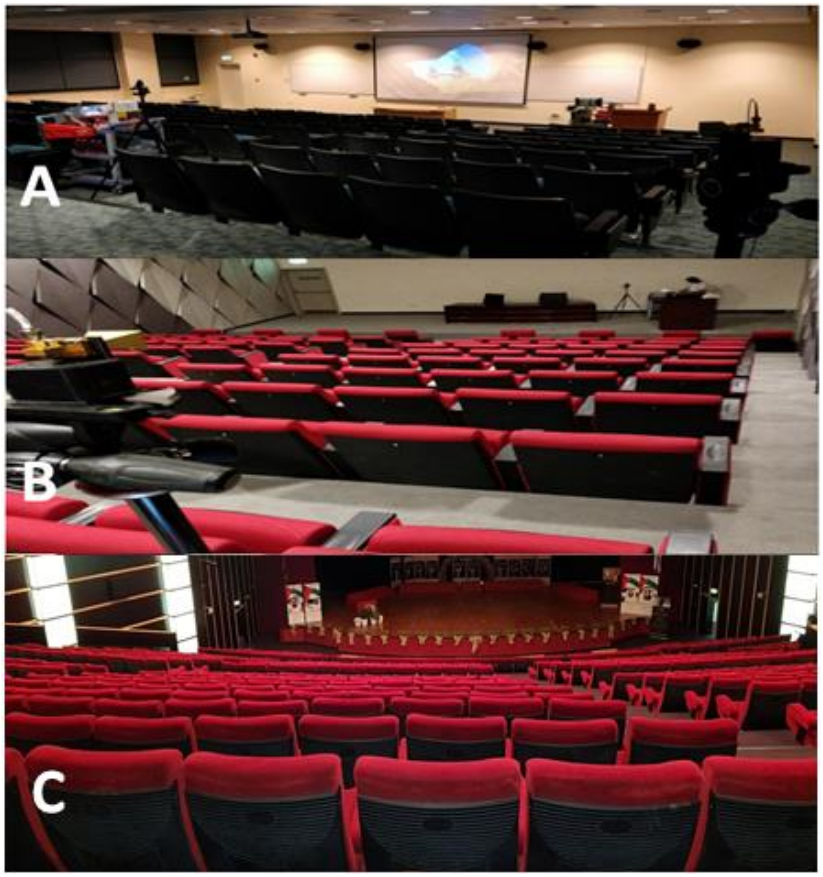

Figure 3.11: A) The interior of EB1-030. B) The interior of Lecture Hall A. C) the interior of Main Auditorium.

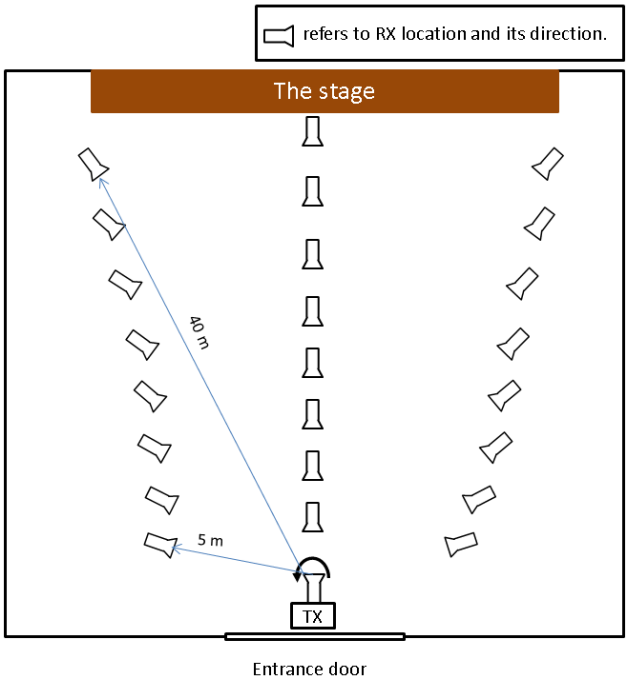

Figure 3.12: Main Auditorium top view measurement setup diagram.

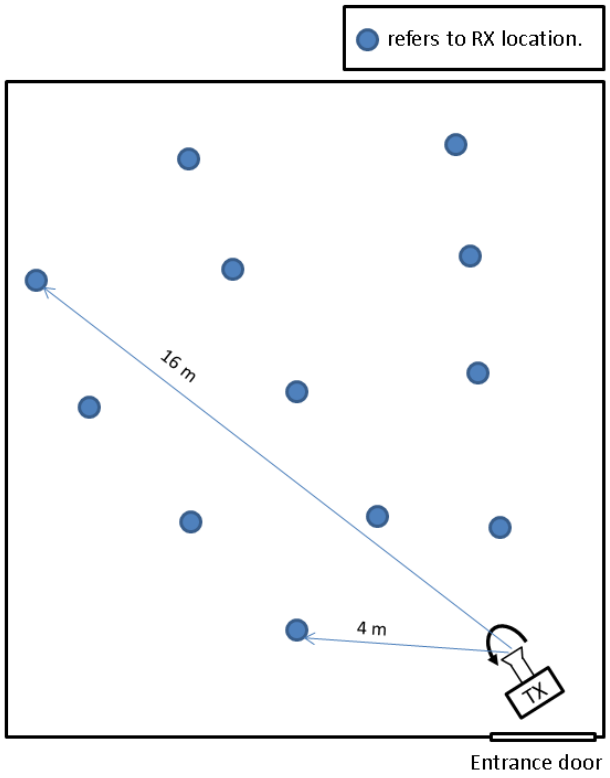

Figure 3.13: Hall A top view measurement setup diagram.

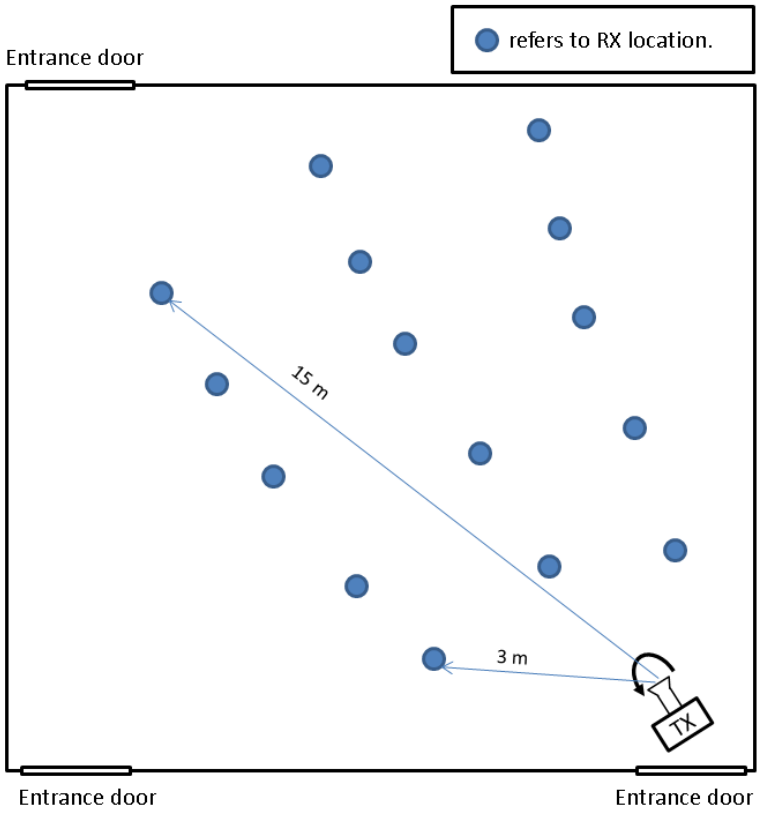

Figure 3.14: EB1-030 top view measurement setup diagram.

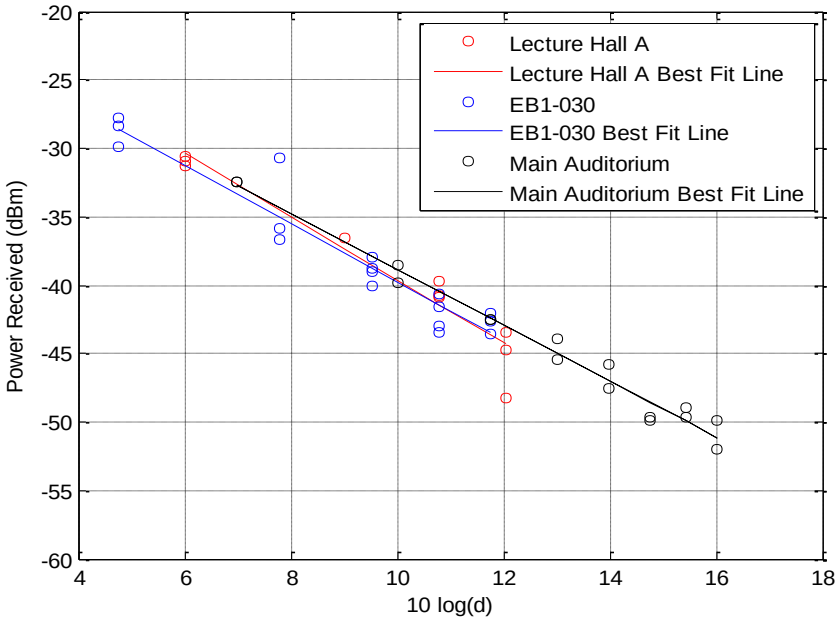

Figure 3.15: Received power LOS measurements in halls.

Figure 3.15 shows that the path loss in big lecture halls were very close to each other for same TX-RX separation distances. Another observation is that when TX-RX separation distance becomes very high, the increase rate of the path loss becomes weaker relative to smaller separations. The PLE for the best-fit line of Lecture Hall A, EB1-030 and Main Auditorium were 2.3, 2.1 and 2 respectively. In addition to that, the received power was increased when RX was closer to walls. The standard deviation of the Hall A, EB1 hall and Main Auditorium were 1.5 dB, 1.56 dB, and 0.85 dB, respectively. The standard deviation for the Main Auditorium is very low because it's very spacious hall where objects inside it is almost distributed the same way in its entire area.

3.2.4. Wide building rotunda. A wide building rotunda is known as a large circular hall or room in a building with a highly elevated ceiling, for example a dome. Two buildings were used for LOS path loss measurements. The first building was EB2, whereas the second building was the university's Main Building. The major differences between these two buildings are that the Main Building was much bigger than EB2 and had a higher ceiling. The pictures of the interiors of both buildings are shown in Figure 3.16 and Figure 3.17. Both TX and RX were non-stationary. The received power vs the TX-RX separation distance was shown in Figure 3.18.

Figure 3.16: EB2 Rotunda.

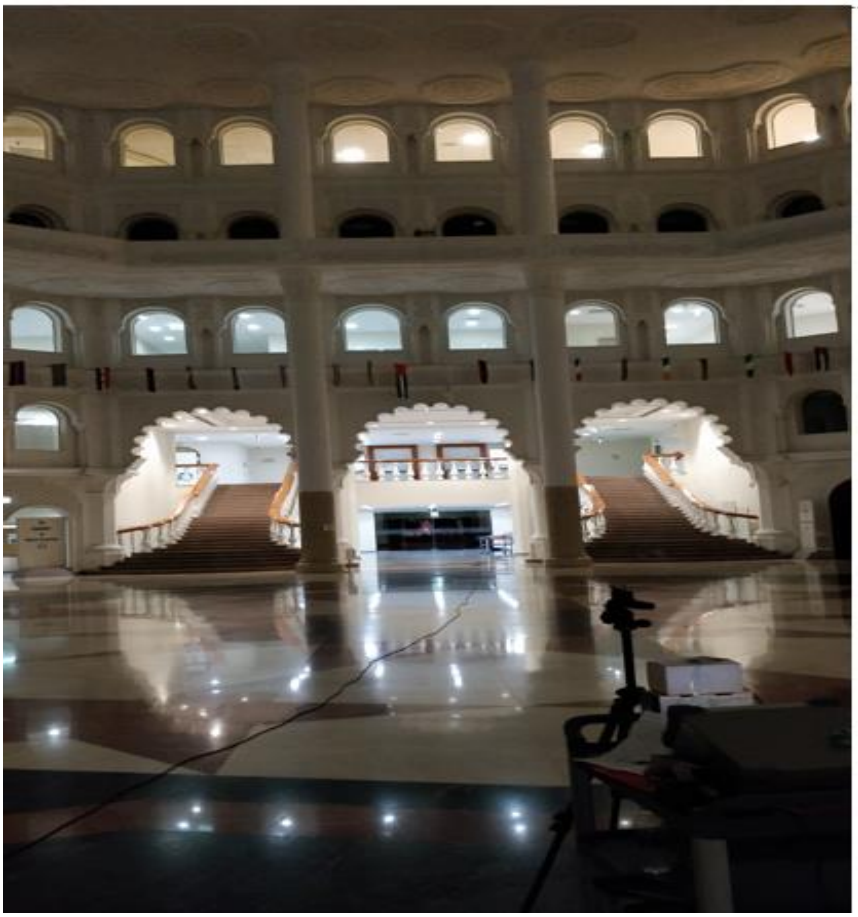

Figure 3.17: Main Building Rotunda.

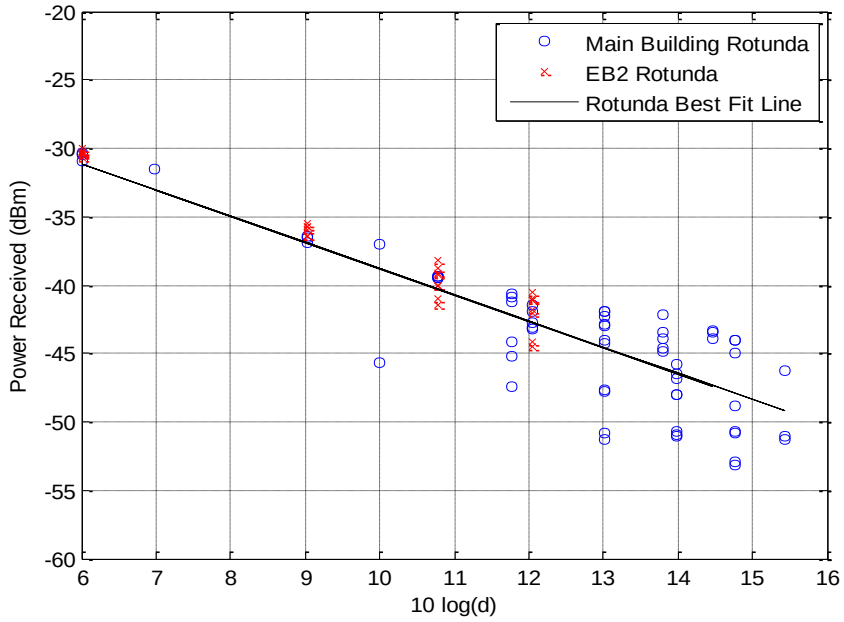

Figure 3.18: Received power LOS measurements in dome building rotunda

In Figure 3.18, it was clear that both main building's and EB2's rotundas had similar effects on the signal's power level. Thus, generalizing their results to other rotunda scenarios is possible. The PLE was found to be 1.91 for both scenarios' measurements. The PLE of rotunda scenarios is lower than FS scenario since they are close empty indoor environment where receive power is a summation of several multipath component added to the LOS component. The reason behind Moreover, the received power in EB2 was increased when the RX was close to any of the building pillars. The standard deviation for wide building rotunda is equal to 1.37 dB.

3.3. Outdoor Measurement Scenarios and Results

Outdoor path loss measurements were also conducted on the AUS campus to characterize the mm-wave channel in open area scenarios. The number of measurement scenarios chosen was not high enough to give full understanding of the mm-wave outdoor characteristics since there were no actual urban and semi-urban scenarios at AUS and not enough variety of building types, heights and landscape.

The measurement setup was the same as the one used for indoor scenarios, which was shown in Figure 3.1. Only LOS measurements were conducted where the antennas at the TX and RX face each other. For consistency, the measurements were

gathered in environments during times at which people were not present to disrupt or affect the measurement taking process. Moreover, all measurement was conducted in windy weather in temperatures ranging between 18°C and 26°C. Thus, measurement in different weathers and comparing their result could be done in the future.

3.3.1. Outdoor hallway. In this scenario, measurements were conducted in the outdoor hallway connecting the engineering buildings EB1 and EB2 at AUS. The street view of the hallway and a top-view map are shown in Figure 3.19 and Figure 3.20, respectively.

The hallway has one open side and one supported side by connected columns as shown in the figures. The open side of the hallway was highlighted by the top blue line in Figure 3.20. The closed side of the hallway is mostly composed of the exterior wall of the engineering buildings, except for an 18 meters gap between the two buildings, which is supported by columns. The total length of the hallway is 100 meters. Regarding measurements, the maximum recorded TX-RX separation distance was 42 meters. The output power of the TX was 5 dBm. The results are shown in Figure 3.21 along with the best-fit line. The PLE for this scenario was calculated to be 1.67. This value was less than the PLE for LOS free-space environments due to multiple reflections from the hallway ceiling and buildings' walls giving rise to a wave guiding effect.

Figure 3.19: Hallway between EB1 and EB2 top view.

Figure 3.20: Hallway between EB1 and EB2 Image.

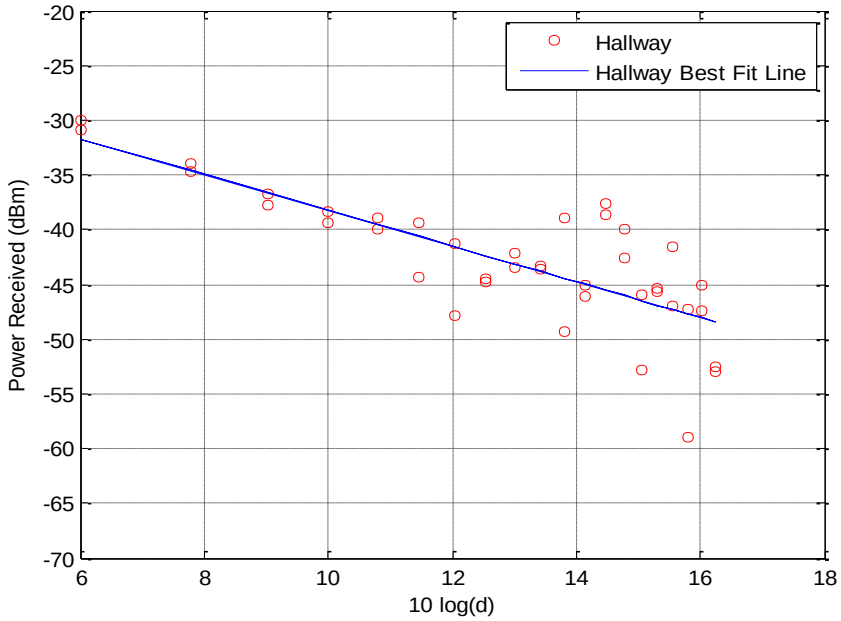

Figure 3.21: Received power LOS measurements in Hallway between EB1 and EB2.

Figure 3.21 shows that as the TX-RX distance increase, the deviation between powers received at the same distance increases. Another observation is that a relatively high-powered signal component was reflected off both the ceiling and the side construction column, which ends up reaching the RX at higher separation distances.

Thus, the received power at high TX-RX distances can be divided mainly into three components: the LOS component, the component reflected off the ground and the component reflected off the ceiling. It cannot be confirmed, however, that the side reflected components provide a major contribution to the total power received. The proof of the fact that the ceiling and the construction column are the reason behind the increase of the PLE is the fact that the received power did not decrease when the RX placed where the hallway is open sided. Moreover, ground reflection is available in most of the scenarios; which means that the only two factors that could have led to increasing the PLE for this scenario are the ceiling and side construction columns. The PLE was 1.63, which is lower than FS case, and the standard deviation was found to be 3.76 dB.

3.3.2. Low urban environment. Low Urban Environments are ones that contain a low density of buildings. Measurements in this scenario were conducted in the area between Library and both engineering buildings (EB1 and EB2). The measurement scenario was presented in Figure 3.22. LOS measurements were conducted for 80 TX-RX separation distances. The measurement set up top view diagram is shown in Figure 3.23. The measurement results are shown in Figure 3.24.

Figure 3.22: Low Urban environment used for path loss measurement.

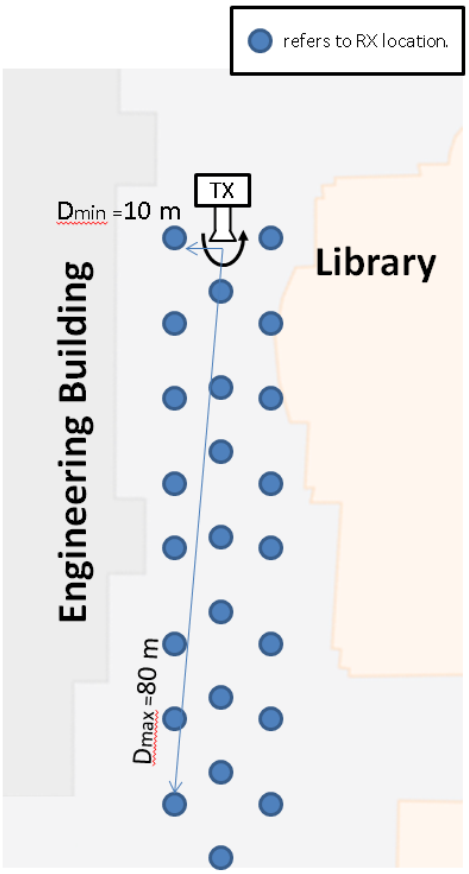

Figure 3.23: Low urban environment top view measurement setup diagram.

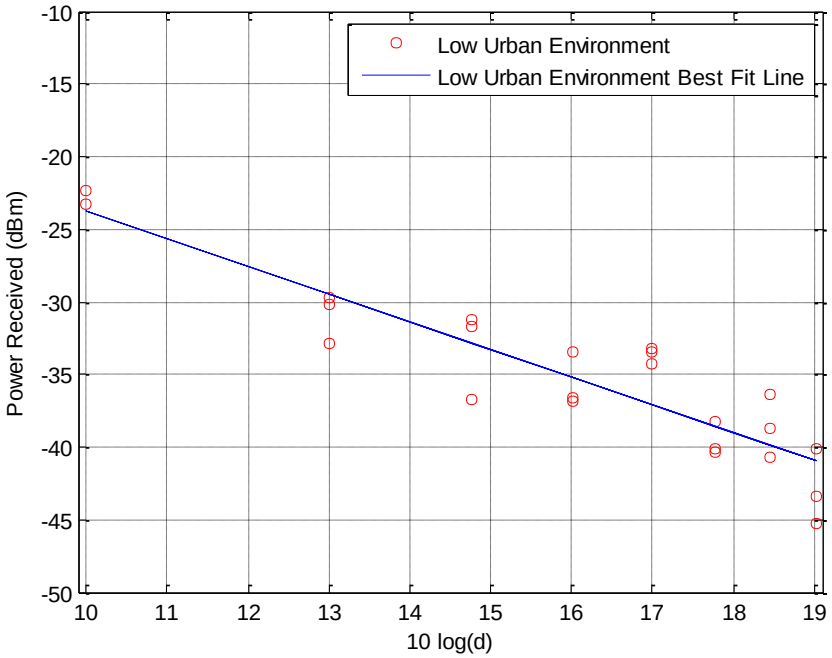

Figure 3.24: Received power LOS measurements in area between Engineering Buildings and Library.

The PLE was found to be 1.91 due to the reflected components constructively adding to the LOS component. Reflections were caused from the three buildings surrounding the measurement area. The standard deviation was found to be equal to 2.4 dB in this scenario.

3.3.3. Open area environment. Open area environments are environments characterized with the lack of almost any obstructing material, such as buildings or foliage. In this scenario, path loss measurements have been conducted at the empty parking lot at the AUS. The parking is located between the sports complex and tennis court. This parking cannot be considered a free space environment since the received signal consisted of a combination of a LOS component and a component reflected off the ground. Moreover, there is a possibility that the streetlight, tennis building, sports complex and the sidewalk might have resulted in some minor reflections. The parking image is shown in Figure 3.25. The parking lot has an area of more than 100 square meters. LOS measurements had been conducted. Measurement results are shown in Figure 3.26. PLE is found to be 1.93, which is lower than that of the FS case, but is very close to it nonetheless. It was also observed that the received power increased when the RX was close to the sidewalk. This might be due to the smooth sidewalk surface resulting in a stronger ground reflected component. The standard deviation was found to be 2.71 dB.

Figure 3.25: Parking image.

3.3.4. Foliage environment. An environment populated with foliage is one where landscape is covered by leaf bearing trees. Carrying out path loss measurements

in such environments is crucial since channel characteristics might be different from normal non-urban environments. A picture depicting the measurement scenario was shown in Figure 3.27. The area covered by the foliage was roughly 26×50 square meters. Two measurement scenarios had been conducted. For the first one, both TX and RX were located on the ground level. The TX was stationed outside the foliage area whereas the RX's location was varied. For the other measurement scenario, the TX was fixed at a height of 7.5 meters with respect to the RX. This was located on first floor of the Architecture Building. As for the RX, it was moving among the foliage. The top view measurement setup diagram is for both scenarios is shown in Figure 3.28 and Figure 3.29. The RX was moving in the dotted track shown in Figure 3.28 and Figure 3.29. The measurement results for the TX place at both the ground level and at a height of 7.5 meters are shown in Figure 3.30 and Figure 3.31, respectively. The PLEs were found to be 2.3 and 6.38 for the first and second scenarios, respectively, both of which are higher than the case of FS.

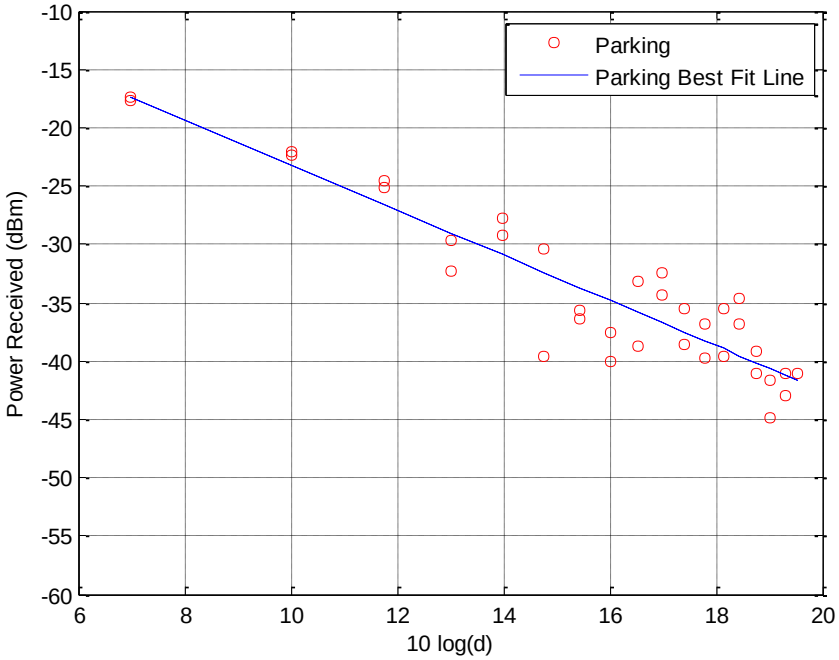

Figure 3.26: Received power LOS measurements in empty parking.

When the TX was on ground, the PLE was relatively lower than the case where TX was 7.5 meters high. The main reason that led to the higher PLE in the second set of measurements was the substantial blockage resulting from the greater number of

trees and leaves. Moreover, it had been noticed that the tree trunks cause very high attenuation, greater than the attenuation caused by the leaves. Another observation was that wind has a noticeable effect on the received power in environment populated with foliage due to the movement of the leaves.

Figure 3.27: Foliage measurement scenario image.

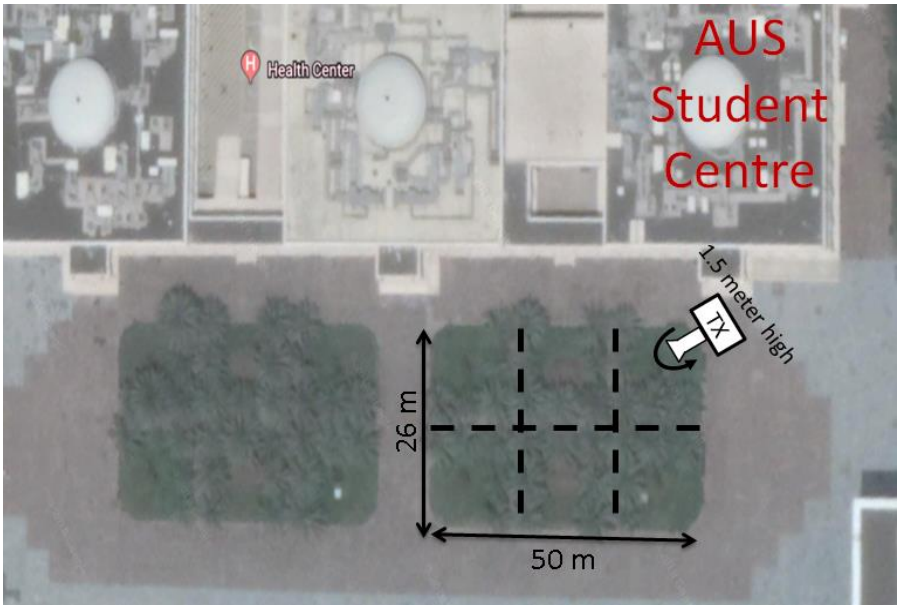

Figure 3.28: Foliage top view measurement set up diagram for 1.5 m TX height.

The received power underwent significant variations until the leaves stopped moving and shaking. The standard deviations were found to be 2.67 dB and 8.34 dB for the first and second measurements, respectively.

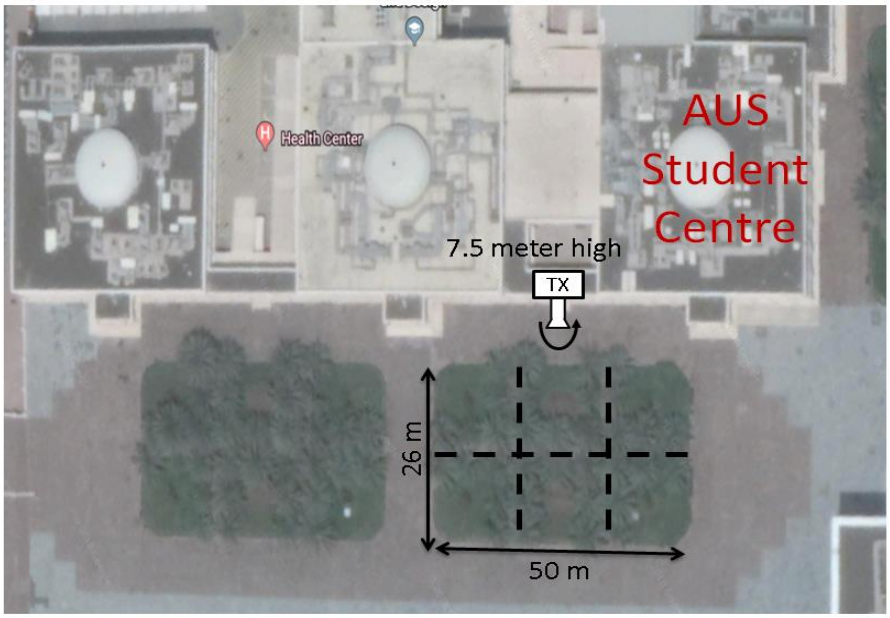

Figure 3.29: Foliage top view measurement set up diagram for 7.5 m TX height.

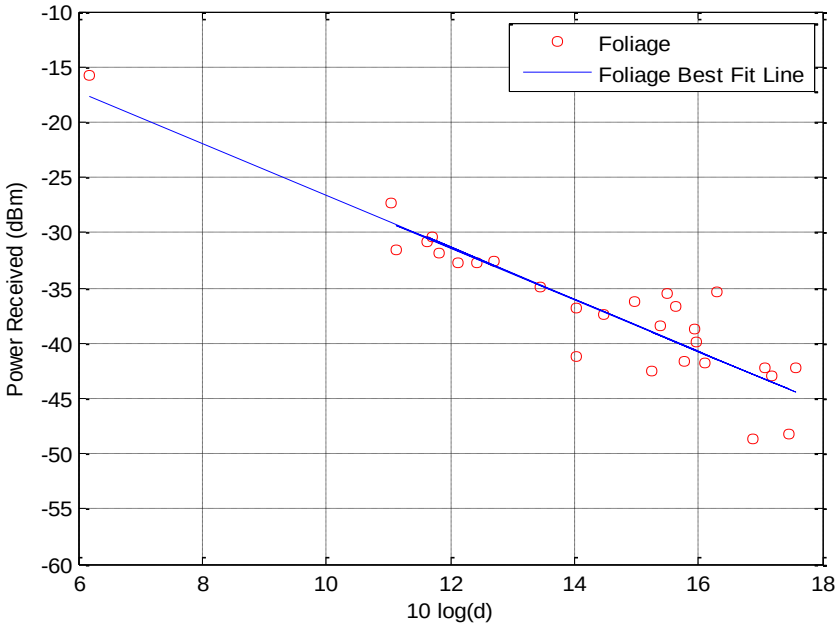

Figure 3.30: Received power LOS measurements in Foliage Environment.

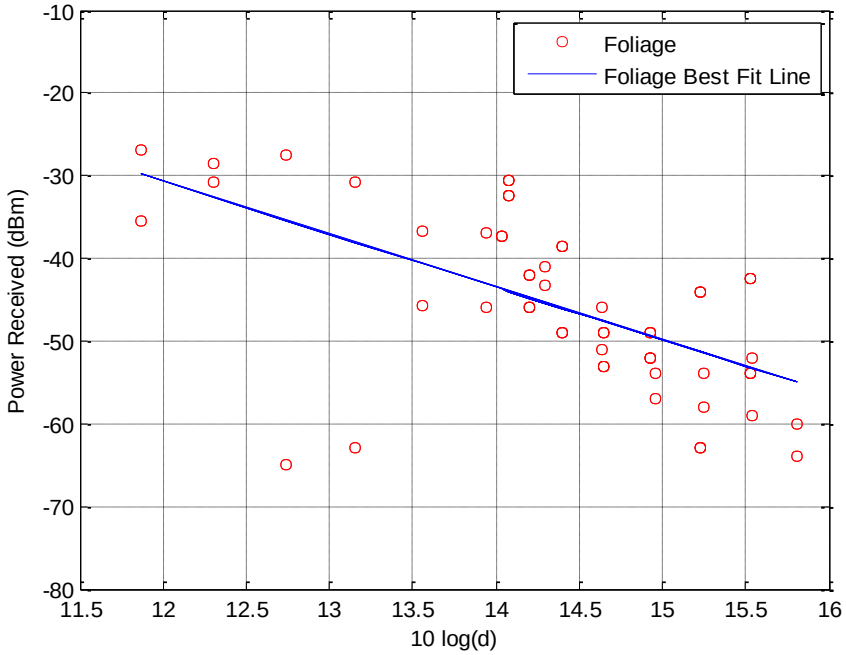

Figure 3.31: Received power measurements in Foliage Environment where TX height is 7.5 meter.

3.3.5. Outdoor-indoor environment and different floors. In this scenario, the TX was placed outdoors while the RX was placed indoors where there is no LOS connections between the TX and RX exist. Although the TX and RX were pointing to each other, they were blocked by the building's concrete wall. Both TX and RX were one meter away from the wall. The wall is 25 cm thick, and is made of concrete. There was no signal received at the RX, meaning that concrete indoor areas were isolated (different clusters), and that the same carrier frequency and modulation schemes could be used for different information in neighboring indoor-outdoor scenarios.

Another test that was conducted included having the TX and RX at two different floors at the main building. No signal was received for any TX-RX antenna orientation. This means that different floors could also be considered isolated, depending on how the transmitter antennae are aligned. Repeaters are considered a good solution to connect outdoor-indoor scenarios and different floors.

3.3.6. Fitting conducted measurements to previous path loss models. Some of the conducted measurements were fitted by path loss models suggested by other researchers to check whether the measurement results fit these models.

5GCM PL CL Office, PL IEEE and 5GCM PL CL Canyon path loss models were used to fit the lab measurements, the rotunda measurements and low urban environment measurements. The 5GCM PL CL Office, PL IEEE and 5GCM PL CL Canyon path loss models are defined in Equation 3.2, Equation 3.3 and Equation 3.4, respectively.

$$PL_{\mathrm{dB}} = 32.4 + 17.38\log_{10}(d) + 20\log_{10}(f_c)\,. \tag{3.2}$$

$$PL_{\mathrm{dB}} = 32.5 + 20\log_{10}(f_c) + 20\log_{10}(d)\,. \tag{3.3}$$

$$PL_{\mathrm{dB}} = 32.4 + 21\log_{10}(d) + 20\log_{10}(f_c). \tag{3.4}$$

Here d is the TX-RX separation distance in meters and f_c is the center frequency of the transmitted signal in GHz. These models are explained in details in [12]. Figure 3.32, Figure 3.33 and Figure 3.34 show the measurement results with the path loss model line.

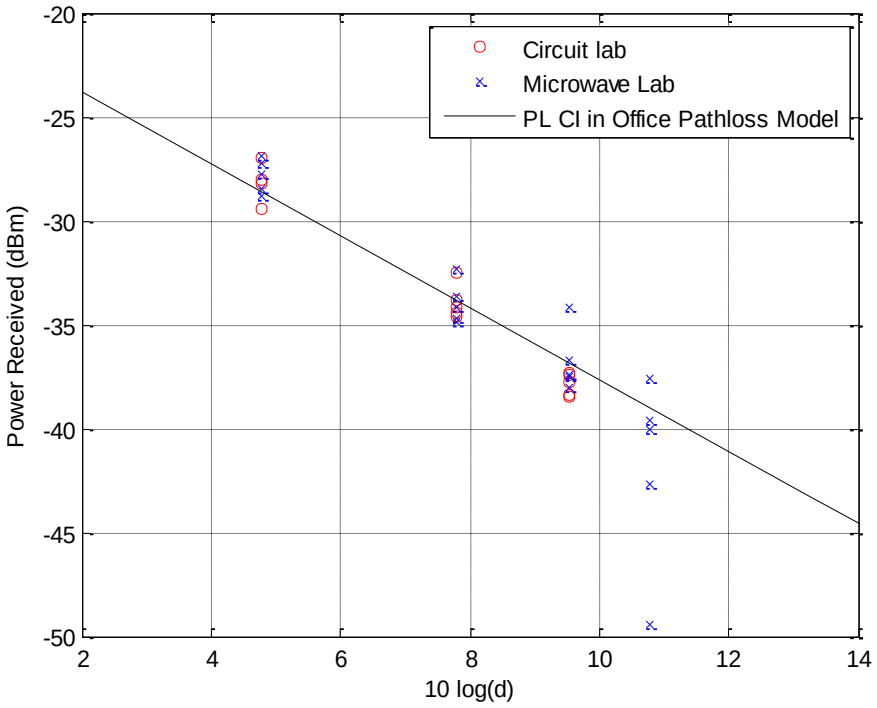

Figure 3.32: Received power measurements in labs and 5GCM Path loss Model for Offices Scenario.

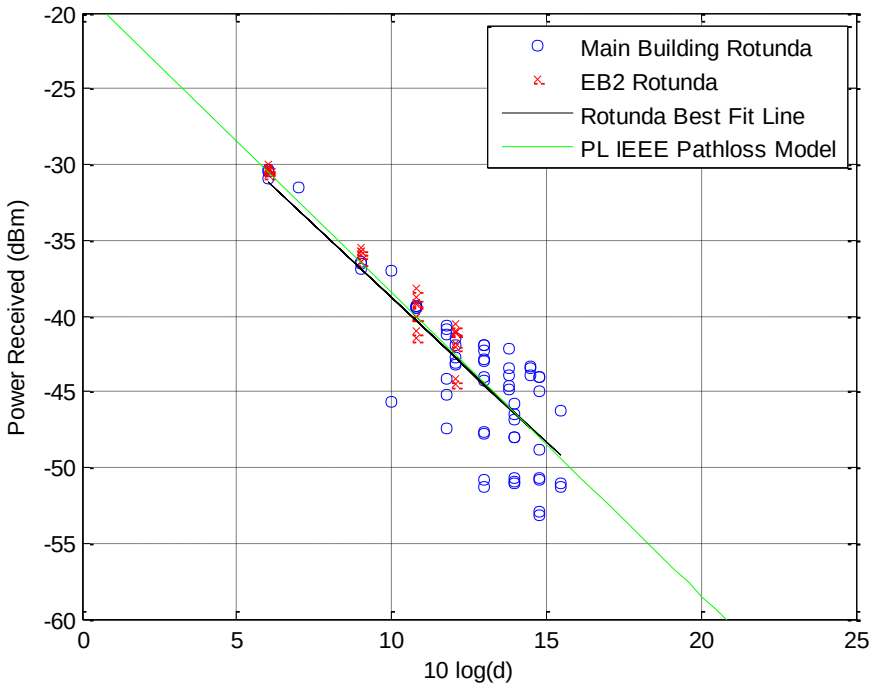

Figure 3.33: Received power measurements in building rotunda and PL IEEE Path loss Model.

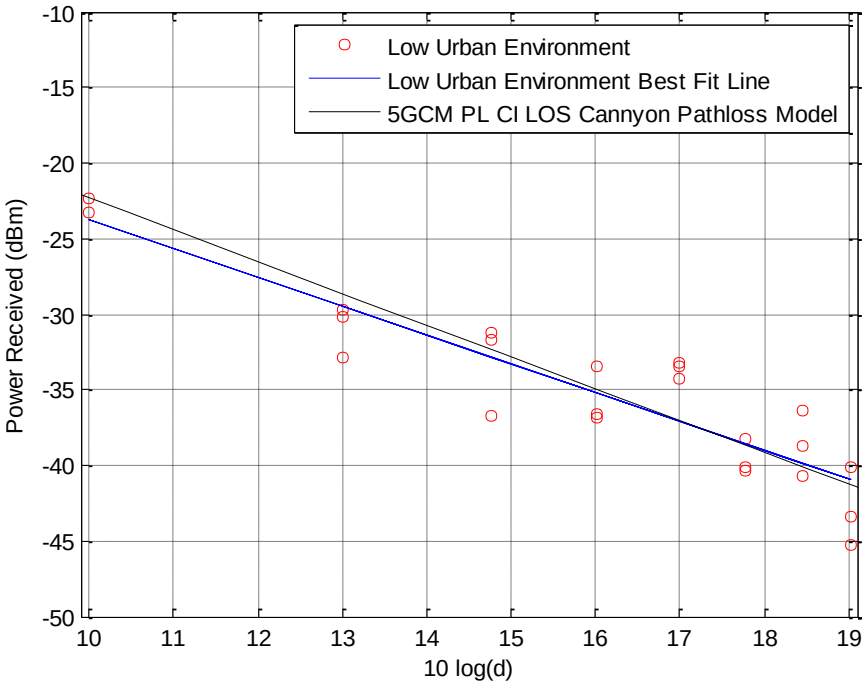

Figure 3.34: Received power measurements in Outdoor Low Urban Scenario and 5GCM Path loss Model.

3.4. Results Analysis and Conclusion

The goal of conducting extensive path loss measurements is to provide a way to predict the path loss for any real scenario, and thus do proper link budget design to get the desired SNR. In general, the path loss can be found from Equation (3.5) given as,

$$PL_{\mathrm{dB}} = PL_{\mathrm{dB}}(d_{ref}) + 10\, n\, log_{10}(d/d_{ref}). \quad (3.5)$$

Here $PL(d_{ref})$ is the path loss at the reference distance d_{ref}, n is the path loss exponent and d is the TX-RX distance. Therefore, by finding out the PLE for each environment, it will be very simple to predict the path loss for any distance. In addition to that, PLE found in a previous scenario in Chapter 3 could be generalized to scenarios with the same aspect. This means that finding PLE for every area in a region is not necessary. Thus, equation (3.5) is a very simple, yet effective, method to predict the path loss for most scenarios. However, path loss could vary from the calculated loss and the variation is measured by the standard deviation of the measurement results.

In summary, utilizing the mm-wave spectrum is the next step for higher data rate communication. Directive antennas and small cell sizes seemed to be the method to employ effectively mm-wave technology. Smaller antennas reduced the costs of base stations, which was an incentive for having higher number of base stations per region. Some challenges stand in the way of this technology; high frequency waves are susceptible to scattering, and cause a great number of multipath components. This, in turn, brings up the need for complicated equalizers at receivers. Relays and repeaters are required to have indoor to outdoor communication due to the high penetration losses present at such high frequencies. Further research must be conducted before applying this technology on bigger scale regions.

It was clear that in general as TX-RX separation distance increased, the path loss increased. Moreover, the PLE of indoor scenarios was in most of the cases below two.

Chapter 4. Penetration and Reflection Measurements

It is important to understand and predict the behavior of signals when they are transmitted through mediums and materials different from air. This is required for designing proper wireless systems and eliminating areas with outages or low SNR. For this reason, both penetration and reflection losses have been measured for different types of building materials that are frequently used in UAE constructions. Penetration loss and reflection measurement in this experiment have been done for different types of glass and building materials using 28 GHz frequency.

4.1. Penetration Measurement for Glass and Aluminum

The reason different glass and aluminum types are used for penetration and reflection measurements is the fact that they are the most commonly used materials to cover any new buildings in The UAE. A sample of the UAE building style is shown below in Figure 4.1.

Figure 4.1: Image of one of the streets in Dubai (UAE) and the common constructions style in Dubai.

The figure shows how towers in the UAE are covered completely or partially with glass or aluminum sheets. The commonly used glass types in UAE are shown in Table 4.1.

Table 4.1: Types of used glass in UAE

Glass type	Glass Description
Clear Glass	Glass that does not contain dyes or coatings
Tinted Glass	Glass that underwent some heat processing to make it stronger and harder to break
Colored Glass	Glass containing color
Laminated Glass	Two pieces of glass that had been attached to each other via glow material, becoming a single piece
Doubled Glass	Two piece of glass, one colored and another clear. This type of glass contains a gap between the two layers while keeping them connected by their edges
Sandblast Glass	Unclear Glass used in bathrooms

Penetration loss measurements were conducted in an outdoor open space to eliminate the effect of the multiple indoor reflections that may occur during the measurement taking process. Both antennas were placed 42 cm away from each other. The objects being tested were placed between both antennas and were fixed on the table using clamps. The measurement setup is shown in Figure 4.2.

Figure 4.2: Image of one of the penetration loss measurement set up.

Table 4.2 shows the penetration loss for different types of glass with 6 mm thickness.

Table 4.2: Penetration loss of different types and colors of single glass

Type of Glass	Penetration Loss (dB)
Clear Glass	2.6
Sandblast Glass	1.4
Bronze Glass	3.3
ST Bronze Glass	8.6
PNA Solar E Plus Bronze Glass	24.5

Lowest penetration losses occurred when sending signals through Sandblast glass; which means that the sand layer added to the clear glass to become sandblast decreased the glass reflection loss. Table 4.2 also shows that different glass colors had different penetration losses. This is because every color of glass panels has a different manufacturing procedure and because of the material added to the glass.

The Other penetration loss experiment had been done by using the same types of glass, but with different thicknesses. Results showed that doubling the glass thickness did not double the penetration loss. For example, 12 mm Sandblast and clear Glass had penetration losses of 2.1 and 4.6 dB, respectively. This comes from the fact that the penetration loss that has been measured is the sum of losses occurring from both reflection and penetration combined. On the other hand, double glass shows impressive results. The penetration loss of three 6mm double glass samples is shown in Table 4.3.

Table 4.3: Penetration loss of different colors of double glass

Type of Glass	Penetration Loss (dB)	Penetration Loss of flipped Glass (dB)
6mm Majestic Bronze with 12 mm air space	24.8	28.8
6mm Majestic Bronze with 16 mm air space	35.2	36
6mm Neutral 70 On Bronze-FT with 12 mm air space	28.6	30.8

The table shows that different double glass colors would imply different penetration losses. It also shows that double glass has very high penetration loss compared to single colored glass. The reason behind this is the fact that double glass has air space separating two pieces of glass, which causes several inner reflections between them, resulting in more losses for the penetrated signal.

Moreover, increasing this air space by 4mm increases the penetration loss by more than 10 dB for the “majestic color” glass panels. In addition, flipping the glass face and making the back face of the double glass (clear piece) facing the TX increases the penetration loss. This is expected, as the second face will be the colored one, which means it will cause more reflections and will accordingly intensify the effects of the air space gap.

Another experiment was conducted for glass measurement, in which two or more sheets of glass were placed on the path of the transmitted signal. It was clear that the

path loss of combined glasses is always less than the sum of path loss of the constituents. This shows that the reflection loss caused when the signal moves from air to glass is much higher than that for transitions between glass and almost any type of glass.

Penetration loss was also found for different types of Aluminum Building covers and other building and non-building materials. The results are shown in Table 4.4.

Table 4.4: Penetration loss of different building materials

Material	Thickness (millimeter)	Penetration Loss (dB)
Stainless Steel Sheet	2	38.8
Aluminum Sheet Silver Mirror Color	4	47.7
Aluminum Sheet Grey Quartz color	4	More than 50.1
Aluminum Sheet Quercus Color	4	49.6
Aluminum Louver	-	17.9
Plastic Sheet	4	zero
Wood Sheet	16	12
Carton Sheet	8	0.3

From Table 4.4, the color of the Aluminum sheet affects the penetration loss. It also shows that when the aluminum contains some gaps, such as in the case of "Aluminum Louver", more signal penetration occurs. Penetration and reflection losses can be used to calculate electrical parameters such as the conductivity and permittivity of the tested material.

4.2. Penetration Measurement for Dusty Glass and Wet Glass and Aluminum

Since measurement was conducted in the UAE, where dusty weather conditions are very common in different times of the year, it only seemed natural to extend the study and incorporate penetration losses for dusty sheets of glass and aluminum. Results show that dust adds losses from 1 to 3 dB for a single sheet. However, it can add up to 5 dB of losses in the case of double glass. In the case of dust, penetration loss increases since dust scatters more signals from the surface of the sheets.

On the other hand, Wet glass and Aluminum have lower penetration loss than dry one. It reaches up to 2 dB for single glass, 3 dB for double glass and 7 dB for 4 mm aluminum sheets. The reason of decreasing the penetration loss is the fact that conductivity of the wet surface is lower than the conductivity of the dry surface, which means its characteristic impedance becomes higher, and therefore its reflection coefficient is lower.

4.3. Reflection Loss Measurement

Reflection loss measurement is important to predict the effect of materials and construction on the signal power in surrounding areas. This work presents reflection measurements for commonly used material in construction in the UAE.

In reflection measurements, both antennas are facing the reflector object. The distance between the antennas and the reflector was 25 cm. The angle of reflection was 45 degrees in respect to the reflector's surface. The reference power is -16.4 dBm. Glass and Aluminum reflection measurement are summarized in Table 4.5.

Table 4.5: Reflection loss of different glass and aluminum types and colors

Material Type	Thickness (mm)	Reflection loss (dB)
Clear Glass	6	3
Sandblast Glass	6	3.2
Sandblast Glass	10	2.3
Bronze Glass	6	4.1
ST Bronze Glass	6	4.5
PNA Solar E Plus Bronze Glass	6	1.1
Double Glass Majestic Bronze with 12 mm air space	6+6	1.3
Double Glass Majestic Bronze with16 mm air space	6+6	1.5
Double Glass Neutral 70 On Bronze-FT with12 mm air space	6+6	1
Stainless Steel Sheet	2	0.8
Aluminum Sheet Silver Mirror Color	4	0.8
Aluminum Sheet Grey Quartz color	4	0.4
Aluminum Sheet Quercus Color	4	0.5
Aluminum Louver	-	2.8

The measurements show that reflection losses for glass, aluminum and steel are very small. Table 4.5 also shows that the reflection loss is smaller for aluminum and steel compared to glass. In addition, the table shows that Sandblast glass yields higher reflection loss than clear glass. The reason lies behind the fact that Sandblast glass' surface is rough and scatters the signal. Other conclusions include the observation that increasing the glass thickness decreases the reflection loss. The higher thicknesses allow less electric field to penetrate through the object edges or by penetrating throw the glass sheet. In addition, the glass color might increase or decrease the reflection loss depending on where the colored side resides. Flipping the double glass side will either decrease or increase the reflection loss, depending on whether the clear glass has lower or higher reflection loss than the colored one used in the sheet. Moreover, double glass has lower reflection loss than single glass since there is a reflected signal component coming from the other face of the glass. This is the reason behind the increases in

reflection losses as the air space in double glass expands. Other tests showed that aluminum sheets also have different reflection losses depending on their colors. In addition, "Aluminum Louver" has higher reflection loss than aluminum sheets since it has some gaps that allow the signal to pass through them.

Table 4.6: Reflection coefficient of different glass and aluminum types and colors

Material Type	Thickness (mm)	Reflection Coefficient
Clear Glass	6	0.707945777
Sandblast Glass	6	0.691830964
Sandblast Glass	10	0.767361481
Bronze Glass	6	0.623734829
ST Bronze Glass	6	0.595662137
PNA Solar E Plus Bronze Glass	6	0.881048864
Double Glass Majestic Bronze with 12 mm air space	6+6	0.860993743
Double Glass Majestic Bronze with16 mm air space	6+6	0.841395133
Double Glass Neutral 70 On Bronze-FT with12 mm air space	6+6	0.749894202
Stainless Steel Sheet	2	0.91201083
Aluminum Sheet Silver Mirror Color	4	0.91201083
Aluminum Sheet Grey Quartz color	4	0.954992576
Aluminum Sheet Quercus Color	4	0.944060867
Aluminum Louver	-	0.724435953

The reflection coefficient of the tested material was calculated using equation (4.1),

$$\Gamma = \sqrt{\frac{P_{\mathrm{r,ref}}}{P_{\mathrm{r,LOS}}}}. \tag{4.1}$$

$P_{r,\mathrm{ref}}$ is the received power reflected from the reflector and $P_{r,\mathrm{LOS}}$ is the reference-received power for a LOS scenario when the TX-RX distance is equal to summation of the distances between TX-reflector and RX-reflector.

Table 4.6 summarizes the reflection coefficient of the tested material. The closer the reflection coefficient to one, the lower the reflection loss (i.e. reflection loss is zero when the reflection coefficient is one).

Based on the measurement results, UAE constructions and building material are highly reflective. This allows outdoor scenarios to have enough reflection and high enough SNR, whereas repeaters are necessary for indoor coverage.

Chapter 5. Small-scale Measurements

As mentioned in Section 1.2 of this report, small-scale measurement is carried out to measure the CIR of the wireless channel. Understanding CIR of wireless channel is important to design the RX circuits and signal processing algorithms needed for recovering the transmitted signal. This report will be concerned with three quantities and will define the CIR of wireless channel at mm-wave, which are PDP, excess delay and RMS delay spread. Small-scale measurement was conducted in AUS's campus in UAE at 24 GHz. No similar measurement was reported in UAE environments and constructions types according to the best of the author's knowledge. The reason behind using 24 GHz instead of 28 GHz is the limitations of the available equipment in AUS labs.

5.1. Small-Scale Measurement Techniques and Set up

The easiest way to find the PDP a is by transmitting wideband signal and using cross correlation between the received signal and the transmitted signal. The other way is by using Sliding Correlation techniques. The measurement techniques used in this work is shown in details in this chapter.

5.1.1. PN sequence generation. As mentioned in Chapter 2, a PN sequence is used to modulate the carrier signal to generate the transmitted signal to measure the PDP of the channel.. The PN sequence is a periodic signal that looks random and has high BW. The PN sequence has very low correlation with any other signal, which made it close to the noise behavior; however, it is easier to generate. Thus, a PN sequence is the most preferred signal to be used in small-scale measurement.

In this work, the PN sequence had been generated using M93M931A Wave Form Generator Module manufactured by Agilent technology. This module operates at 1.25GS/s, 10-bit vertical resolution. Its noise floor is less than -150 dBc/Hz across the channel BW. Its sampling clock is 1.25GS/s with minimum waveform length equal to 128 samples and waveform granularity of 8 samples. First step of PN sequence is by generating the PN sequence using MATLAB. The MATLAB code used is shown in Appendix C. The used PN sequence has the polynomial power Fs= {9, 4}, and thus its period length is 511 chips. A 31chep of the generated signal can be shown in Figure 5.1.

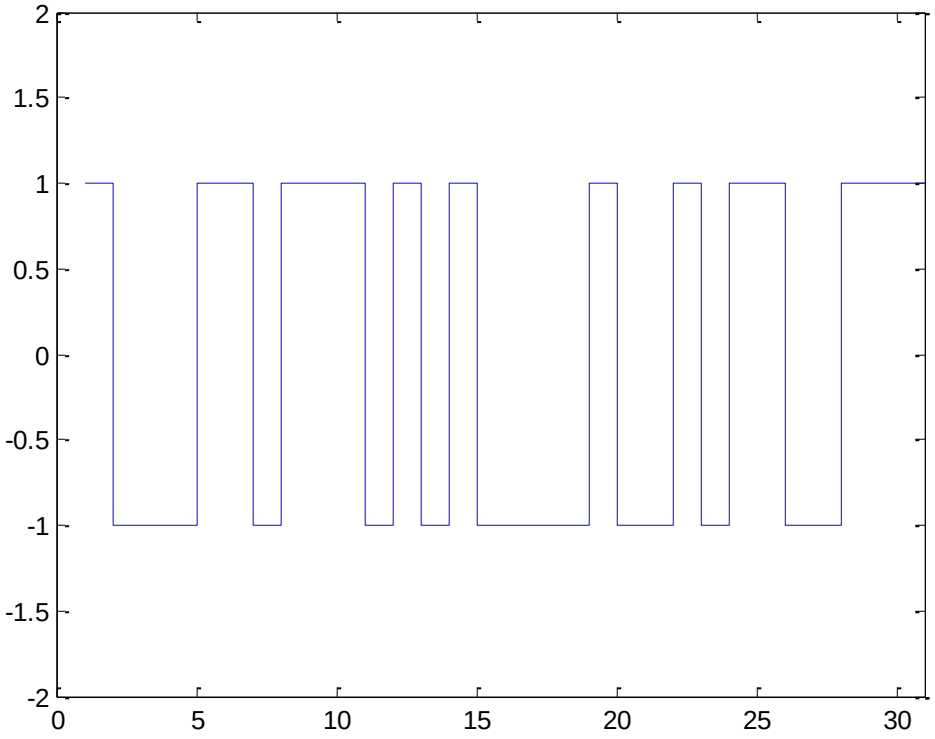

Figure 5.1: Pseudo-random noise derived from an m-sequence.

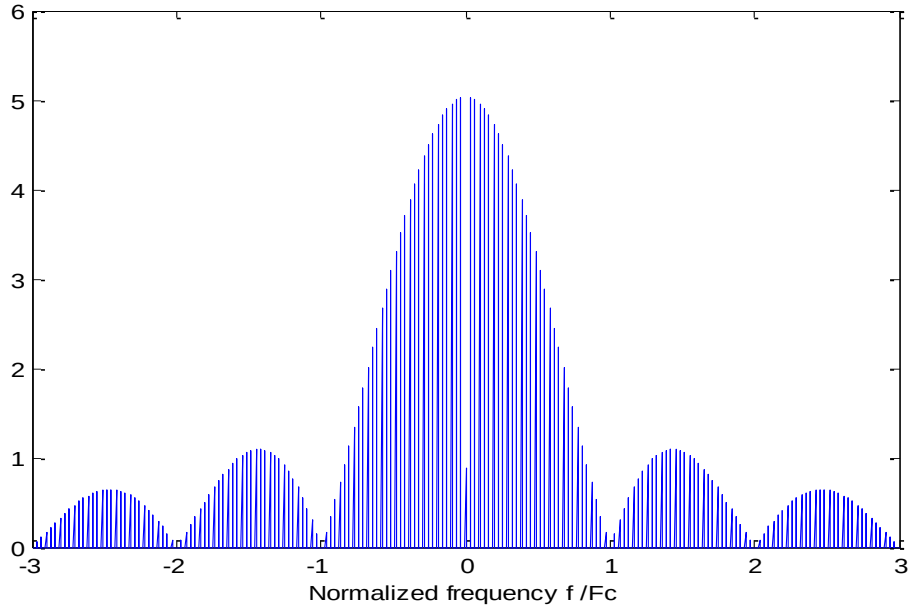

Figure 5.2: The frequency spectrum of a PN is characterized by a train of Dirac delta functions under a sinc (f/fc) envelope.

The frequency domain of the generated PN sequence signal is shown in Figure 5.2. The autocorrelation of the PN sequence is shown in Figure 5.3.

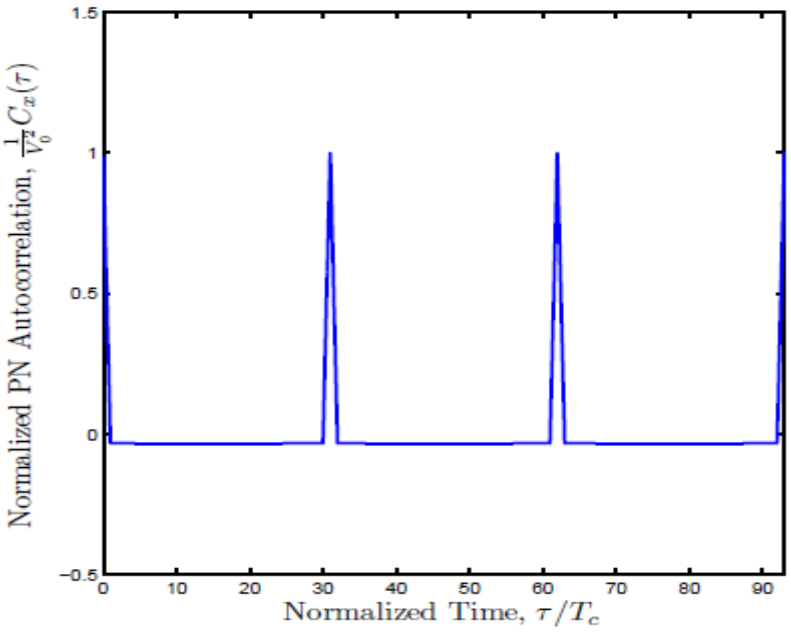

Figure 5.3: The autocorrelation of a PN is characterized by a train of sharp triangular peaks, each with a base width of 2Tc [54].

After generating the signal in MATLAB, interface between the MATLAB and the M93M931A Wave Form Generator Module have been done. The time domain output of the generator is shown in Figure 5.4. Its chip rate is 250 MHz, thus first null in the BW is at 250 MHz and second null is at 500 MHz The temporal resolution is 1/fc = 4 ns. The max multipath delay is one period time length, and it is equal to the number of chips per period multiplied to the chip time length, which is equal to $511 \times 4\ \text{ns} = 1.226\ \mu s$. The maximum path delay that corresponds to $1.226\ \mu s$ is 367.9 meters. The peak-to-peak voltage was equal 166 mV, and the calculated output power is 6.9 dBm.

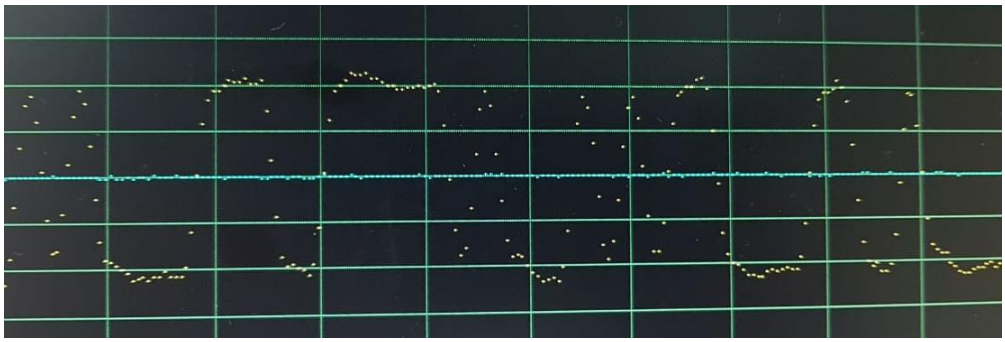

Figure 5.4: Generated PN sequence found by the M9210A.

5.1.2 Measurement setup. The transmitter and receiver setups are shown in Figure 5.5. The details of the used equipment are shown in Table 5.1.

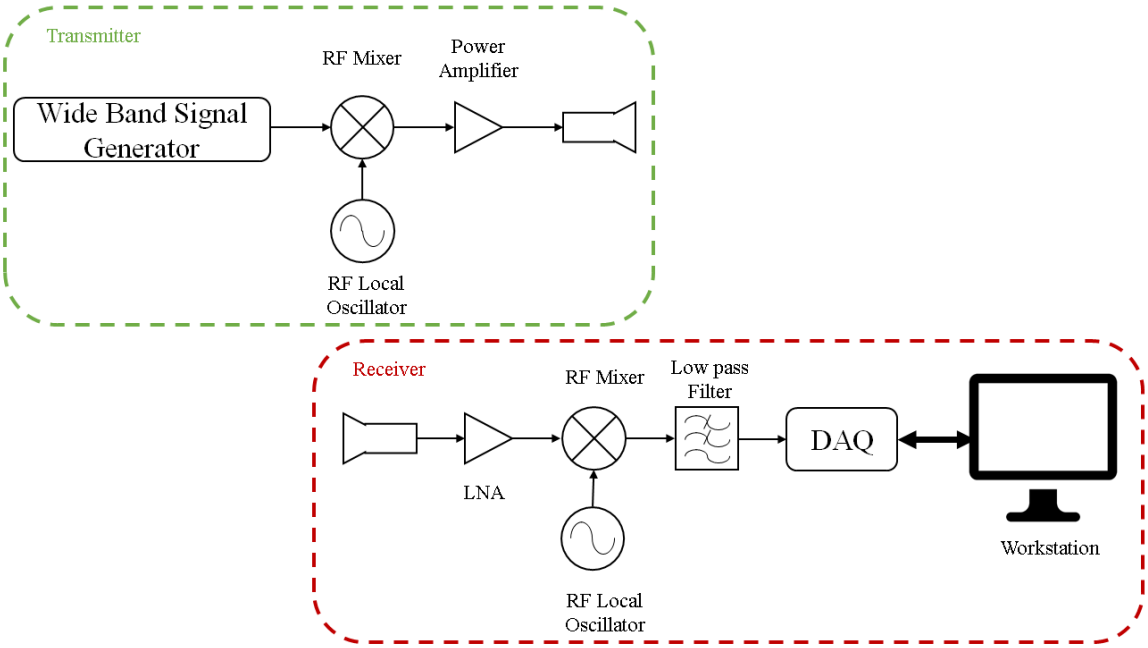

Figure 5.5: Block diagram of the measurements system.

The transmitted power is equal to 12 dBm. The transmitted frequency is 24 GHz since the only available oscillator convert down the frequency by 22.5 GHz, which is not enough to convert 28 GHz signal into the range of the high bandwidth oscillator (2 GHz).

Table 5.1: The details of the components used for small-scale measurement's TX and RX.

Component	Manufacturer and Model Number	Details
Amplifier	HD Communications Corp-HD30172	24 dB gain with 13dBm saturated power
Mixer	Marki Microwave-M2-0240	12 dB convergent loss
Oscillator	Cernexwave-42S35FOO	22.5 GHz with 10 dBm output power
Antenna	Cernexwave –Waveguide Standard Gain Horn Antenna	30° beam width with 15 dB gain at Ka Band

Thus, another down conversion stage is needed which requires another amplifier that is not available in the lab. Moreover, the passband signal is 1 GHz, which

is affected by the available mixer non-linearity at 28 GHz. Thus, the received signal is subjected to some distortion. The received signal is captured by the antenna and amplified by a cascaded two 24 dB amplifiers, and then mixed down to 1.5 GHz frequency. Then, the signal is saved and down converted into baseband signal using MATLAB. To get the PDP, a cross correlation between the down converted signal and the original PN signal is found. The cross correlation graph is the channel impulse response of the environment.

5.2. Measurement Scenarios

Both indoor and outdoor scenarios were used to conduct small-scale measurement. In each scenario, RMS delay spread, received power, number of multipath component and PDP were found. Average excess delay ($\bar{\tau}$) and RMS delay spread (σ_τ) are calculated as shown in (5.1) and (5.2) respectively:

$$\bar{\tau} = \frac{\sum \tau p(\tau)}{\sum p(\tau)} \tag{5.1}$$

$$\sigma_\tau = \sqrt{\tau^2 - \bar{\tau}^2} \tag{5.2}$$

where $p(\tau)$ and τ are the power in watt and its delay component.

Each measurement's result is found after taking the average of four-measurement reading at the same scenario. The minimum power threshold that could be detected as for a multipath component was selected to be10 dB below the highest multipath power. The reason behind this threshold is the fact that below this value, the multipath component is neglected and very close to noise level caused by the receiver amplifiers. Furthermore, the minimum time distance between two neighboring peaks was chosen to be 4 ns.

5.2.1. Microwave lab measurement. The microwave lab image is shown in Figure 3.2. Both TX and RX were placed in the middle of the lab. The TX-RX distance is 10 meter. The received signal is captured every 15° RX's antenna rotation in the counterclockwise direction. Measurement results are summarized in Table 5.2. Figure 5.6 shows the top view diagram of the measurement setup. Figure 5.7 the PDP for 0°, 30°, 90° and 180° RX antenna angles, while and Figure 5.8 shows received power polar plot. Table 5.2 shows that number of multipath is one when the antenna is from $-60°$ to 60° around the LOS.

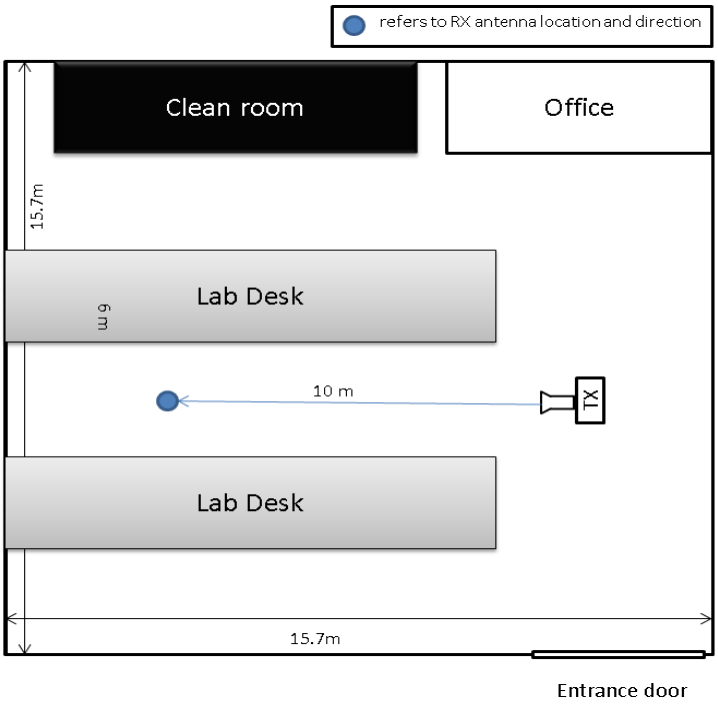

Figure 5.6: Microwave Lab top view measurement setup diagram.

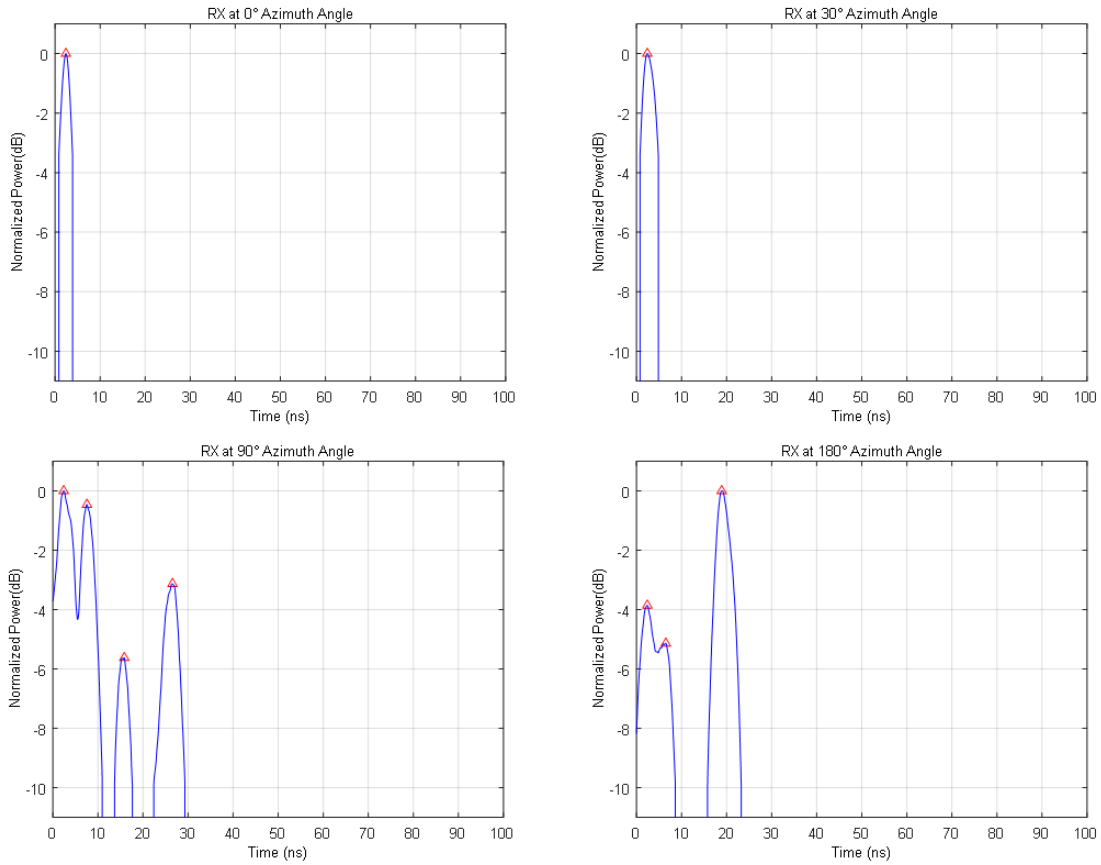

Figure 5.7: PDP of microwave lab measurements for 0°, 30°, 90° and 180° RX antenna angle.

It is also shows that the highest number of paths occurs when the antenna is from 120° to 270° around the opposite side of the LOS. For a single path, excess delay varies from 2.25 ns to 2.96 ns, and RMS delay varies from 1.11 ns to 1.49 ns.

Table 5.2: Microwave lab measurement results

Angle in degrees	Total received power (dBm)	10 dB threshold paths	Excess delay (ns)	RMS delay spread (ns)
0	-7.1297	1	2.42	1.15
15	-9.6252	1	2.72	1.36
30	-13.0283	1	2.96	1.49
45	-14.5602	1	2.29	1.33
60	-14.3629	2	2.73	1.73
75	-15.1168	1	2.34	1.28
90	-14.1802	2	3.23	1.88
105	-14.6075	2	3.15	4.07
120	-15.1941	4	10.3	8.99
135	-16.4314	6	18.9	11.95
150	-15.0491	3	17.6	10.6
165	-16.9087	4	14.4	10.1
180	-16.5504	3	13.7	7.67
195	-15.4408	4	12.3	8.26
210	-15.8429	1	2.44	1.21
225	-16.3188	2	3.80	4.83
240	-14.7318	8	16.1	12.1
255	-13.7805	5	12.5	7.35
270	-14.0648	5	16.8	13.9
285	-13.6107	2	5.43	4.92
300	-16.0804	3	5.12	3.92
315	-13.4706	1	2.83	1.43
330	-13.0656	1	2.25	1.11
345	-6.4069	1	2.49	1.19

The difference in excess delay and RMS delay spread for single paths shows that the width of the path is different, which means that there are other paths combined with the single path and it is less than 4 ns away from it (below the resolution of our measurement).

In addition, both RMS delay spread and excess delay increase when number of paths increases. The highest RMS delay spread occurs at angle 135°, and is equal to 11.95 ns. This value is very small since microwave lab is a very small indoor environment.

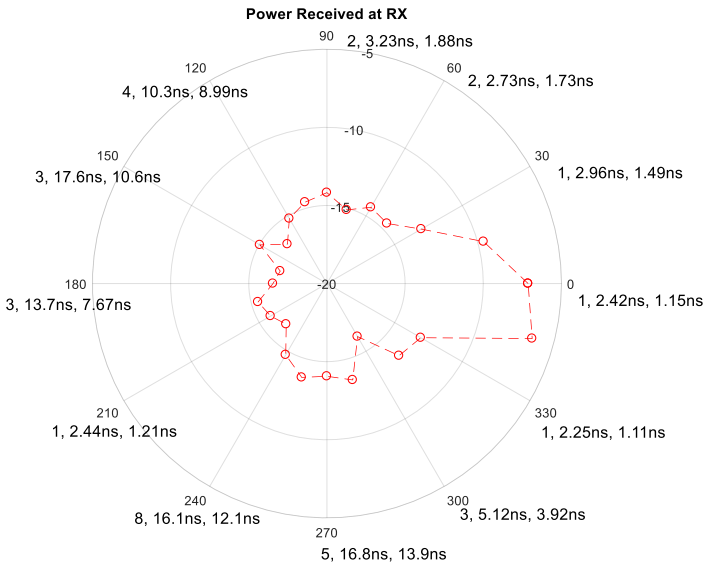

Figure 5.8: AOA polar plot received power in dBm at the RX on microwave lab. The plot shows number of resolvable multipath components, the excess delay, and RMS delay spread for every 30° RX azimuth angles.

5.2.2. Power lab measurement. The power lab image is shown in Figure 5.9. Measurements were conducted for TX-RX distance to be 7 and 14 meters. For 14 meters, TX-RX separation distance, the RX was covered by metallic equipment station and no LOS exists. Top view of measurement setup is shown in Figure 5.10. Measurement results are summarized in Table 5.3 and Table 5.4. Figure 5.11 shows the PDP for 0°, 30°, 90° and 180° RX antenna angles, whereas Figure 5.12 shows the received power polar plot for the power lab with 7 meter TX-RX distance separation. Figure 5.13 shows the PDP for 0°, 30°, 90° and 180° RX antenna angles, while Figure 5.14 shows power polar plot for the power lab with 14 meter TX-RX distance separation.

The results for the different angles are summarized in Tables 5.3 and 5.4. It is noticed from Table 5.4 that the highest excess delay and RMS delay are 38.5 ns and 21.9 ns respectively. The number of multipath components varies from 5 to 16 paths, which is much higher than microwave lab case since the lab is larger and crowded with bigger metallic components. The highest numbers of paths occur when the RX antenna's angle is from 30° to165°, which is the case when the antenna faces the open area in its left side.

Figure 5.9: Power lab measurement scenario.

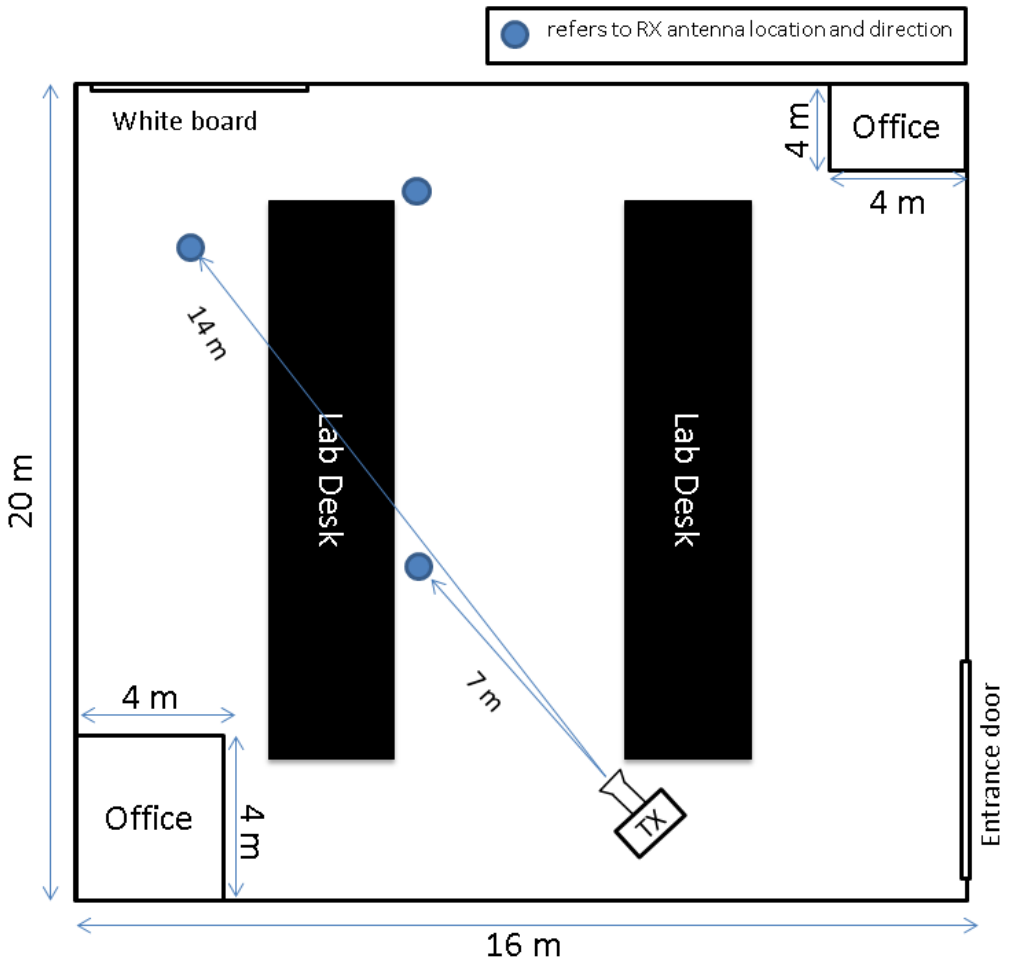

Figure 5.10: Microwave Lab top view measurement setup diagram.

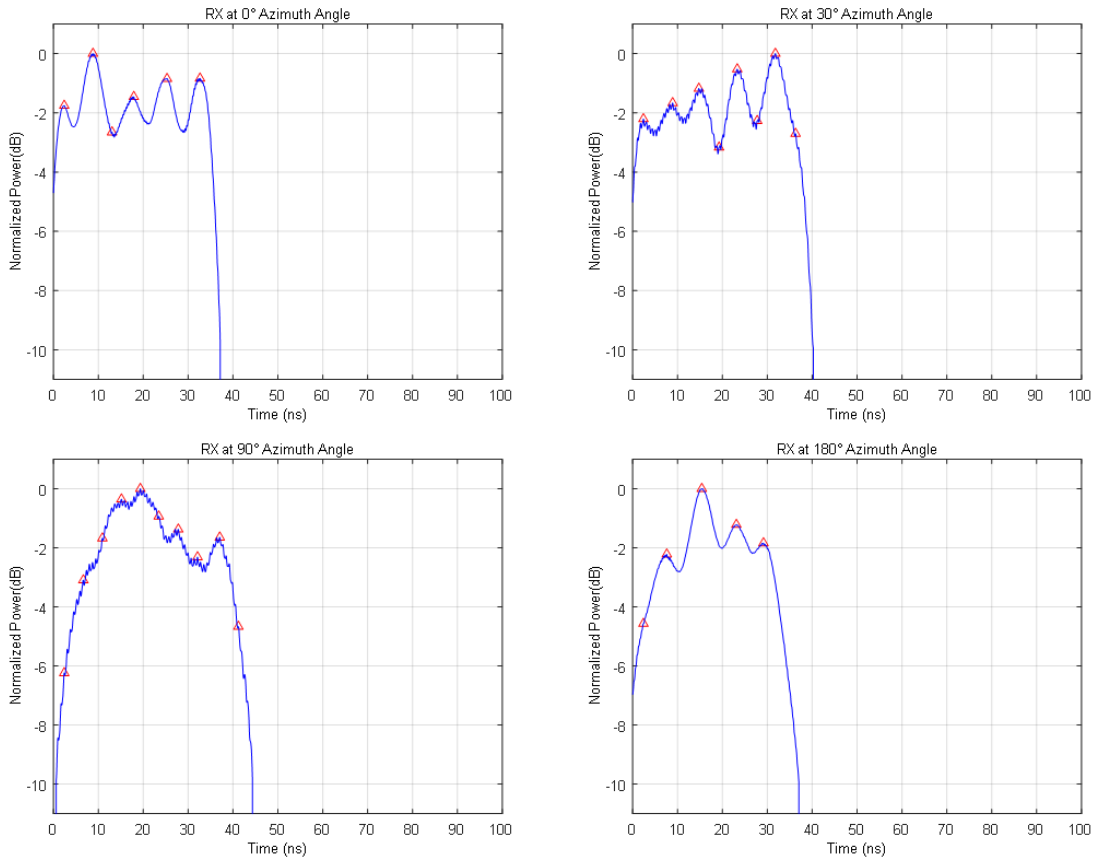

Figure 5.11: PDP of power lab 7m TX-RX distance measurements for 0°, 30°, 90° and 180° RX antenna angle.

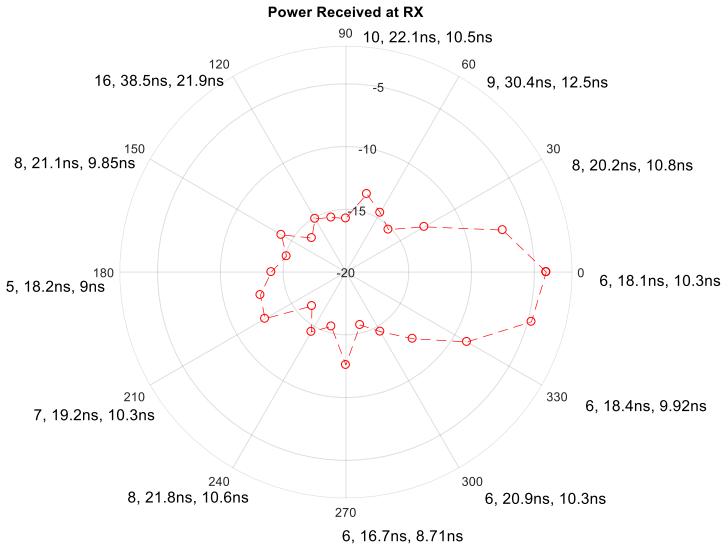

Figure 5.12: AOA polar plot received power in dBm at the RX on power lab for 7 m TX-RX distance case. The plot shows number of resolvable multipath components, the excess delay, and RMS delay spread for every 30° RX azimuth angles.

Table 5.3: Power lab measurement results for 7-meter TX-RX separation distance.

Angle in degrees	Total received power (dBm)	10 dB threshold paths	Excess delay (ns)	RMS delay spread (ns)
0	-4.0526	6	18.1	10.3
15	-7.0794	5	15.9	9.02
30	-12.7948	8	20.2	10.8
45	-15.2153	8	24.3	10.7
60	-14.5391	9	30.4	12.5
75	-13.5579	9	27.6	10.2
90	-15.7239	10	22.1	10.5
105	-15.4972	11	25.9	10.5
120	-15.0965	16	38.5	21.9
135	-16.1648	9	23.2	15.0
150	-14.0648	8	21.1	9.85
165	-15.1126	14	32.4	26.3
180	-14.0615	5	18.2	9.00
195	-12.9558	7	17.6	9.62
210	-12.5655	7	19.2	10.3
225	-16.1823	9	22.8	9.85
240	-14.5052	8	21.8	10.6
255	-15.5199	4	12.2	7.19
270	-12.6043	6	16.7	8.71
285	-15.6385	8	18.2	9.46
300	-14.5240	6	20.9	10.3
315	-12.4919	5	17.2	9.46
330	-8.8754	6	18.4	9.92
345	-4.7087	6	11.1	6.83

Table 5.4 shows that increasing TX-RX distance and not having a LOS between TX and RX will increase the number of paths, and therefore the RMS delay spread. The maximum excess delay and RMS delay spread for the power lab are 109 ns and 247 ns, respectively. The highest number of paths occurs when RX is in the range from 150° to225°, which is when the antenna faces the whiteboard and open area in its right side.

It is also can be noticed that the highest multipath component power is always not the first one for 14 m TX-RX distance case. This occurs because of the total TX-RX sight blockage in this scenario.

Finally, the received signal power in power lab is from -11.8 dBm to -16.7 dBm, which highlighted the fact that power lab is an indoor environment that reflect the signal and scatter it everywhere which keeps the signal level almost constant for most of the points inside the lab and for any RX antenna angle.

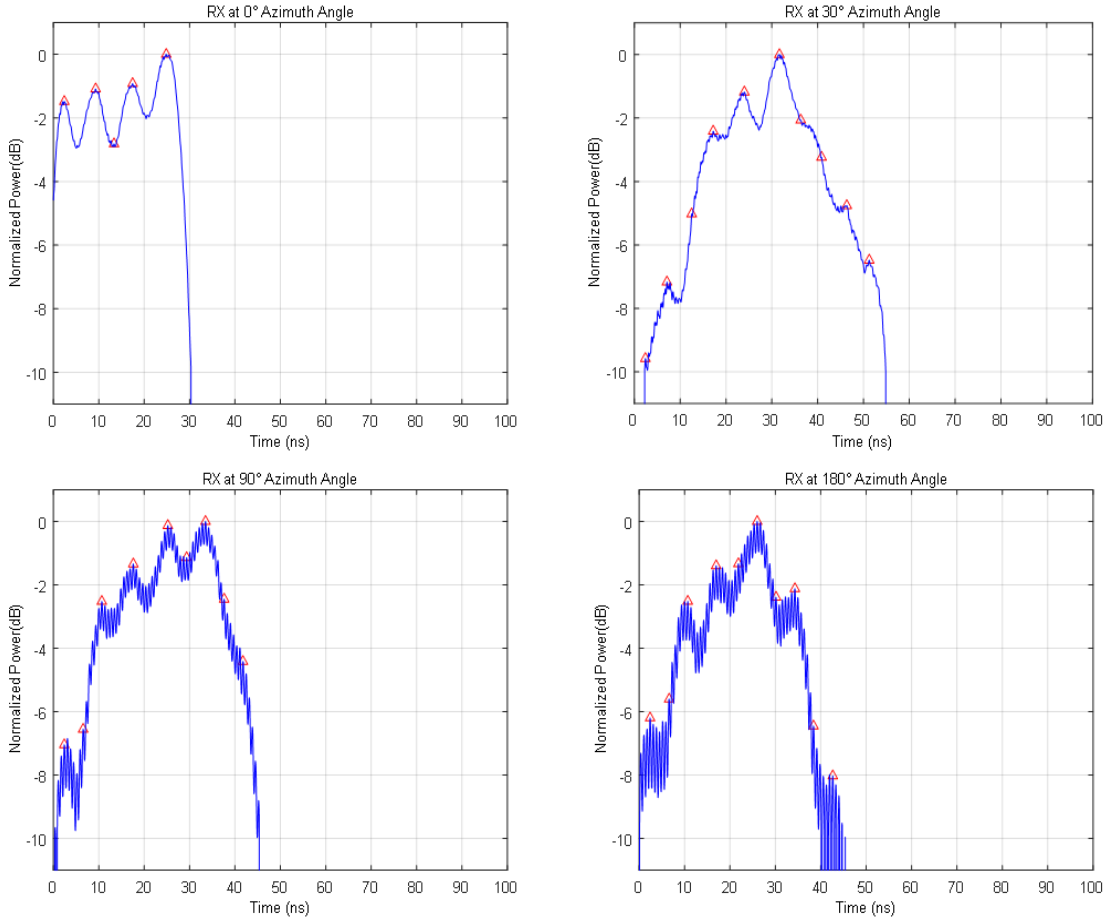

Figure 5.13: PDP of power lab 14m TX-RX distance measurements for 0°, 30°, 90° and 180° RX antenna angle.

5.2.3. Corridor measurement. Small-scale measurements were conducted in the corridor shown in Figure 5.15. Figure 5.16 shows the top view measurement set up diagram.

The corridor is 27.4 meters long, 2.67 meters high and 4 meters in width. Measurement was conducted for 10 meters and 20 meters TX-RX separation distance. The TX was stationary at the middle of the end of the corridor, where RX was moving for every TX-RX distance.

Measurement results are summarized in Tables 5.5 and 5.6. The threshold for path detection was set to be 20 dB less than the highest multipath component, and strong path threshold was 10 dB less than the highest multipath component.

The number of paths for 10 meters TX-RX separation varied from 4 ns to 14 ns. The calculated excess delays and RMS delay spread are 144 ns and 87.2 ns, respectively.

Table 5.4: Power lab measurement results for 14-meter TX-RX separation distance.

Angle in degrees	Total received power (dBm)	10 dB threshold paths	Excess delay (ns)	RMS delay spread (ns)
0	-11.8814	5	15.4	8.37
15	-14.2617	7	20.2	10.3
30	-15.3998	10	29.2	11.4
45	-14.7554	7	22.1	10.4
60	-13.2782	19	42.8	18.7
75	-15.8746	13	30.1	14.5
90	-15.2957	9	24.9	10.2
105	-16.7654	20	35.2	19.9
120	-15.4343	10	23.5	12.0
135	-16.6284	8	18.7	9.5
150	-15.7479	20	32.6	29.6
165	-15.6657	30	71.6	69.8
180	-15.0712	17	27.1	16.9
195	-15.9036	7	30.1	11.4
210	-15.6637	52	85.0	169
225	-16.1034	46	109	247
240	-15.7868	16	30.3	15.4
255	-14.1893	9	20.1	10.5
270	-14.6827	17	32.5	28.5
285	-16.0447	12	29.1	11.6
300	-16.4256	21	32.5	30.9
315	-15.4422	7	17.6	9.19
330	-13.9048	6	18.9	9.14
345	-11.8455	5	16.1	8.37

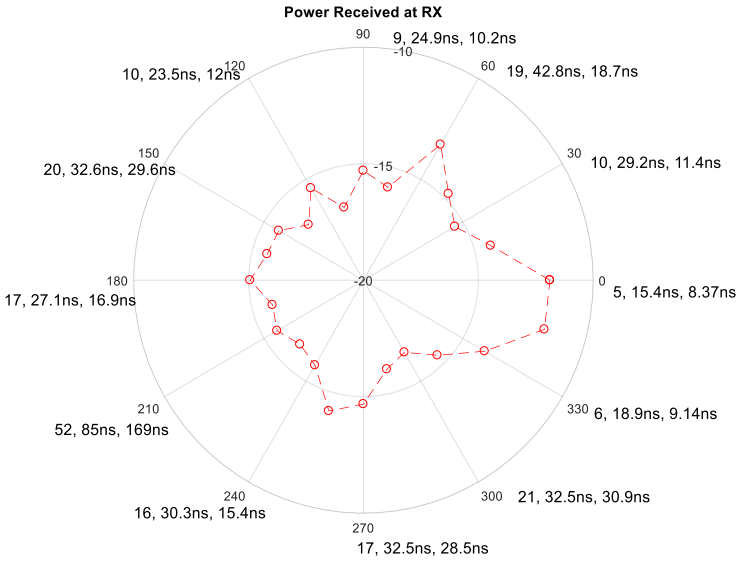

Figure 5.14: AOA polar plot received power in dBm at the RX on power lab for 14 m TX-RX distance case. The plot shows number of resolvable multipath components, the excess delay, and RMS delay spread for every 30° RX azimuth angles.

Figure 5.15: Corridor measurement scenario

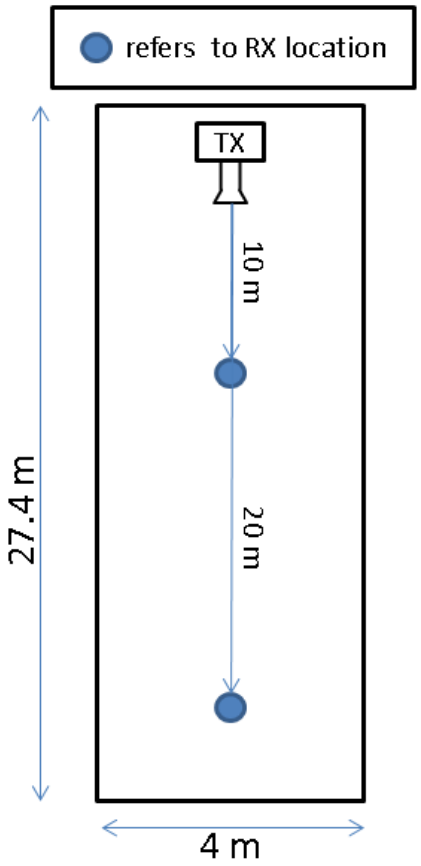

Figure 5.16: The corridor top view measurement setup diagram.

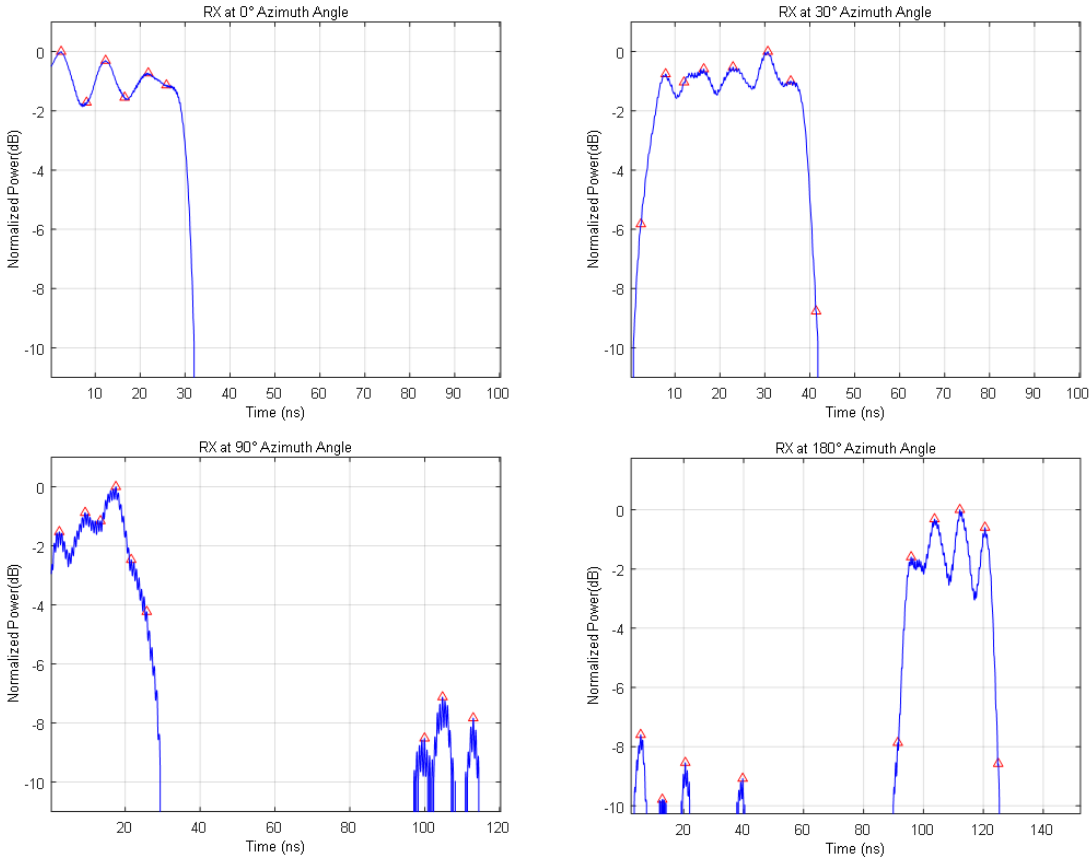

Figure 5.17: PDP of corridor 10 m TX-RX distance measurements for 0°, 30°, 90° and 180° RX antenna angle.

The time difference between paths is higher in corridor rather than lab case since corridor causes many reflections to the signal before it reaches the RX antenna, while labs will attenuate the signal power if it had the same number of reflections. The received power is between -5 dBm and -15.5 dBm except for the case when RX antenna is at 195° and 210° (facing the door of a class hall). Figure 5.17 and Figure 5.18 show, respectively, the PDP for 0°, 30°, 90° and 180° RX antenna angles and the received power polar plot for corridor for a 10 meters TX-RX separation. Figure 5.19 and Figure 5.20 show, respectively, the PDP for 0°, 30°, 90° and 180° RX antenna angles and received power polar plot for corridor for a 20 meters TX-RX separation. For 20 meters TX-RX distance, the average number of paths increased because of the increase in the TX-RX distance. The number of paths varied from 4 to 19 paths. Excess delay and RMS delay values maximum values are 34.5 ns and 127 ns respectively, which are less than 10 meters TX-RX distance case; the reason behind this is the fact that higher distance is associated with higher path loss

Table 5.5: Corridor measurement results for 10-meter TX-RX separation distance.

Angle in degrees	Total received power (dBm)	10 dB threshold paths	Excess delay (ns)	RMS delay spread (ns)
0	-5.3205	6	14.9	8.93
15	-7.7490	5	14.8	7.84
30	-13.1617	8	21.8	10.5
45	-14.5778	6	17.5	9.30
60	-14.9492	8	20.6	9.68
75	-15.0462	11	24.4	10.2
90	-14.8980	9	21.2	26.7
105	-15.4088	4	7.85	5.25
120	-15.2009	14	37.8	33.7
135	-15.4590	13	43.4	39.0
150	-14.5996	7	72.3	13.0
165	-14.5985	9	53.4	12.0
180	-14.0679	10	103	22.7
195	-20.0187	13	144	87.2
210	-21.3226	6	17.6	8.68
225	-13.0778	5	17.9	9.70
240	-15.5020	7	22.1	10.8
255	-15.2599	10	21.6	9.17
270	-15.1320	9	23.3	10.3
285	-15.5557	8	23.5	10.2
300	-15.0782	9	21.9	8.29
315	-12.5546	8	19.9	10.4
330	-11.5758	7	17.8	9.90
345	-5.3546	5	16.0	9.43

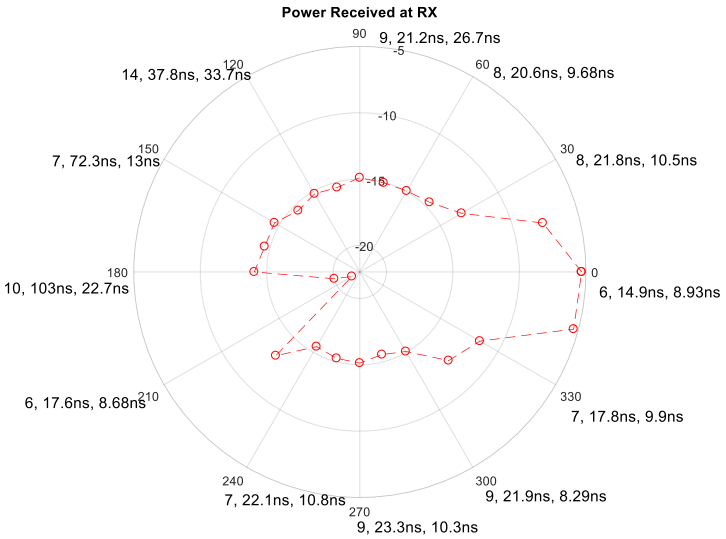

Figure 5.18: AOA polar plot received power in dBm at the RX on corridor for 10 m TX-RX distance case. The plot shows number of resolvable multipath components, the excess delay, and RMS delay spread for every 30° RX azimuth angles.

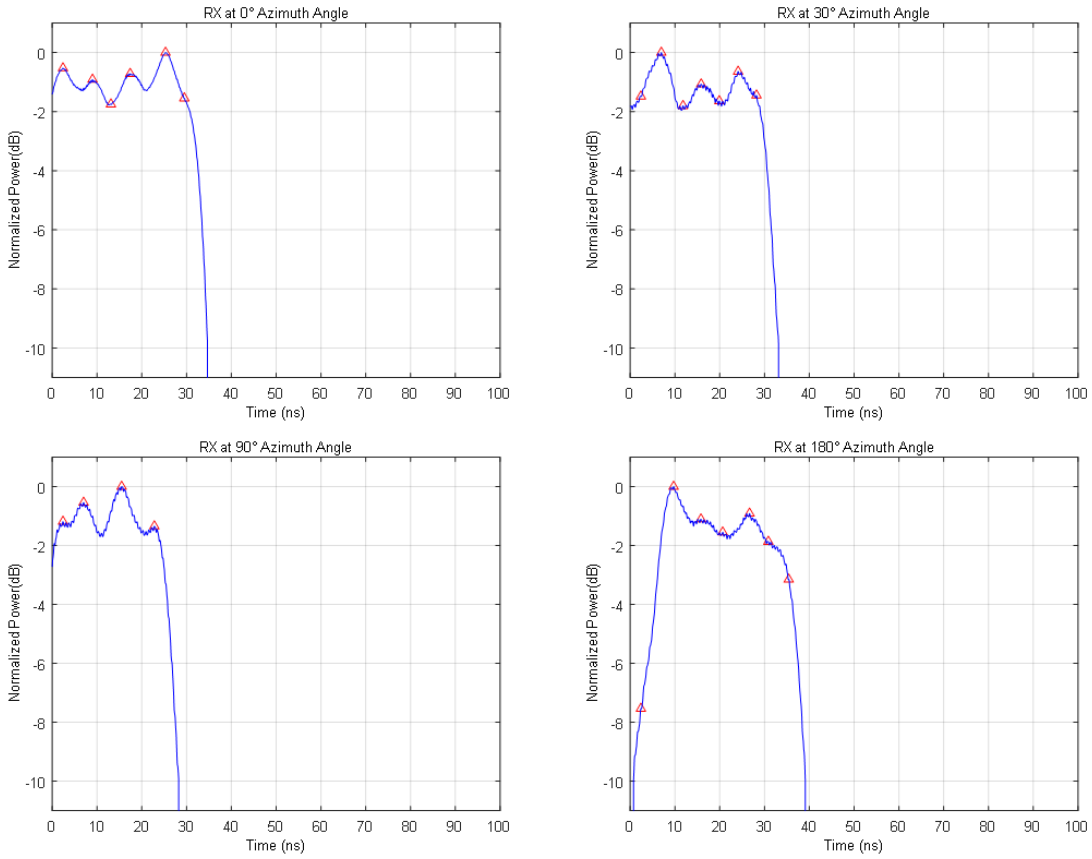

Figure 5.19: PDP of corridor 20 m TX-RX distance measurements for 0°, 30°, 90° and 180° RX antenna angle.

Thus, paths reaching RX antenna only had single or double reflections. In addition, the power received is between -14 dBm and -16 dBm in most of the angles. Higher number of paths occurs among the angle between 195° and 300°, which are the cases when the antenna faces wide exit in this corridor.

5.2.4. Engineering building 1 rotunda measurement. Measurements were conducted in EB rotunda. The building picture is in Figure 3.9. Both TX and RX were placed in the corner of the building. The TX-RX distance was 18 meter. Measurement results are summarized in Table 5.7.

The number of paths for Engineering Building rotunda varied from 4 to 17. The maximum excess and RMS delay spread is 64.7 ns and 155 ns, respectively. The received power is between -9.5 dBm and -17.3 dBm. Figure 5.21 and Figure 5.22 show, respectively, the PDP for 0°, 30°, 90° and 180° RX antenna angles and the received power polar plot for engineering building scenario.

Table 5.6: Corridor measurement results for 20 meters TX-RX separation distance.

Angle in degrees	Total received power (dBm)	10 dB threshold paths	Excess delay (ns)	RMS delay spread (ns)
0	-9.3036	6	16.4	9.51
15	-9.1612	7	18.8	10.4
30	-12.5060	7	15.3	8.98
45	-15.0346	9	20.6	9.39
60	-15.0827	8	20.2	9.13
75	-14.8881	8	21.7	8.27
90	-15.1087	10	23.8	68.3
105	-14.9598	13	34.7	14.7
120	-15.0515	9	27.0	11.6
135	-14.8241	8	20.3	10.2
150	-14.6020	6	18.6	9.62
165	-13.5362	7	18.7	9.95
180	-14.3425	7	19.8	9.44
195	-19.9423	8	20.2	10.2
210	-14.9862	14	34.4	16.7
225	-15.1107	9	28.8	33.7
240	-14.9540	12	29.5	52.4
255	-15.6604	13	34.5	61.4
270	-15.4973	19	24.8	48.5
285	-15.5383	8	17.1	8.86
300	-14.8638	15	33.4	127
315	-14.5740	4	12.9	6.79
330	-12.1948	5	19.0	9.41
345	-8.2879	5	17.3	9.67

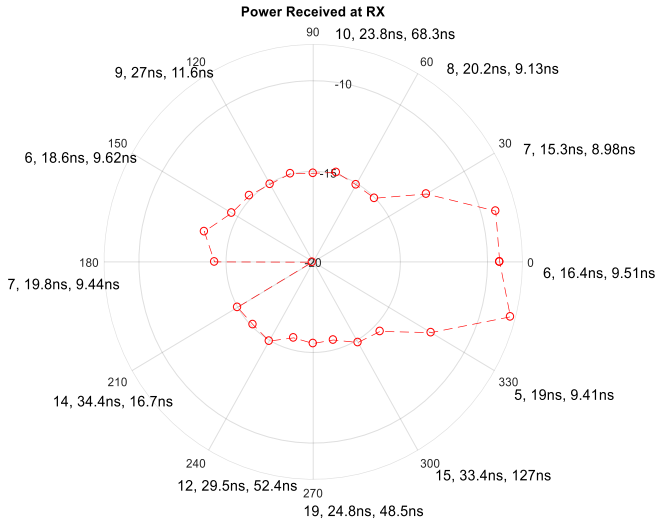

Figure 5.20: AOA polar plot received power in dBm at the RX on corridor for 20 m TX-RX distance case. The plot shows number of resolvable multipath components, the excess delay, and RMS delay spread for every 30° RX azimuth angles.

Table 5.7: EB2 rotunda measurement results for 18 meters TX-RX separation distance.

Angle in degrees	Total received power (dBm)	10 dB threshold paths	Excess delay (ns)	RMS delay spread (ns)
0	-9.5992	4	12.4	7.46
15	-9.9768	6	19.3	10.9
30	-13.5395	7	20.3	10.9
45	-15.0911	9	19.9	9.96
60	-15.7435	10	26.8	12.6
75	-15.0075	8	31.3	10.3
90	-13.9280	7	18.7	10.6
105	-11.5283	6	16.5	9.57
120	-12.0236	7	18.6	10.7
135	-15.4890	7	20.4	10.7
150	-16.1318	12	27.3	12.0
165	-15.5600	10	27.6	11.2
180	-16.1744	13	26.6	11.6
195	-17.1249	8	21.8	9.75
210	-17.3522	6	18.9	9.43
225	-15.4159	8	30.7	11.6
240	-16.1409	5	18.3	10.4
255	-15.3788	5	17.4	9.88
270	-15.7649	14	36.9	25.1
285	-15.4442	10	37.8	155
300	-16.0596	17	64.7	34.6
315	-15.9334	8	21.9	10.3
330	-15.6241	7	18.1	14.7
345	-13.4930	7	20.4	11.0

Another measurement was conducted in the same scenario, but when it was crowded with people. The measurement results are summarized in Table 5.8. For crowded rotunda case, excess delay, RMS delay and received power have decreased. The reason behind that is the fact that multipath components can reach the RX antenna from limited directions due to the presence of people, whom will block the signal paths. The received power varied from -13.28 dBm to -35.4 dBm. The excess delay and RMS delay spread maximum values are 46.2 ns and 37.7 ns, respectively. Figure 5.23 and Figure 5.24 show, respectively, the PDP for 0°, 30°, 90° and 180° RX antenna angles and the received power polar plot for crowded engineering building scenario.

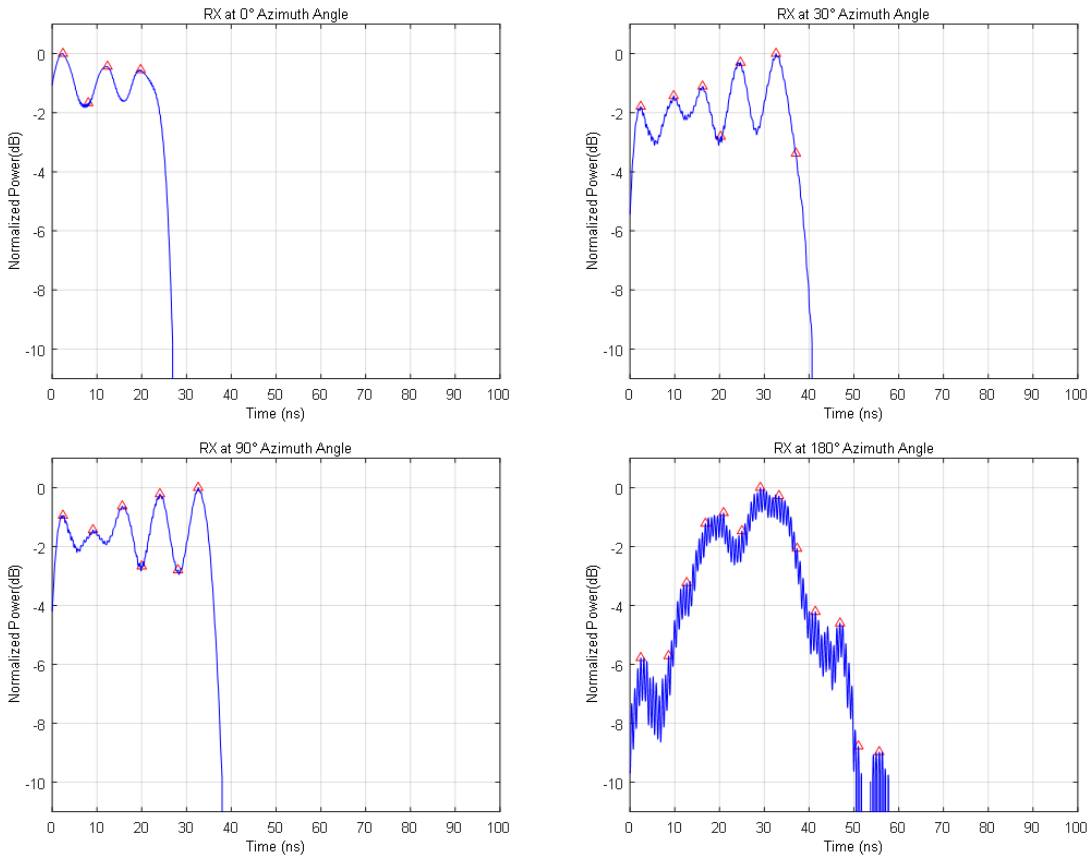

Figure 5.21: PDP of engineering building measurements for 0°, 30°, 90° and 180° RX antenna angle.

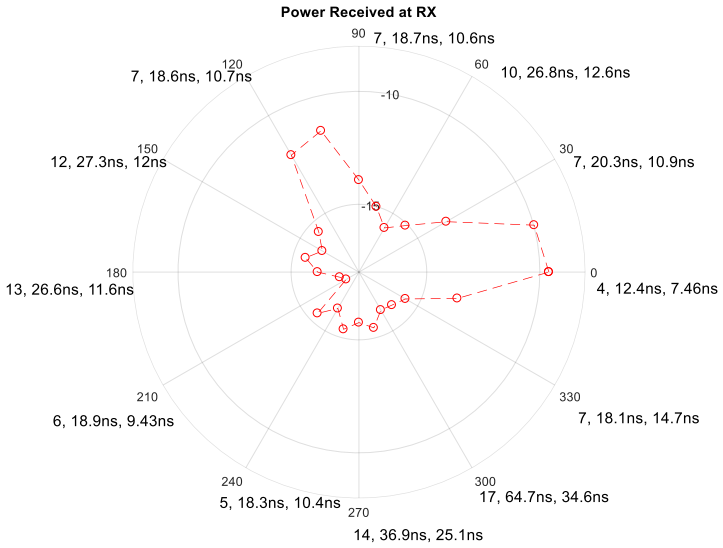

Figure 5.22: AOA polar plot received power in dBm at the RX on engineering building rotunda. The plot shows number of resolvable multipath components, the excess delay, and RMS delay spread for every 30° RX azimuth angles.

Table 5.8: EB rotunda crowded with people measurement results for 18 m TX-RX separation distance.

Angle in degrees	Total received power (dBm)	10 dB threshold paths	Excess delay (ns)	RMS delay spread (ns)
0	-13.7998	6	16.4	9.48
15	-13.2866	6	18.7	10.6
30	-35.4095	10	24.1	10.0
45	-31.7460	10	20.3	10.5
60	-33.2782	8	20.3	10.7
75	-35.3070	16	46.2	31.4
90	-32.0921	9	28.5	11.5
105	-26.9932	9	21.4	10.9
120	-28.1750	7	21.9	9.94
135	-29.9428	9	21.7	11.0
150	-26.8431	10	24.6	11.2
165	-32.9858	10	23.8	85.6
180	-32.8704	9	24.9	10.6
195	-32.9128	14	24.3	37.7
210	-34.2266	8	14.8	7.87
225	-27.6729	8	16.5	9.60
240	-18.9537	7	15.0	9.45
255	-25.9888	6	17.8	10.1
270	-19.6253	8	18.7	10.6
285	-28.1500	8	17.8	10.2
300	-33.3977	7	14.6	8.64
315	-30.3297	7	21.6	10.8
330	-23.7057	5	14.9	8.19
345	-18.9464	7	17.6	9.87

5.2.5. Outdoor wideband measurements. Outdoor measurements were conducted in the area between the library and Engineering Building 1. The TX position was fixed, and the RX was moved into three different locations as shown in Figure 5.25. The measurement results are summarized in Table 5.9, Table 5.10 and Table 5.11.

The results show that the number of paths, excess delay and RMS delay spread in general are higher for outdoor cases rather than indoor cases. In addition, the path loss is also higher for the outdoor case too. The excess delay and RMS delay spread maximum values are 210 ns and 406 ns, respectively.

In addition, the results show that the number of paths increase as TX-RX distance increase, then it starts decreasing because of the high path loss associated with high TX-RX separation.

The multipath component generated is coming from more than a single cluster, which is the case for most indoor scenarios. The multipath components varied from 5 to 82 for all outdoor scenarios.

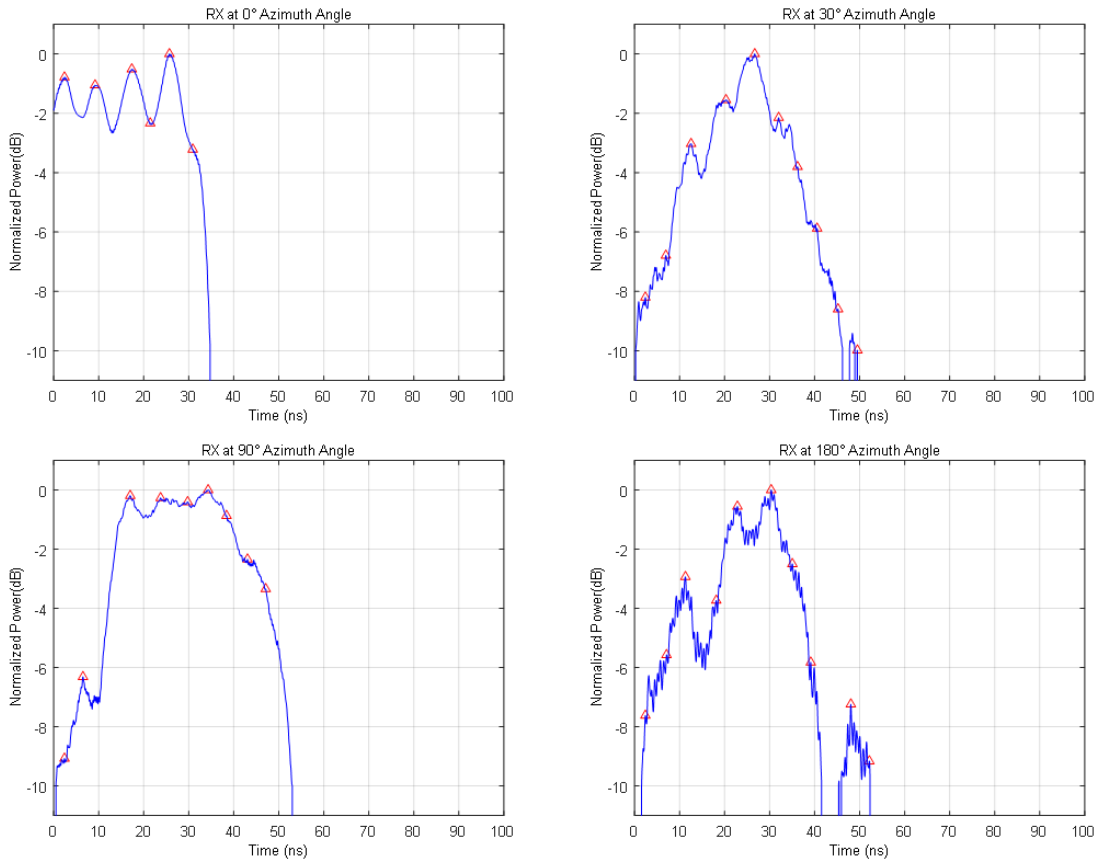

Figure 5.23: PDP of crowded engineering building measurements for 0°, 30°, 90° and 180° RX antenna angle.

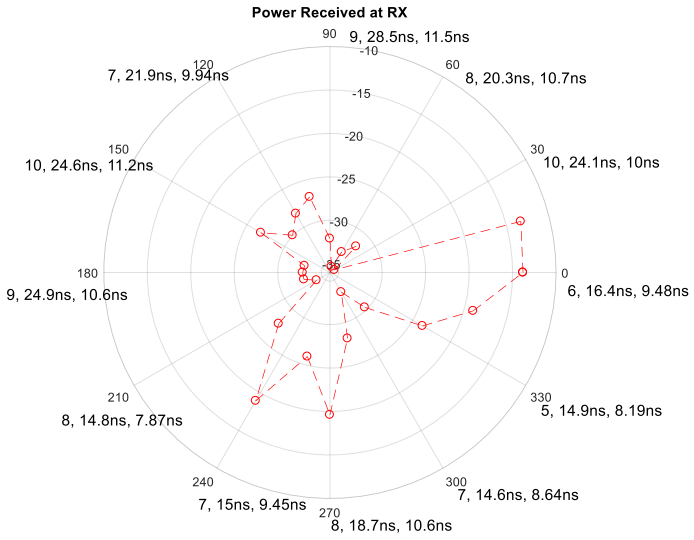

Figure 5.24: AOA polar plot received power in dBm at the RX on crowded engineering building. The plot shows number of resolvable multipath components, the excess delay, and RMS delay spread for every 30° RX azimuth angles.

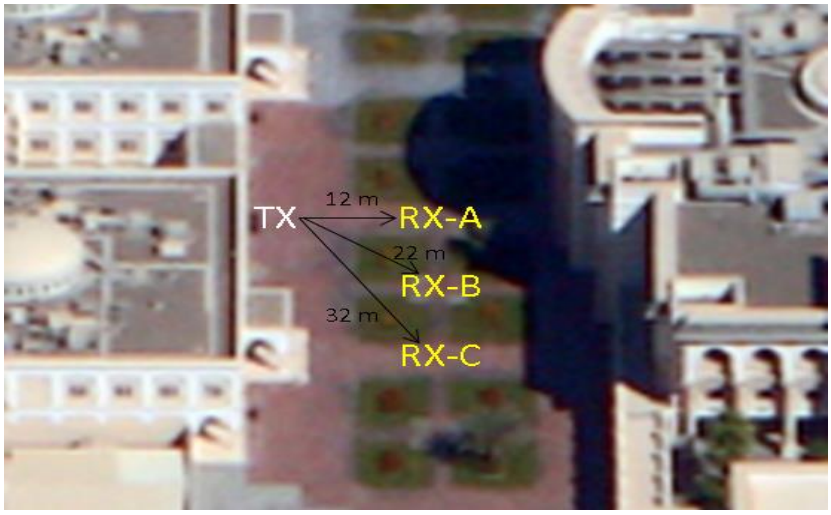

Figure 5.25: Outdoor measurement scenarios.

Table 5.9: Outdoor at point A measurement results for 12 meters TX-RX separation distance.

Angle in degrees	Total received power (dBm)	10 dB threshold paths	Excess delay (ns)	RMS delay spread (ns)
0	-10.8160	6	18.7	10.7
15	-11.8271	7	19.3	10.8
30	-17.7068	8	20.5	11.1
45	-26.6663	7	17.0	9.94
60	-31.3170	4	16.4	8.55
75	-33.0229	7	18.9	9.77
90	-35.8357	14	42.0	156
105	-36.4024	82	73.1	433
120	-35.6864	17	56.2	23.5
135	-33.9188	16	95.5	43.4
150	-30.5678	13	87.3	30.2
165	-26.5439	7	20.6	10.8
180	-23.1195	6	17.0	9.85
195	-24.3963	6	14.9	9.06
210	-27.4221	6	24.0	8.37
225	-31.5262	8	17.0	10.5
240	-30.9314	5	18.0	9.15
255	-27.9475	7	18.9	10.5
270	-32.4248	8	18.1	11.0
285	-35.0854	7	22.0	10.9
300	-33.7782	7	16.3	8.61
315	-30.1371	7	20.3	10.2
330	-23.1053	7	18.3	10.1
345	-14.3715	6	15.3	9.25

Table 5.10: Outdoor at point B measurement results for 22 meters TX-RX separation distance.

Angle in degrees	Total received power (dBm)	10 dB threshold paths	Excess delay (ns)	RMS delay spread (ns)
0	-12.3150	6	18.7	10.9
15	-13.8332	7	18.6	10.8
30	-20.0768	6	18.7	10.6
45	-28.6032	6	18.5	10.7
60	-32.0834	6	16.9	9.88
75	-34.2643	7	16.8	9.92
90	-35.3504	9	23.5	10.7
105	-36.2310	49	210	406
120	-30.6502	14	29.5	72.3
135	-28.2727	34	136	302
150	-35.0248	24	113	110
165	-32.6339	26	179	69.8
180	-33.4158	21	144	97.5
195	-33.8503	29	99.9	90.3
210	-34.3697	19	93.3	53.4
225	-33.6246	12	18.2	9.76
240	-35.9495	29	149	394
255	-34.1311	13	84.4	17.5
270	-35.6969	16	67.8	27.7
285	-35.1289	12	31.5	32.4
300	-33.0768	7	18.6	10.3
315	-29.0256	7	18.8	10.1
330	-23.1640	7	18.8	10.9
345	-15.1393	5	15.8	9.31

Figure 5.26 and Figure 5.27 show, respectively, the PDP for 0°, 30°, 90° and 180° RX antenna angles and the received power polar plot for outdoor point A scenario respectively. Figure 5.28 and Figure 5.29 show, respectively, the PDP for 0°, 30°, 90° and 180° RX antenna angles and the received power polar plot for outdoor point B scenario.

Table 5.11: Outdoor at point C measurement results for 32 meters TX-RX separation distance.

Angle in degrees	Total received power (dBm)	10 dB threshold paths	Excess delay (ns)	RMS delay spread (ns)
0	-14.5195	5	16.3	9.56
15	-18.1713	6	18.8	10.8
30	-27.7649	6	20.4	10.8
45	-33.3617	6	15.3	8.48
60	-34.5686	7	19.4	10.1

75	-35.9273	15	51.9	140
90	-36.2918	9	18.4	59.6
105	No signal detected	-	-	-
120	-34.3628	13	42.4	89.1
135	-34.7684	7	18.1	9.85
150	-31.5889	13	32.1	66.2
165	-32.6693	25	97.5	109
180	-32.1277	36	133	137
195	-35.5484	7	15.5	8.14
210	-35.1034	9	22.3	21.0
225	No signal detected	-	-	-
240	-34.9676	30	106	304
255	-33.8560	7	84.1	12.3
270	-32.8308	13	71.7	30.3
285	-33.0095	14	51.3	33.5
300	-33.0676	16	33.8	29.5
315	-28.5750	6	16.5	9.31
330	-20.1685	6	18.5	10.6
345	-14.8600	6	18.5	10.5

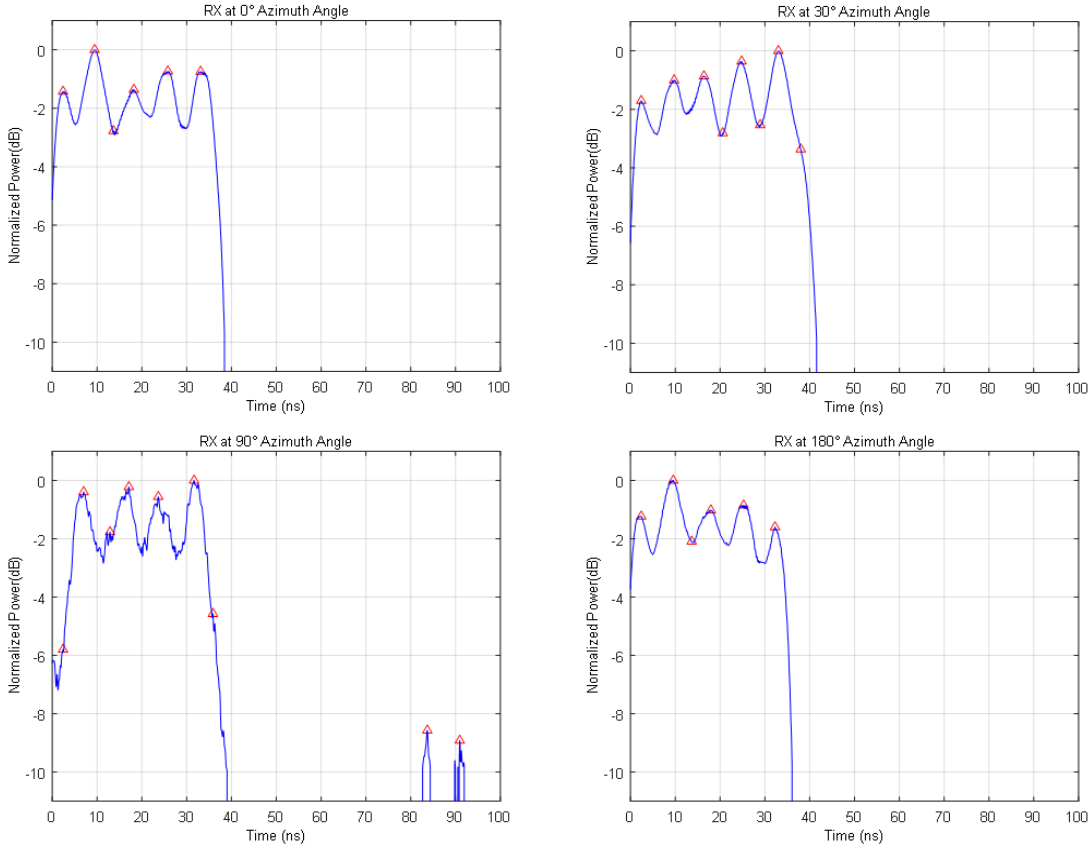

Figure 5.26: PDP of outdoor point A measurements for 0°, 30°, 90° and 180° RX antenna angle.

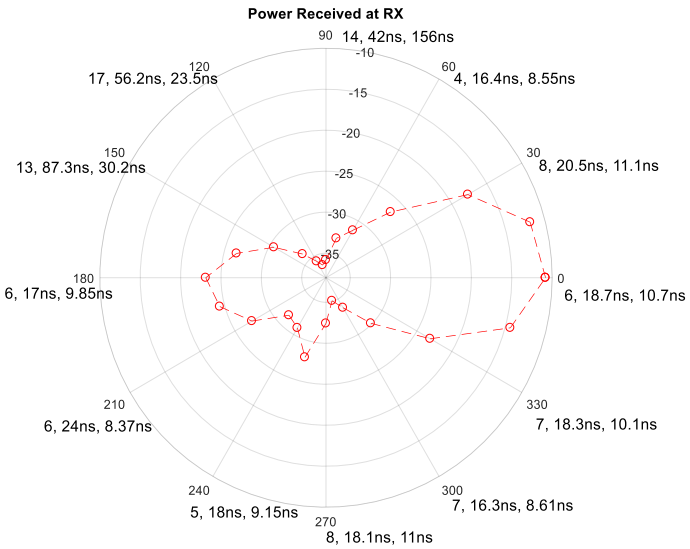

Figure 5.27: AOA polar plot received power in dBm at the RX on outdoor scenario point A. The plot shows number of resolvable multipath components, the excess delay, and RMS delay spread for every 30° RX azimuth angles.

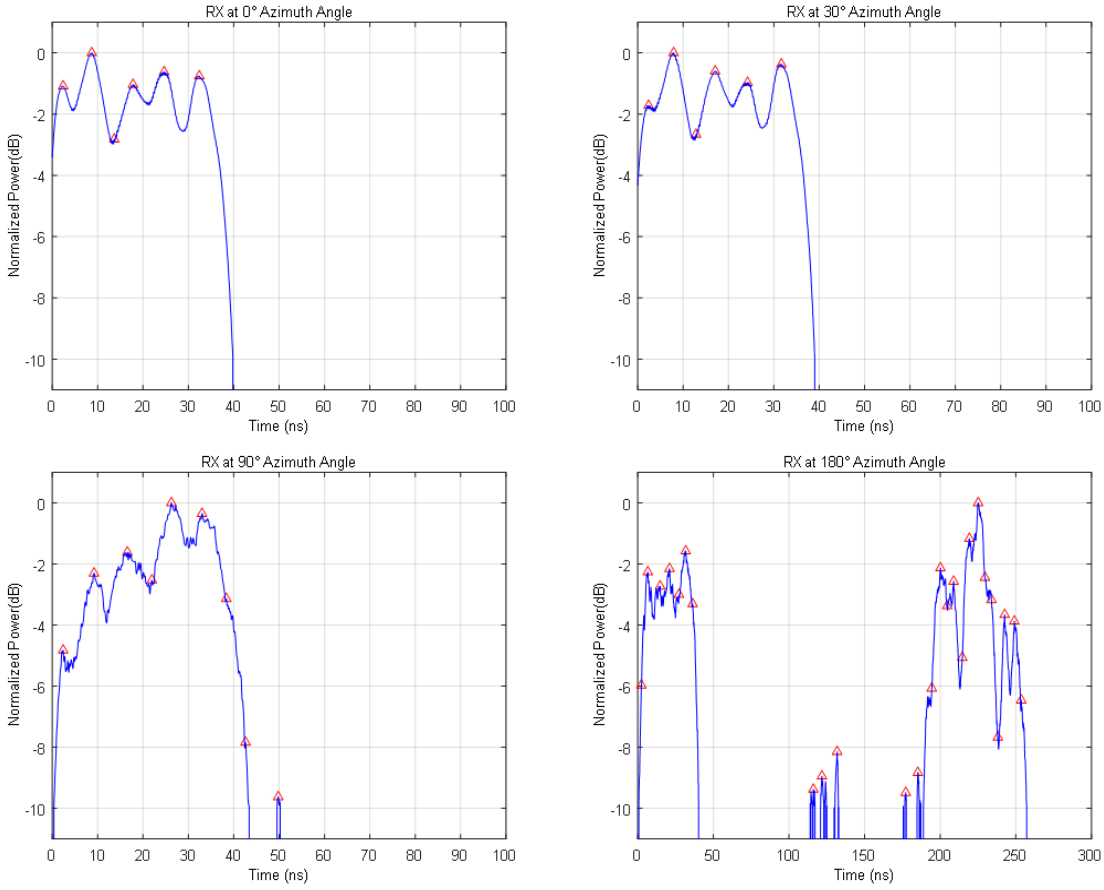

Figure 5.28: PDP of outdoor point B measurements for 0°, 30°, 90° and 180° RX antenna angle.

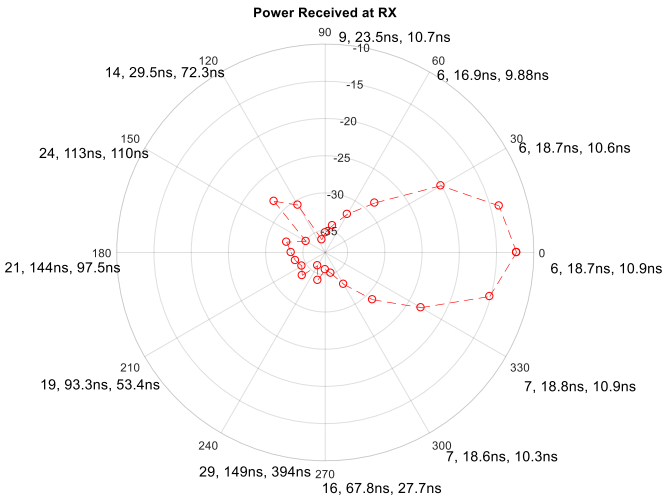

Figure 5.29: AOA polar plot received power in dBm at the RX on outdoor scenario point B. The plot shows number of resolvable multipath components, the excess delay, and RMS delay spread for every 30° RX azimuth angles.

From all of the above results, it seems that in most of cases, there is no multipath component that has a delay more than 60 ns. Moreover, the maximum path delay never exceeds 300 ns for all the cases. This means that for RX designing purpose, an equalizer that can capture 300 ns delay will be able to capture the entire component needed. However, for indoor cases, an equalizer that can capture delays up to 100 ns will be enough.

Chapter 6. Conclusion and Future Work

In this work, a measurement campaign is conducted for wireless channel characterization of mm-waves in different scenarios and environments at the campus of the American University of Sharjah (AUS) in the United Arab Emirates in 2018. Path loss measurements were conducted at 28 GHz carrier frequency in different indoor and outdoor scenarios such as labs, corridors, an underground tunnel, lecture halls, building rotundas, hallway, parking area, and outdoor area with foliage. The path loss exponent (PLE) and the received signal power standard deviation are found for each scenario. These parameters are useful in predicting the path loss for other similar scenarios and help in the proper design of wireless communication systems, especially in 5G mobile radio systems where mm-waves are expected to be used. The results showed that the PLE for indoor line-of-sight scenarios were generally below 2.5 in most of cases. On the other hand, this was not the case for outdoor scenarios with foliage where the PLE was about 6.38. The results also showed that there is no signal leakage between different floors and indoor-outdoor scenarios, which highlight the importance of using repeaters for these cases. Penetration and reflection loss measurements were also conducted in this work using 28 GHz frequency for some of the building materials used in UAE especially different types and colors of glass and aluminum sheets. The materials were tested under different conditions such as clean, dirty, dry and wet. Finally, wideband measurements were conducted using 24 GHz carrier frequency and signal bandwidth of 250 MHz. The measurements were conducted in labs, a corridor, a building rotunda and outdoor scenarios. The channel power delay profile, angle-of-arrival (AOA) spread, RMS delay spread, and the number of multipath component were found. The measurement show that, for indoor scenarios, a maximum delay spread of 100 ns is observed and 300 ns for outdoor scenarios. In addition, the AOA measurement shows the importance of using beamforming techniques for both TX and RX since most of power is received when both TX and RX face each other.

6.1 Future Work.

To be able to apply mm-wave technology in 5G application, large-scale measurements should be conducted in new scenarios such as shopping malls, parks, streets, offices and houses as they are not covered in this work. Moreover, large-scale measurements should be conducted in different weather condition and different times

of the years. Weather conditions such as very high humidity, sand storms, foggy weather and rainy weather are not covered in this work. Further research is also needed for conducting large-scale measurements using other mm-wave frequencies such as 38 and 73 GHz in UAE scenarios.

Other future work could include wideband measurements using other mm-waves frequencies such as 38 and 73 GHz as well as using much higher bandwidths, e.g. more than 250 MHz.

References

[1] S. Rangan, T. S. Rappaport and E. Erkip, "Millimeter-Wave Cellular Wireless Networks: Potentials and Challenges," *Proceedings of the IEEE*, vol. 102, no. 3, pp. 366-385, March 2014.

[2] 3GPP, 3rd Generation Partnership Project (3GPP), "Technical Specification Group Radio Access Network; Study on 3D Channel Model for LTE (release 12)," June 2015, Available: http://www.3gpp.org/dynareport/36873.htm (Access date: Junuary 2018).

[3] T. S. Rappaport, S. Sun and M. Shafi, "Investigation and Comparison of 3GPP And NYUSIM Channel Models For 5G Wireless Communications," *2017 IEEE 86th Vehicular Technology Conference (VTC-Fall)*, Toronto, ON, 2017, pp.1-5.

[4] 3GPP, 3rd Generation Partnership Project (3GPP), "5G; Study on Channel Model for Frequencies from 0.5 to 100 GHz ", TR 38.901, version 14.0.0 Released: 2017.

[5] 3GPP, 3rd Generation Partnership Project (3GPP), "Technical specification group radio access network; study on 3d channel model for lte (release 12)," TR 36.873, version 12.0.0 Releassed: 2016. [Online]. Available: http://www.3gpp.org/dynareport/36873.htm (Access date: Junuary 2018).

[6] E. Ben-Dor, T. S. Rappaport, Y. Qiao and S. J. Lauffenburger, "Millimeter-Wave 60 GHz Outdoor and Vehicle AOA Propagation Measurements Using a Broadband Channel Sounder," *2011 IEEE Global Telecommunications Conference - GLOBECOM 2011*, Kathmandu, 2011, pp. 1-6.

[7] A. Maltsev et al., "Channel Models for 60 GHz WLAN Systems," Tech. Rep., doc: IEEE 802.11-09/0334r8, May 2010, Beijing, Available: https://mentor.ieee.org/802.11/dcn/08/11-08-0811-01-0vht-channel-modeling-for-60-ghz-wlan-systems. (Access date: Junuary 2018).

[8] T. S. Rappaport *et al.*, "Millimeter Wave Mobile Communications for 5G Cellular: It Will Work!," *IEEE Access*, vol. 1, pp. 335-349, 2013.

[9] S. Hur, Y. Cho, J. Lee, Noh-Gyoung Kang, J. Park and H. Benn, "Synchronous Channel Sounder using Horn Antenna and Indoor Measurements on 28 GHz," *2014 IEEE International Black Sea Conference on Communications and Networking (BlackSeaCom)*, Odessa, 2014, pp. 83-87.

[10] G. R. Maccartney, T. S. Rappaport, S. Sun, and S. Deng, "Indoor Office Wideband Millimeter-Wave Propagation Measurements and Channel Models at 28 and 73 GHz For Ultra-Dense 5G Wireless Networks," *IEEE Access*, vol. 3, pp. 2388-2424, 2015.

[11] S. Deng, M. K. Samimi and T. S. Rappaport, "28 GHz and 73 GHz Millimeter-Wave Indoor Propagation Measurements and Path Loss Models," *2015 IEEE International Conference on Communication Workshop (ICCW)*, London, 2015, pp. 1244-1250.

[12] T. S. Rappaport, Y. Xing, G. R. MacCartney, A. F. Molisch, E. Mellios, and J. Zhang, "Overview of Millimeter Wave Communications for Fifth-Generation (5G) Wireless Networks—With a Focus on Propagation Models," *IEEE Transactions on Antennas and Propagation,* vol. 65, no. 12, pp. 6213-6230, 2017.

[13] T. S. Rappaport, J. N. Murdock, and F. Gutierrez, "State of The Art in 60-GHz Integrated Circuitsand Systems for Wireless Communications," *Proceedings of the IEEE,* vol. 99, no. 8, pp. 1390-1436, 2011.

[14] Z. Qingling and J. Li, "Rain Attenuation in Millimeter Wave Ranges," *2006 7th International Symposium on Antennas, Propagation & EM Theory,* Guilin, 2006, pp. 1-4.

[15] M. N. O. Sadiku, *Elements of electromagnetics*, 5th ed. New York : Oxford University Press, 2010.

[16] Z. Pi and F. Khan, "An Introduction to Millimeter-wave Mobile Broadband Systems," *IEEE Communications Magazine,* vol. 49, no. 6, pp. 101-107, 2011.

[17] US Federal Communication Commission, "Allocations and Service Rules for the 71-76 GHZ, 81-86 GHz and 92-95 GHz Bands," DA/FCC #: FCC-03-248, Adopted: October 16, 2003, Released: November 4, 2003, Available: https://www.fcc.gov/document/allocations-and-service-rules-71-76-ghz-81-86-ghz-and-92-95-ghz-1 (Access date: Junuary 2018).

[18] T. Baykas *et al.*, "IEEE 802.15. 3c: the first IEEE Wireless Standard for Data Rates Over 1 Gb/s," *IEEE Communications Magazine*, vol. 49, no. 7, pp, 114-121, 2011.

[19] S. Nie, G. R. MacCartney, S. Sun, and T. S. Rappaport, "72 GHz Millimeter Wave Indoor Measurements For Wireless And Backhaul Communications,"*Personal Indoor and Mobile Radio Communications (PIMRC), 2013 IEEE 24th International Symposium on*, 2013, pp. 2429-2433.

[20] S. Sun, G. R. MacCartney and T. S. Rappaport, "Millimeter-wave distance-Dependent Large-Scale Propagation Measurements and Path Loss Models for Outdoor and Indoor 5G Systems," *2016 10th European Conference on Antennas and Propagation (EuCAP)*, Davos, 2016, pp. 1-5.

[21] K. Haneda *et al.*, "5G 3GPP-Like Channel Models for Outdoor Urban Microcellular and Macrocellular Environments," *2016 IEEE 83rd Vehicular Technology Conference (VTC Spring)*, Nanjing, 2016, pp. 1-7.

[22] K. Haneda, N. Omaki, T. Imai, L. Raschkowski, M. Peter, and A. Roivainen, "Frequency-Agile Athloss Models for Urban Street Canyons," *IEEE Transactions on Antennas and Propagation,* vol. 64, no. 5, pp. 1941-1951, 2016.

[23] G. R. MacCartney, J. Zhang, S. Nie, and T. S. Rappaport, "Path loss models for 5G millimeter wave propagation channels in urban microcells," 2013 *IEEE Global Communications Conference (GLOBECOM),* 2013, pp. 3948-3953.

[24] T. A. Thomas *et al.*, "A Prediction Study of Path Loss Models from 2-73.5 GHz in an Urban-Macro Environment," *2016 IEEE 83rd Vehicular Technology Conference (VTC Spring),* 2016, pp. 1-5.

[25] B. Kim, H. Kim, C. Dongkyu, Y. Lee, H. Wonbin, and P. Jeongho, "28 GHz Propagation Analysis for Passive Repeaters in NLOS Channel Environment," *2015 9th European Conference on Antennas and Propagation (EuCAP)*, 2015, pp. 1-4.

[26] T. S. Rappaport, F. Gutierrez, E. Ben-Dor, J. N. Murdock, Y. Qiao, and J. I. Tamir, "Broadband Millimeter-Wave Propagation Measurements and Models Using Adaptive-Beam Antennas for Outdoor Urban Cellular Communications," *IEEE Transactions on Antennas and Propagation*, vol. 61, no. 4, pp. 1850-1859, 2013.

[27] T. S. Rappaport, G. R. MacCartney, M. K. Samimi, and S. Sun, "Wideband Millimeter-Wave Propagation Measurements and Channel Models for Future Wireless Communication System Design," *IEEE Transactions on Communications*, vol. 63, no. 9, pp. 3029-3056, 2015.

[28] T. S. Rappaport and S. Deng, "73 GHz Wideband Millimeter-Wave Foliage and Ground Reflection Measurements and Models," *2015 IEEE International Conference on Communication Workshop (ICCW)*, London, 2015, pp. 1238-1243.

[29] H. Xu, T. S. Rappaport, R. J. Boyle, and J. H. Schaffner, "Measurements and Models for 38-Ghz Point-To-Multipoint Radiowave Propagation," *IEEE Journal on Selected Areas in Communications*, vol. 18, no. 3, pp. 310-321, 2000.

[30] O. H. Koymen, A. Partyka, S. Subramanian and J. Li, "Indoor mm-Wave Channel Measurements: Comparative Study of 2.9 GHz and 29 GHz," *2015 IEEE Global Communications Conference (GLOBECOM)*, San Diego, CA, 2015, pp. 1-6.

[31] G. R. MacCartney and T. S. Rappaport, "73 GHz Millimeter Wave Propagation Measurements for Outdoor Urban Mobile and Backhaul Communications in New York City," *2014 IEEE International Conference on Communications (ICC)*, Sydney, NSW, 2014, pp. 4862-4867.

[32] V. Raghavan *et al.*, "Millimeter-Wave MIMO Prototype: Measurements and Experimental Results," *IEEE Communications Magazine*, vol. 56, no. 1, pp. 202-209, 2018.

[33] S. Collonge, G. Zaharia, and G. E. Zein, "Influence of the Human Activity on Wide-Band Characteristics of The 60 GHz Indoor Radio Channel," *IEEE Transactions on Wireless Communications*, vol. 3, no. 6, pp. 2396-2406, 2004.

[34] A. Anglès-Vázquez, E. Carreño, and L. S. Ahumada, "Modeling the Effect of Pedestrian Traffic in 60-GHz Wireless Links," *IEEE Antennas and Wireless Propagation Letters*, vol. 16, pp. 1927-1931, 2017.

[35] X. Chen, L. Tian, P. Tang, and J. Zhang, "Modelling of Human Body Shadowing Based on 28 GHz Indoor Measurement Results," *2016 IEEE 84th Vehicular Technology Conference (VTC-Fall)*, 2016, pp. 1-5.

[36] D. Cassioli and N. Rendevski, "A Statistical Model for the Shadowing Induced by Human Bodies in the Proximity of a mmwaves Radio Link," *2014 IEEE International Conference on Communications Workshops (ICC)*, 2014, pp. 14-19.

[37] M. Ghaddar, M. Nedil, L. Talbi, and J. Lebel, "Experimental Analysis of Human Body Effects on NLOS 60 GHz Propagation Channel," *2015 IEEE International Symposium on Antennas and Propagation & USNC/URSI National Radio Science Meeting*, 2015, pp. 1788-1789.

[38] M. Nakamura, M. Sasaki, M. Inomata, and T. Onizawa, "The Effect of Human Body Blockage To Path Loss Characteristics In Crowded Areas," *2016 International Symposium on Antennas and Propagation (ISAP)*, 2016, pp. 218-219.

[39] A. I. Sulyman, A. T. Nassar, M. K. Samimi, G. R. Maccartney, T. S. Rappaport, and A. Alsanie, "Radio Propagation Path Loss Models for 5G Cellular Networks in the 28 Ghz and 38 Ghz Millimeter-Wave Bands," *IEEE Communications Magazine*, vol. 52, no. 9, pp. 78-86, 2014.

[40] T. Nguyen. (2017, 23/2/2018). *Small Cell Networks and the Evolution of 5G (Part 1).* Available: http://www.qorvo.com/design-hub/blog/small-cell-networks-and-the-evolution-of-5g (Access date: February 2018)

[41] H. Seleem, A. Alsanie, and A. I. Sulyman, "Two-Stage Multiuser Access in 5G Cellular Using Massive MIMO and Beamforming," *International Conference on Cognitive Radio Oriented Wireless Networks*, 2015, pp. 54-65: Springer.

[42] G. R. MacCartney and T. S. Rappaport, "Rural Macrocell Path Loss Models for Millimeter Wave Wireless Communications," *IEEE Journal on Selected Areas in Communications*, vol. 35, no. 7, pp. 1663-1677, July 2017.

[43] G. R. MacCartney Jr and T. S. Rappaport, "Study on 3GPP Rural Macrocell Path Loss Models for Millimeter Wave Wireless Communications," *arXiv preprint arXiv:1703.10300*, 2017.

[44] J. N. Murdock, E. Ben-Dor, Y. Qiao, J. I. Tamir, and T. S. Rappaport, "A 38 GHz Cellular Outage Study for an Urban Outdoor Campus Environment," *IEEE Wireless Communications and Networking Conference (WCNC), 2012 IEEE*, 2012, pp. 3085-3090.

[45] C. L. Dillard, T. M. Gallagher, C. W. Bostian, and D. G. Sweeney, "Rough surface Scattering from Exterior Walls at 28 GHz," *IEEE Transactions on Antennas and Propagation*, vol. 52, no. 12, pp. 3173-3179, 2004.

[46] O. Landron, M. J. Feuerstein, and T. S. Rappaport, "A Comparison of Theoretical and Empirical Reflection Coefficients for Typical Exterior Wall Surfaces in a Mobile Radio Environment," *IEEE Transactions on Antennas and Propagation*, vol. 44, no. 3, pp. 341-351, 1996.

[47] Yong-Hoon Kim, Ki-Seok Yang and Sung-Hyun Kim, "Scattering Characteristics of Surface Roughness in Frequency and Incident Angle Dependent at Millimeter-Wave," *1999 Asia Pacific Microwave Conference. APMC'99. Microwaves Enter the 21st Century. Conference Proceedings (Cat. No.99TH8473)*, Singapore, 1999, pp. 789-792 vol.3.

[48] J. Ryan, G. R. MacCartney Jr, and T. S. Rappaport, "Indoor Office Wideband Penetration Loss Measurements at 73 GHz," *arXiv preprint arXiv:1703.08030*, 2017.

[49] H. Zhao *et al.*, "28 GHz Millimeter Wave Cellular Communication Measurements for Reflection and Penetration Loss in and Around Buildings in New York City," *2013 IEEE International Conference on Communications (ICC)*, Budapest, 2013, pp. 5163-5167.

[50] A. A. Vazquez, E. Carreno, and L. Ahumada, "Modelling the Effect of pedestrian Traffic in 60 Ghz Wireless Links," *IEEE Antennas and Wireless Propagation Letters*, vol. 16, pp. 1927-1931, 2017.

[51] A. A. AlAbdullah, N. Ali, H. Obeidat, R. A. Abd-Alhmeed, and S. Jones, "Indoor Millimetre-Wave Propagation Channel Simulations at 28, 39, 60 and 73 GHz for 5G Wireless Networks." *2017 Internet Technologies and Applications (ITA)*, Wrexham, 2017, pp. 235-239.

[52] C. E. O. Vargas, L. d. S. Mello, and R. C. Rodriguez, "Measurements of Construction Materials Penetration Losses at Frequencies from 26.5 GHz to 40 GHz," *IEEE Pacific Rim Conference on Communications, Computers and Signal Processing (PACRIM)*, 2017, pp. 1-4.

[53] *Y. Du* et al., *"*Measurement and Modeling of Penetration Loss in the Range from 2 GHz to 74 GHz,*"* 2*016 IEEE Globecom Workshops (GC Wkshps), Washington, DC*, 2016, pp. 1-6.

[54] R. J. Pirkl and G. D. Durgin, "Optimal Sliding Correlator Channel Sounder Design," *IEEE Transactions on Wireless Communications*, vol. 7, no. 9, pp. 3488-3497, September 2008.

[55] G. R. MacCartney Jr, H. Yan, S. Sun, and T. S. Rappaport, "A Flexible Wideband Millimeter-Wave Channel Sounder with Local Area and NLOS to LOS transition Measurements," *arXiv preprint arXiv:1703.08043*, 2017.

[56] R. J. Pirkl and G. D. Durgin, "How to Build an optimal broadband channel Sounder," *2007 IEEE Antennas and Propagation Society International Symposium*, Honolulu, HI, 2007, pp. 601-604.

[57] N. Moraitis and P. Constantinou, "Measurements and Characterization of Wideband Indoor Radio Channel at 60 GHz," *IEEE Transactions on Wireless Communications*, vol. 5, no. 4, pp. 880-889, April 2006.

[58] Y. Azar *et al.*, "28 GHz Propagation Measurements for Outdoor Cellular Communications using Steerable Beam Antennas in New York City," *IEEE International Conference on Communications (ICC)*, 2013, pp. 5143-5147.

[59] M. Kyrö, S. Ranvier, V.-M. Kolmonen, K. Haneda, and P. Vainikainen, "Long Range Wideband Channel Measurements at 81–86 GHz Frequency Range," *Proceedings of the Fourth European Conference on Antennas and Propagation (EuCAP)*, 2010, pp. 1-5.

[60] T. S. Rappaport, E. Ben-Dor, J. N. Murdock, and Y. Qiao, "38 GHz and 60 GHz Angle-Dependent Propagation for Cellular & Peer-to-Peer Wireless Communications," *IEEE International Conference on Communications (ICC)* , 2012, pp. 4568-4573.

[61] J. Ko *et al.*, "Millimeter-Wave Channel Measurements and Analysis for Statistical Spatial Channel Model in In-Building and Urban Environments at 28 GHz," *IEEE Transactions on Wireless Communications*, vol. 16, no. 9, pp. 5853-5868, 2017.

[62] M.-D. Kim, J. Liang, J. Lee, J. Park, and B. Park, "Directional Multipath Propagation Characteristics Based on 28ghz Outdoor Channel Measurements,"*10th European Conference on Antennas and Propagation (EuCAP)* , 2016, pp. 1-5.

[63] M.-D. Kim, J. Liang, H.-K. Kwon, and J. Lee, "Directional Delay Spread Characteristics Based on Indoor Channel Measurements at 28GHz," *2015 IEEE 26th Annual International Symposium on Personal, Indoor, and Mobile Radio Communications (PIMRC), ,* 2015, pp. 403-407.

[64] M. S. Bartlett, "Smoothing Periodograms from Time Series with Continuous Spectra," *Nature,* vol. 161, no. 4096, pp. 686-687, 1948.

[65] INU, "Multi Propagation and Parameterization of its Characteristics," *International Telecommunication Union: Geneva, Switzerland,* 1999, Available: https://www.itu.int/dms_pubrec/itu-r/rec/p/R-REC-P.1407-0-199907-S!!PDF-E.pdf (Access date: March 2018).

[66] A. M. Al-Samman, T. A. Rahman, and J. Nasir, "Time Dispersion Characteristics for Wideband Channel in 28 GHz Millimeter Wave Band for 5G Cellular Networks," *2015 IEEE 11th International Colloquium on Signal Processing & Its Applications (CSPA), ,* 2015, pp. 1-4.

[67] M. Zhu, G. Eriksson, and F. Tufvesson, "The COST 2100 Channel Model: Parameterization and Validation Based on Outdoor MIMO Measurements at 300 MHz," *IEEE Transactions on Wireless Communications,* vol. 12, no. 2, pp. 888-897, 2013.

[68] H. Arslan and T. Yucek, "Delay Spread Estimation For Wireless Communication Systems," *Proceedings of the Eighth IEEE Symposium on Computers and Communications. ISCC 2003,* Kemer-Antalya, Turkey, 2003, pp. 282-287 vol.1.

[69] M. K. Samimi and T. S. Rappaport, "Ultra-Wideband Statistical Channel Model for Non Line of Sight Millimeter-Wave Urban Channels," *2014 IEEE Global Communications Conference,* Austin, TX, 2014, pp. 3483-3489.

[70] S. Hur *et al.*, "Wideband Spatial Channel Model in an Urban Cellular Environments at 28 GHz," *2015 9th European Conference on Antennas and Propagation (EuCAP), ,* 2015, pp. 1-5.

[71] M. Kyro, V.-M. Kolmonen, and P. Vainikainen, "Experimental Propagation Channel Characterization of Mm-Wave Radio Links in Urban Scenarios," *IEEE Antennas and Wireless Propagation Letters,* vol. 11, pp. 865-868, 2012.

[72] *G. R. MacCartney, M. K. Samimi and T. S. Rappaport, "Omnidirectional path loss models in New York City at 28 GHz and 73 GHz,"* 2014 IEEE 25th Annual International Symposium on Personal, Indoor, and Mobile Radio Communication (PIMRC), *Washington, DC, 2014, pp. 227-231*

[73] A. I. Sulyman, A. Alwarafy, G. R. MacCartney, T. S. Rappaport, and A. Alsanie, "Directional Radio Propagation Path Loss Models for Millimeter-Wave Wireless Networks in the 28-, 60-, and 73-GHz Bands," *IEEE Transactions on Wireless Communications,* vol. 15, no. 10, pp. 6939-6947, 2016.

[74] Z. Shi, Y. Wang, L. Huang, and J. Ma, "System Capacity of 72 GHz mmWave Transmission in Hybrid Networks," *2016 IEEE 84th Vehicular Technology Conference (VTC-Fall),* 2016, pp. 1-5.

[75] J. Järveläinen, K. Haneda, and A. Karttunen, "Indoor Propagation Channel Simulations at 60 GHz Using Point Cloud Data," *IEEE Transactions on Antennas and Propagation*, vol. 64, no. 10, pp. 4457-4467, 2016.

[76] J. Blumenstein et al., " In-Vehicle Channel Measurement, Characterization, and Spatial Consistency Comparison of 30--11 GHz and 55--65 GHz Frequency Bands," *IEEE Transactions on Vehicular Technology*, vol. 66, no. 5, pp. 3526-3537, 2017.

Appendix A

Summary of path loss measurements results found in the literature review.

References	Frequency (GHz)	Location	LOS / NLOS	PLE	Std Dev
[39]	28	Manhattan, New York City. TX height of 17 m and RX height of 1.5m.	LOS - Best Values	-	-
			NLOS- Best Values	4	7.4
			LOS- Average Values	1.8	0.1
			NLOS- Average Values	4.6	9.2
		Manhattan, New York City. TX height of 7 m and RX height of 1.5m.	LOS- Best Values	-	-
			NLOS- Best Values	3.7	9.5
			LOS- Average Values	1.9	1.1
			NLOS- Average Values	4.5	10.8
[8]		NYU-poly campus in Brooklyn and NYU campus in Manhattan	LOS- Best Values	1.68	0.2
			NLOS- Best Values	4.58	8.83
			LOS- Average Values	2.55	8.66
			NLOS- Average Values	5.76	9.03
[72]		Urban environment (Manhattan)	LOS	2.1	3.6
			NLOS	3.4	9.7
[32]	29	Indoor Office	LOS	1.46	4.25
			NLOS	3.46	8.31
		Indoor Shopping Mall	LOS	1.98	3.56
			NLOS	2.76	9.47
		Urban micro Street Canyon	LOS	2.19	4.37
			NLOS	3.07	3.27
		Outdoor open areas	LOS	2.73	5.73
			NLOS	3.39	8.03
[8]	38	NYU-poly campus in Brooklyn and NYU campus in Manhattan	LOS- Best Values	1.89	4.55
			NLOS- Best Values	3.2	11.69
			LOS- Average Values	2.3	11.5
			NLOS- Average Values	3.86	13.39
		UT Austin campus	LOS	2.3	11.55
			NLOS	3.86	13.39
[26]		UT Austin campus (more directive antenna)	LOS	2.2	10.3
			NLOS	3.88	14.6
		UT Austin campus (less directive antenna)	LOS	2.21	9.4
			NLOS	3.18	11
[39]		Campus at the University of Texas at Austin, TX height of 23 m	LOS	2	2.3
			NLOS - Best	2.7	8
			NLOS - All	3.3	10.6
		Campus at the University of Texas at Austin, TX height of 8 m	LOS	1.9	8.4
			NLOS - Best	3.2	10.3
			NLOS - All	3.8	11.1
		Campus at the University of Texas at Austin, TX height of 36 m	LOS	1.9	3.7
			NLOS - Best	2.6	8.1
			NLOS - All	3.1	10.3
[60]		University of Texas at Austin campus. P2P Channel in Pedestrian Walkway	LOS	2	3.79
			NLOS	4.57	11.72
[60]		University of Texas at Austin campus, Cellular Channel in an Urban Campus.	LOS	2.22	6.38
			NLOS	3.88	11.43
[73]	60	Courtyard (P2P)	LOS	2.2	2
			NLOS	3.6	9
		Peer to Vehicle	LOS	2.5	3.5
			NLOS	5.4	14.8
[60]		University of Texas at Austin campus. P2P Channel in Pedestrian Walkway	LOS	2.25	2
			NLOS	4.22	10.12
[6]		Vehicle to Vehicle	LOS	2.66	5.4
			NLOS	7.17	23.8
[6]		Outdoor courtyard with pedestrian walkway between several buildings on The Univ. of Texas campus. The courtyard had little vegetation but had several lamp poles and was surrounded by tall office buildings 6 to 10 stories high. Antennas pointing to each other (P2P)	LOS	2.23	1.87
			NLOS	4.19	9.98
[32]	61	Indoor Office	LOS	1.59	4.81
			NLOS	4.17	13.83
		Indoor Shopping Mall	LOS	2.05	4.29
			NLOS	2.98	12.86

		Urban micro Street Canyon	LOS	2.22	4.84
			NLOS	3.27	10.7
		Outdoor open areas	LOS	2.83	6.78
			NLOS	3.42	1.97
[74]	72	In urban micro (UMi) street canyon scenarios using 3rd Generation Partnership Project (3GPP)	LOS	1.98	3.1
			NLOS	3.19	8.2
[73]	73	Courtyard (P2P), RX at height of 2 m	LOS(TX at height of 17m	2.2	4.1
			LOS, TX at height of 7m	2.3	6.9
			NLOS, TX at height of 17m	4.4	11.7
			NLOS, TX at height of 7m	4.9	11.9
		Courtyard (P2P), RX at height of 4.06 m	LOS,TX at height of 17m	2.3	4.6
			LOS, TX at height of 7m	2.4	9.1
			NLOS, TX at height of 17m	4.5	12.6
			NLOS, TX at height of 7m	4.8	12.4
[72]		Urban Environment (Manhattan), RX at height 2 m	LOS	2	5.2
			NLOS	3.3	7.6
		Urban Environment (Manhattan), RX at height 4.06 m	LOS	2	4.2
			NLOS	3.5	7.9

Appendix B

Summary of small-scale measurements results found in the literature review.

Reference	Frequency (GHz)	Scenario	RMS delay spread s (ns)	
			Mean	Variance
[10]	28	V-V polarized, LOS	17.3	18
		V-V polarized, NLOS	17.7	13.8
		V-V polarized, LOS-Best	4.1	1.6
		V-V polarized, NLOS-Best	13.4	13.1
		V-H polarized, LOS	17.2	14.5
		V-H polarized, NLOS	18	10.9
		V-H polarized, LOS-Best	7.3	3.5
		V-H polarized, NLOS-Best	13.2	10.8
		Combined Polarizations, LOS	17.2	16.4
		Combined Polarizations, NLOS	17.8	12.5
		Combined Polarizations, LOS-Best	4.1	1.6
		Combined Polarizations, NLOS-Best	13.4	13.1
[27]		narrow beam, Manhattan	17.6	-
		wide beam, Brooklyn	15.6	-
		Directional beam with lowest PL: Narrowbeam LOS	0.85	-
		Directional beam with lowest PL: Narrowbeam NLOS	25.7	-
		Directional beam with lowest PL: Widebeam NLOS	7.1	-
[27]	38	narrow beam, Austin	11.4	-
		wide beam, Austin	7.7	-
		P2P: Narrowbeam	23.6	-
[60]		LOS - Urban Peer-to-Peer Channel in Pedestrian Walkway	1.2	-
		NLOS - Urban Peer-to-Peer Channel in Pedestrian Walkway	23.6	-
[10]	73	V-V polarized, LOS	12.8	16.9
		V-V polarized, NLOS	12.3	14.2
		V-V polarized, LOS-Best	3.6	1.5
		V-V polarized, NLOS-Best	11.3	14.4
		V-H polarized, LOS	11.4	17.5
		V-H polarized, NLOS	8.4	10.6
		V-H polarized, LOS-Best	7	10.9
		V-H polarized, NLOS-Best	12.5	22.5
		Combined , LOS	12.1	17.2
		Combined , NLOS	10.7	13
		Combined , LOS-Best	3.6	1.5
		Combined , NLOS-Best	11.3	14.4
[27]		NLOS - Access (Unique pointing angles)	11.1	-
		NLOS - Backhaul (Unique pointing angles)	9.4	-
		Directional beam with lowest PL: Access LOS	1.2	-
		Directional beam with lowest PL: Backhaul LOS	1.5	-
		Directional beam with lowest PL: Access NLOS	7.1	-
		Directional beam with lowest PL: Backhaul NLOS	5.6	-
[27]	60	P2P: Narrowbeam	7.4	-
[75]		indoor - cafeteria : LOS	4.4	-
			6.9	-
			7.3	-
			5.1	-
			6.9	-
			7.7	-
		indoor - cafeteria : LOS	17.6	-
			10.8	-
			9.6	-
			18.4	-
			14.4	-
			11.3	-
[60]		LOS - Urban P2P Channel in Pedestrian Walkway	0.8	-
		NLOS - Urban P2P Channel in Pedestrian Walkway	7.4	-
[76]	3 -- 11	Mid size vehicle. TX is placed at 10×10 spatial points, using a polystyrene rack for 3–11 GHz and a metallic X–Y table covered with absorbers for 55–65 GHz. RX is placed next to the rear-view mirror on the front windshield	23.34	<0.01
			23.27	<0.01
	55 -- 65		5.02	<0.01
			5.02	<0.01

Vita

Mohammed K.Y Aborahama was born in 1994, in Dubai, United Arab Emirates. He received his primary and secondary education in Dubai, UAE. He received his B.Sc. degree in Electrical Engineering from the American University of Sharjah in 2016.

In February 2017, he joined the Electrical Engineering master's program in the American University of Sharjah as a graduate teaching assistant. During his master's study, he authored a paper entitled “Large-scale Channel Measurements at 28 GHz in the United Arab Emirates for 5G systems” which was presented in 14th IEEE Radio & Wireless Week published in 2019. His research interests are in wireless communication, antennas, wave propagation and microwave engineering.